1—
Introduction:
Developments in Textile Characterization Methods

Mastura Raheel
University of Illinois at Urbana-Champaign, Urbana, Illinois

Textile characterization must take into consideration an in-depth understanding of the nature of fiber-forming materials (polymers), fiber structure, its physical, mechanical, and chemical properties, and how these properties relate to further engineering operations that result in fabrics/textiles and finished products. The end-use performance of finished products will depend upon all these factors, and can be predicted on the basis of fundamental theories of fiber science and sound characterization methods.

Fundamental theories of fiber science have evolved from the classical theories of physics, chemistry, polymer science, and engineering. The greatest advances in textile materials have been where linear laws of classical physics or physical chemistry can be applied. The difficulties increase when it becomes necessary to take account of quantum and relativistic effects and chemical interactions. Textile systems generally are extraordinarily complex, and the effects of treatments almost invariably go beyond the bound of linearity. Thus predictive mathematical models may very well be nonlinear or only yield empirical statistical correlations. Major strides have been made in the last decade or so in the use of sophisticated methods and mathematical models to characterize textile materials and predict end-use performance. Textile characterization is important at all stages of textile production and processing in order to achieve a product that meets perceived performance needs. The aim of textile characterization is to understand the material structure and behavior as well as the processes sufficiently to be able to predict their consequences, and so to be able to set up control techniques that will lead to products with specified properties.

There are numerous well-known organizations, such as the International Standards Organization (ISO), the American Society for Testing and Materials

(ASTM), the American Association of Textile Chemists and Colorists (AATCC), the European Standardization Committee (CEN), and various others, that develop standard test methods for evaluating and predicting performance of fibrous systems. However, generally, there is a significant time lag between the developments in textile characterization methods and their acceptance as standard methods. The literature is replete with innovative uses of standard methods as well as newer methods and instrumentation for characterizing polymers, fibers, textiles, and their auxiliaries. It is not the intent of this book to include all physical, mechanical, and chemical methods for characterization of fibrous materials, but rather to focus on recent developments in selected characterization methods and their applications to fibrous systems, based on evolving theories of physical, chemical, and engineering sciences.

The book begins with polymer characterization methods. Polymers, the fiber-forming materials, have (or can be manipulated to have) characteristic structures and physicochemical properties. These features have profound impact on fiber and textile properties. In Chapter 2 P. H. Geil, a renowned polymer scientist, discusses in great detail polymer characterization methods. The specific areas of polymer characterization covered in Chapter 2 include (1) chemical structure, including composition and configuration, (2) physical structure, including crystallinity and morphology-related aspects, and (3) physiochemical properties.

Geil mentions the use of traditional methods of characterizating various aspects of polymers but focuses mainly on recent advances in polymer characterization methods. For example, polymer chemical composition and configuration analysis begins with the traditional analytical chemistry techniques of elemental analysis by atomic absorption spectroscopy, x-ray dispersive analysis, and reaction of specific groups in a polymer with specific reagents, but the thrust of his discussion is on Fourier-transform infrared spectroscopy (FTIR) and FT nuclear magnetic resonance (FT-NMR) methods. He explains the theoretical basis of these analytical techniques and provides practical guidance about sample preparation, the analytical technique, and interpretation of results. Also, he describes the usefulness of these techniques in studying textile fibers. Molecular weight determination is described using chromatography processes and also by simpler techniques such as solution and melt viscosity methods. The significance of molecular weight characterization on solution spinning and melt spinning of fibers is described.

The physical structure of polymers and fibers requires a range of techniques for characterization because of the range of size scales, particularly in fibers. The structures of interest fall into the size scale of the individual molecular segment; the relative number of regular and random conformations and their arrangement in space, that is, the degree of crystallinity and orientation; the size and shape of the crystalline and amorphous regions; and the organization and interaction of these crystals in larger structures. Characterization of all these aspects is discussed in

great detail with illustrations and examples of polymers and fibers by using a range of techniques. The techniques described include FTIR, electron diffraction (ED), x-ray diffraction [both wide-angle (WAXD) and small-angle scattering (SAXS)], and electron microscopy (EM) [both scanning (SEM) and transmission (TEM)]; also many probe microscopes are described. Geil cautions about the problems in utilizing several techniques (especially electron diffraction) that primarily depend upon appropriate sample preparation. He suggests sample preparation methods and describes their representative results and potential difficulties.

In Chapter 3, W. R. Goynes discusses the importance of structural characterization of fibers and textiles using scanning electron microscopic (SEM) techniques. He focuses on the specifics of sample preparation and microscope operating conditions, bringing to attention the difficulties of obtaining meaningful signals and interpreting those signals. The significance of back-scattered electrons in interpreting changes in elemental composition of fibers/materials is introduced, and the importance of x-rays for elemental analysis is emphasized. Goynes concludes with examples of textile characterization using SEM as a powerful tool. It is well known that surface morphology and characteristic structural features of fibers are dramatically revealed by scanning electron microscope; however, Goynes also presents the effects of physical and chemical treatments on changes in the fibers' characteristic features. This characterization method also provides valuable information regarding process evaluation and product quality control.

Chapter 4 focuses on analytical pyrolysis as a technique to identify and detect small changes in polymers, fibers, and other textile auxiliaries. Analytical pyrolysis (or thermolysis) is a nonoxidative process in which polymers or large molecules break down into characteristic smaller molecules. Instrumental analysis of these pyrolysates, which are structure-specific volatile compounds, provides information about the structure and identity of the parent compound. I. R. Hardin discusses the mechanism of pyrolysis, the types of reactions that occur to give rise to complex mixtures of products, and how these volatile fragments are separated and analyzed using gas chromatography (GC) alone or in conjunction with mass spectrometry or Fourier-transform spectroscopy. He elaborates on these techniques with examples of identifying or detecting small changes in polymers, finishes, and dyes.

Chromatographic and spectroscopic methods are employed for characterization of a wide variety of polymers, fibers, textiles, and textile auxiliaries. In Chapter 5, Y. Yang presents the scientific basis and application of conventional liquid chromatography (LC) for dye identification, separation, and purification. Also, as a powerful tool, LC is employed for analysis of textile finishing processes such as flame retardant, stain resistant, durable press, and others. Packing textile material into the column as a stationary phase is an innovative method for the investigation of pore structure and dyeing and finishing behavior of the specific textile em-

ployed as a stationary phase. This technique is useful as well for studying dyeing and finishing mechanisms in textile systems. Yang provides the basic concepts of liquid chromatography as a tool for textile and related materials characterization, and focuses on pore structure and surface area analysis as it relates to textile wet processes. The subjects of color identification, separation and purification, dyeing thermodynamics, sorption isotherms, dye compatibility and dye-fiber interactions are discussed in depth. In a related topic, K. R. Beck, in Chapter 6, focuses on characterization of durable-press finishes for cellulosic textiles using chromatographic and spectrophotometric methods. Beck, a pioneer in the use of chromatographic techniques for analyzing textile finishes, describes analysis of durable press chemicals utilizing thin-layer, gas, and high-performance liquid chromatographic methods as well as spectroscopic methods. The spectroscopic methods included are ultraviolet-visible, near infrared, infrared, nuclear magnetic resonance, and mass spectrometry. Beck illustrates the use of these methods in determining molecular structure, mixture composition, and properties of durable press agents, as well as the mechanism of cross-linking reactions.

In Chapter 7, N. R. Bertoniere describes a technique based on the principles of gel-permeation chromatography. Her focus is on the development of reverse gel permeation column chromatography to assess pore size distribution in cotton cellulose. This method was developed at the Southern Regional Research Center, New Orleans, La. over a period of years by Bertoniere and associates. Bertoniere describes the experimental problems with columns made from cotton cellulose by various methods and proposes meaningful solutions. Reverse gelpermeation chromatography as a tool to elucidate pore structure in different varieries of cotton and jute fibers is described. The effects of caustic mercerization and liquid ammonia treatment on pore size distribution of cotton are explained; the progressive losses in the accessible internal volume of cotton with increasing the degree of cross-linking is used to illustrate increases in resilience accompanied by losses in strength. Of significance is the use of this method in following the differences among conventional cross-linking agents and formaldehyde-free cross-linking agents with respect to the degree to which they alter the pore size distriburion in the cross-linked cotton. Bertoniere explains why formaldehyde-free reagents differ in the weight add-on required to impart easy care performance to cotton fabric. Research in this area is ongoing.

Chapter 8, authored by L. Rebenfeld et al., focuses on characterization of pore structure in fibrous networks as it relates to absorbency. They discuss the discontinuous nature of textile materials, their heteroporous nature, and the deceptively high level of porosity in textile materials—which is directly related to absorbency. Nevertheless, the porosity of a textile material is strongly affected by lateral compressive forces to which the material is subjected, hence the pressure dependence of liquid absorption characteristics of textiles. While porosity is an important physical quantity, the dimensions of the pores give a more descriptive

way of characterizing the porous nature of a network. Rebenfeld and associates delineate pore volume, which determines liquid absorption capacity, from geometric considerations such as pore throat dimensions that influence liquid flowthrough processes, which in turn affect filtration or barrier properties of porous materials. On the basis of the heteroporous nature of fibrous materials, they introduce the concept of pore sizes and their distribution as unimodal, bimodal, and trimodal. To characterize the pore structure in terms of pore volumes and pore throat dimensions they describe the instrumentation of mercury porosimetry used until recently, and the new instrumentation developed at the Textile Research Institute by the authors. These analytical methods are particularly well suited for textiles and other compressible planar materials.

Another topic that has presented much difficulty in the past is that of characterizing single fibers as to their mechanical properties. S. Kawabata, a renowned researcher in the area of polymers, fibers and textiles, presents in Chapter 9 the theoretical basis of direct measurement of the mechanical properties of single fibers. Kawabata describes the advantages of direct "micromeasurement" of single fiber mechanical properties and discusses anisotropy in mechanical properties and the difficulties in measuring very small force and deformation in a single fiber. The mechanical anisotropy of the fiber strictly reflects the microstructure of the fiber and has great implications on the micromechanics of fiber/resin composites. Kawabata also presents the instrumentation developed by the author for this purpose.

The next four chapters focus on new developments in analyzing textile attributes (handle, color, protective qualities) that are not easily measurable as compared to specific textile properties. Chapter 10 deals with objective measurement of fabric hand. S. Kawabata and M. Niwa, the leaders in this area of research, present the significance of fabric hand or handle evaluation on the perception of garment appearance, comfort and tailorability. They analyze and correlate fabric hand judgments by experts with specific fabric properties that express fabric hand characteristic and that can be measured objectively. This is described as objective system for hand evaluation. The nonlinear mechanical properties of a fabric that describe fabric hand, including the weighting system for these properties and the equations that describe these weighting systems, are presented. The mechanical parameters are measured by a set of four instruments known as the Kawabata system or KESF system. Recently, an automated KESF system has been developed.

Color and colorimetry is another elusive but rapidly evolving area of study. P. T. F. Chong, in Chapter 11, provides an extensive background in basic colorimetry and describes the color measuring systems, as well as the developments in color measuring instruments. On the basis of his extensive experience as a color scientist, Chong provides valuable insights into instrument setup, calibration, and verification, as well as sample preparation and color measurement. This is followed by an in-depth presentation of the application of color measuring systems

in the textile and textile-related industries. The major applications discussed are color matching, color quality monitoring or screening the color of the products against preset tolerance in color requirement, colorant strength evaluation, and whiteness/yellowness evaluation. Chong also discusses aspects of colorant solution evaluation including colorant strength, dye solubility, solution stability, dye exhaustion characteristics and so on.

Chapter 12 deals with characterization of chemical barrier performance of textile systems. J. O. Stull describes the types of barrier materials, standards pertaining to chemical barrier performance of these materials, and an overview of barrier testing approaches. Three testing approaches are discussed in detail; those pertaining to resistance of material to degradation, chemical penetration resistance, and permeation resistance. The complexities of textile substrate (homogeneous single layer, coated, laminated, microporous, or containing adsorptive components), testing techniques, test conditions, and the impact of multicomponent chemical challenges are brought to focus. For example, using different test methods, or even the same method but different test conditions, can provide different results for the same material and chemical combination. Thus, selection of test method and conditions must be appropriate to the product's application and expected performance.

Degradation resistance testing may show how material/products deteriorate or are otherwise affected, but will not always demonstrate retention of barrier characteristics with respect to specific chemicals. Degradation testing is most useful when retention of specific physical properties is desired or as a screening technique for other chemical barrier testing techniques. Penetration testing should only be used if the wetting or repellency characteristics of materials are to be evaluated. This type of testing is appropriate for the evaluation of material performance against liquid chemicals and can be used for microporous and continuous filmbased materials. Vapor transmission test methods are used to measure gross vapor penetration of chemical vapor or gas challenges over relatively short periods of time. This characterization technique is applicable to any film-based material or adsorbent-based material. Chemical permeation testing, however, provides a barrier material's total chemical resistance and can detect very small amounts of permeating chemical. Thus, permeation testing provides the most rigorous of all chemical resistance test methods. Several techniques are presented to provide flexibility in test conditions and applications. Since there are a number of techniques to characterize the barrier performance of materials, careful selection of a test method and its parameters depends on the understanding of the material (textile/ product) and its application.

In Chapter 13 P. L. Brown introduces a topic of much interest and concern among health care providers and others, the barrier properties of textiles against microorganisms. Recently, the focus on preventing transmission of infectious microorganisms through barrier materials has grown to include both infection con-

trol and personal protection. One major reason for this growth is the risk associated with exposure to blood-borne pathogens as perceived by the health care community. Other potentially hazardous microorganisms (not blood-borne) include Prions, Muerto Canyon virus, and multiple-drug-resistant forms of *Mycobacterium tuberculosis*, staphylococci, and enterococci, to name a few. In addition, biotechnology workers dealing with recombinant DNA, laboratory technicians handling cultures of human pathogens, and veterinary and agricultural workers dealing with zoonotic agents also risk exposure. However, each work environment with potential microbiological hazard may require a different strategy and risk reduction decision.

The basic performance objectives of personal protective clothing products against biohazards are allowing fluid flow, such as air or liquid, while limiting the transfer of potentially pathogenic microbes being transported with them, or else preventing the transfer of fluids and indirectly preventing the transfer of microbes. These two objectives are fundamentally different and require different experimental approaches to the analysis and characterization of the barrier properties of the respective materials to microorganisms. Brown, with his extensive experience as a research scientist and protective product specialist, provides an extensive theoretical background about the types of biohazards, textile substrates, and characterization methods for assessing barrier properties of textiles. He discusses the limitations of laboratory test methods and emphasizes the need for understanding the different microbial, physical, chemical, and thermal stresses imposed on textiles (and finished products) used in personal protection and infection control.

Recognizing the complexities of the different end-use environments for microbial barrier textiles and various stresses that can be imposed on their barrier integrity, Brown discusses developing a realistic strategy related to product evaluation in the laboratory. He suggests developing a feasible testing hierarchy based on combinations of various tests. The degree of hazard associated with exposure to the microbes will dictate how carefully the end-use application for the textile will need to be investigated, how conservative the modeling and experimental approach should be, and the definitions for adequate versus inadequate microbial barrier performance. The ultimate goal is reduction of the risk of product failure during actual use.

In summary, this volume focuses on current and evolving methods of characterizing selected attributes of fibrous materials that are difficult to predict by employing a single standardized test method.

2—
Polymer Characterization

Phillip H. Geil
University of Illinois at Urbana-Champaign, Urbana, Illinois

Polymer characterization can be divided into three areas: (1) chemical structure, including composition and configuration; (2) physical structure, including such interactive factors as degree of crystallinity, crystal structure, defects and disorder, conformation, and morphology, and (3) properties, primarily physical but also chemical. In this chapter, I summarize traditional methods of characterization, with references to permit readers to obtain further details of both background and methods, and describe in somewhat greater detail newer methods, all with particular emphasis on techniques applicable to synthetic textiles and textile polymers. For most of the methods I assume an understanding of the terminology and basis for the traditional techniques; such as, for x-ray diffraction, unit cell, crystal structure, Bragg's law, reciprocal lattice, and Ewald's sphere. An excellent recent compilation of polymer characterization techniques is given in Ref. 1.

I—
Chemical Structure

In this section the composition, configuration, and molecular weight (average and distribution) are considered. The basic techniques for all of these can be considered traditional, with improvements primarily in instrumentation. Since there are numerous discussions in general and specific texts, I only summarize them here.

Of first concern is "purification" of the polymer, that is, separation of the polymer from additives, catalyst residue, and impurities, with characterization of all of these often being of interest. This is often difficult in concept and reality for polymers. Methods include [2,3]:

1. Extraction, generally by use of nonsolvents for the polymer, to remove additives, etc. Of concern is the ability to determine completeness and the time required.

2. Solution reprecipitation, to improve purification. Problems include variation in solubility with molecular weight, as well as dependence on branching, cross-linking, tacticity, and crystallinity, separation by which may or may not be desired. For common polymers the *Polymer Handbook* [4] lists potential solvents (see also Ref. 3).

3. Separation, to remove nonpolymer impurities and separate low-molecular-weight fragments produced by analytical, chemical, or thermal degradation. For polymers, separation generally uses liquid/solid (e.g., thin layer, TLC), liquid/liquid, ion exchange, and gel permeation chromatography (GPC) techniques, with the sample inserted following dissolution. TLC, for instance, is simple, rapid, and effective but yields only microgram quantities for subsequent characterization. GPC, especially preparative GPC, yields larger samples. Although usually used for molecular weight fractionation (see later discussion), it is also useful for variations in chemical structure.

A—
Composition—Elemental Analysis and Substitutional Groups

Elemental analysis, based on traditional analytical chemistry techniques for low-molecular-weight systems (e.g., combustion), is the usual basis for comparison and calibration of other techniques (see, e.g., Ref. 3). Some journals, such as *Macromolecules*, require elemental analyses for monomers and polymers described in synthesis papers. Atomic absorption spectroscopy, as well as a variety of other techniques, can be used for trace elements, such as from unseparated catalyst residues and stabilizers, with x-ray dispersive analysis, in a scanning (SEM) or transmission electron microscope (TEM), usable for elements (of higher mass than carbon) in particulate additives and impurities [e.g., 5]. In the SEM, x-ray dispersive analysis (see Chapter III), for example, can be applied to particulates on the surface of fibers while in the TEM, sections or specially prepared thin films would be used in the STEM mode.

For determination of substituent groups (e.g., CH_2, C=O, C=C, etc), standard chemical methods can be used either after breakdown of the polymer (with care to insure against changes in the groups to be tested) or on the polymer itself [2,3]. The methods involve reaction of specific groups with known reagents. More frequently used are infrared spectroscopy techniques (IR) and, increasingly since the 1980s with the development of high-speed computers, Fourier-transform IR (FTIR). As will become obvious, IR is a technique of broad applicability for both chemical and physical characterization of polymers. As discussed in numerous texts (see, in particular, Refs. 6–8 and other references therein as well as Ref. 1), IR absorption is due to excitation of the vibrational motion of groups of nuclei. An IR absorption band, with an intensity proportional to the number of groups in the beam, can be observed for each vibrational degree of freedom (normal mode, type of motion) of a molecule for which the induced or real dipole interacts with the in-

cident light, absorbing energy. Secondary requirements are that the band can be resolved from other bands, now greatly simplified with, for example, deconvolution programs available in FTIR systems, and the intensity is strong enough to detect.

In the complementary Raman spectroscopy technique (for general Raman references related to polymers, see Ref. 1, Chapters 21 and 42), a change in polarizability of the molecule results in inelastic (incoherent, change in wavelength) scattering of the incident beam (usually visible or near IR, laser light). Symmetric vibrations of, for example, a linear CO_2 molecule give rise to Raman scattering, while nonsymmetric vibrations give rise to IR absorption; furthermore, polar bands yield strong IR absorption while nonpolar bands do not. Thus the C-C polymer backbone (or similar bonds in the centrosymmetric O_2 and N_2 molecules) does not absorb in the IR, while substituted groups with C-H, C-F, and C=O, because of differences in electronegativity of the atoms, are polar and absorb strongly. The symmetrical vibrations, on the other hand, scatter Raman strongly. In both cases individual groups will absorb or scatter radiation at a number of unique frequencies, with these "characteristic group frequencies" permitting characterization of the samples composition.

Consider the CH_2 group. Its vibrations (Fig. 1), as for other similar types of groups, can be classified as follows, with the frequencies given in the figure:

1. Valency or stretching vibrations (symbol ν) result in a change in one or more (few) bond lengths, and may be symmetrical (ν_s) or asymmetrical (ν_{as}).

2. Planar deformation or bending vibrations (δ) result in a change in one or more bond angles with approximately constant bond lengths.

3. Nonplanar deformation vibrations (γ,ρ,τ,) result in a complex change in several angles, with bond lengths nearly constant. Examples include wagging (pendulum vibration perpendicular to the CH_2 plane, symbol γ), rocking (pendulum vibration in the CH_2 plane, symbol ρ), and twisting (rotational vibration about the CH_2 symmetry axis, symbol τ).

The characteristic group frequencies of hydrocarbons are shown in Figure 2. The CH_2 δ vibration (bending, 1460 cm^{-1}, below the range of the figure) is essentially independent of the number or sequence of CH_2 groups or the physical state; it is thus a good internal thickness band for calibrating the amount of sample in the beam if isolatable from neighboring bands. There is some shift, to 1440 cm^{-1}, when the CH_2 is adjacent to an unsaturated C and 1425 cm^{-1} when adjacent to a carbonyl group. On the other hand, the γ, ρ, and τ vibrations are very sensitive to the local environment of the group and thus can be used for determination of configuration (discussed later). Catalogs of characteristic group frequencies are available for both low [11] and high [2,12] molecular weight materials as well as in the computer library systems available for the IR instruments. The latter permits spectral matching.

Methods of polymer sample preparation for FTIR are diagrammed in Figure 3 (see Ref. 8 for details). Of these, the transmission and reflection techniques are

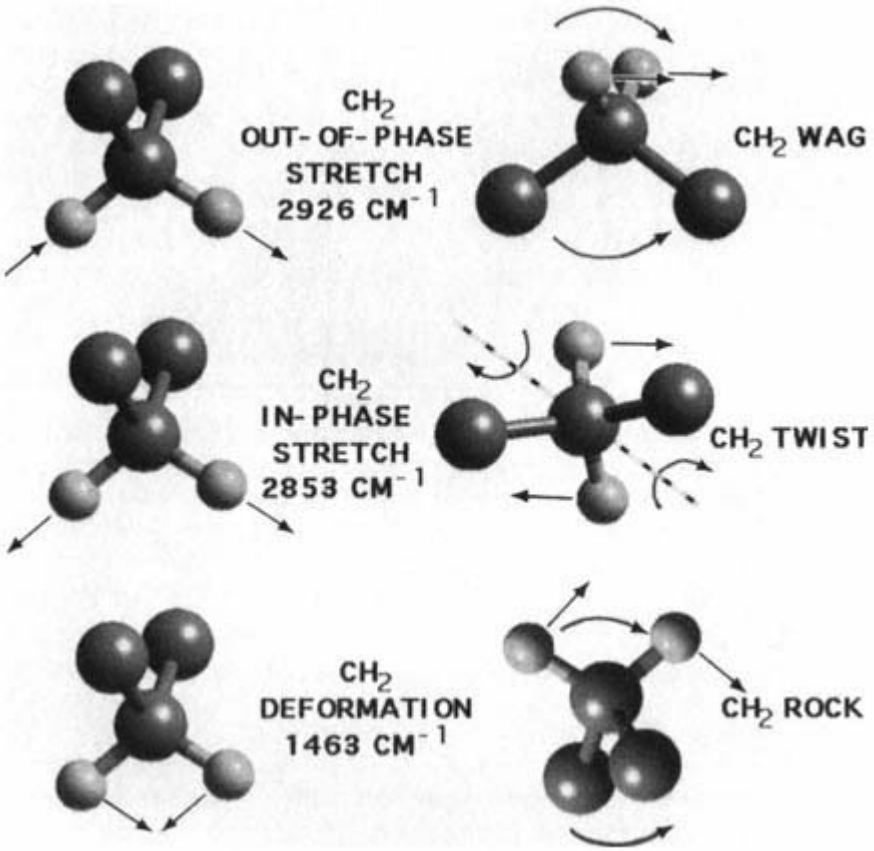

Figure 1
Examples of CH_2 group vibrations (normal modes). The small circles represent H atoms, and the large C atoms with the upper C atoms on the left, for instance, being the next C atoms along the chain.
(Modified from Ref. 9.)

of the most use for fibers. Standard transmission methods, using thin molded or drawn films, require uniform-thickness, nonscattering films. Fibers can be used by, for example, laying them parallel to each other on a window or wrapping them on a frame and coating with Nujol (an oil of low absorptivity in the regions of interest) to reduce the scattering. In addition to normal reflectance techniques, including attenuated total reflectance (ATR), diffuse reflectance (DRIFT) techniques have also proven useful. The photoacoustic spectroscopy (PAS) technique can also be used and is rapidly growing in use for samples, such as fibers, that have high scattering. It can depth-profile changes in compositions, such as induced by oxidation. A particularly useful recent advance is the development of FTIR

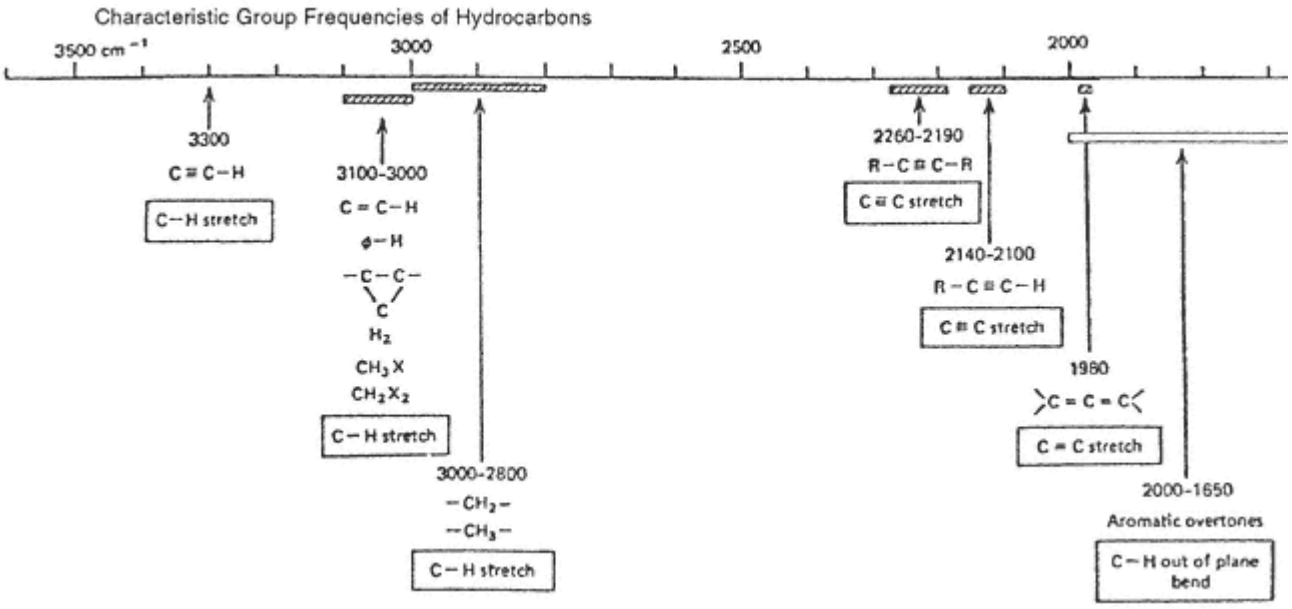

Figure 2
Characteristic group frequencies of hydrocarbons. The various types of groups shown absorb IR in the spectral ranges shown, and the position of the peaks in the ranges is a function of attached groups and the local environment.
(From Ref. 10a. More extensive charts are given in Ref. 10b.)

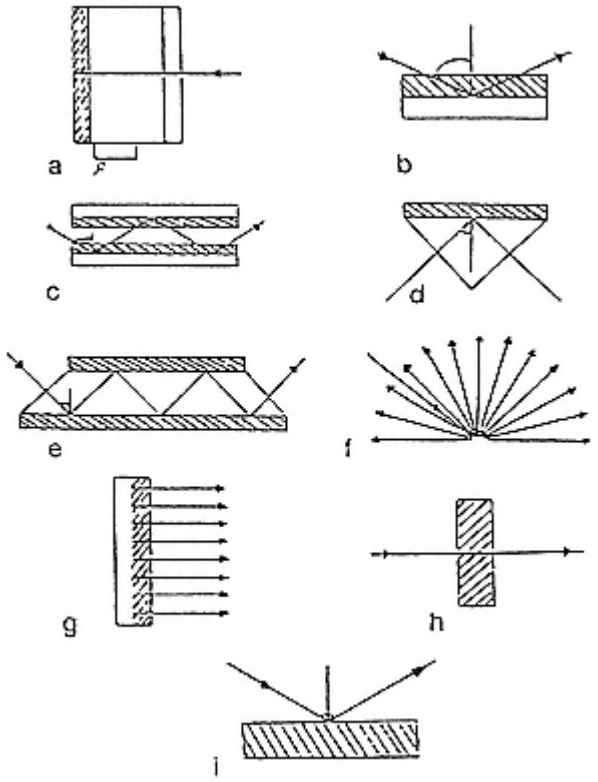

Figure 3
Diagrams of FTIR sampling techniques (a) Photoacoustic spectroscopy (PAS). Pressure fluctuations induced by the incident IR are detected by a sensitive microphone. (b,c) Specular or external reflection spectroscopy (RA). An IR beam passing through the sample at a steep angle (70–89.5°) is reflected from a mirror-like optical substrate one (b) or more (c) times. Useful for coatings. (d,e) Internal reflectance or attenuated total reflectance spectroscopy (IRS or ATR). The beam is transmitted through a high-refractive-index, low-absorptivity crystal (e.g., Ge) and is reflected once (d) or several (e) times at the crystal-sample surface. The method samples a depth of 0.5μm of the sample's surface and can be used for opaque samples. (f) Diffuse reflectance spectroscopy (DRIFT). The scattered light is reflected from mirrors to the detector. Useful for fibers. (g) Emission spectroscopy. The emission spectrum of a sample is the mirror image of its absorbance spectra. Useful for metals, opaque samples and fibers for $\nu > 2000\ cm^{-1}$; sample needs to be at thermal equilibrium. (h) Transmission spectroscopy. For films, or powdered samples dispersed in KBr pellets or suspended in an inert (to IR) oil on a window. (i) Spectral reflectance spectroscopy. Reflectance from the surface of the sample with angle of reflection equaling angle of incidence. Not useful for fibers. (From Ref. 8.)

microscopy, that is, the attachment of an IR microscope to an VTIR unit. Tills permits the observation (by visible light) and characterization of an individual fiber.

The other primary method of characterizing the substituent group composition is nuclear magnetic resonance (NMR) spectroscopy (and FT-NMR) [see Refs. 1 (Chap. 17), 8, and 13)]. In NMR the sample is placed in a slowly varying strong magnetic field H_0 while an oscillatory smaller field of frequency v_1 and constant maximum strength H_1 is applied at right angles (or H_0 and H_1 can be held constant while v_1 is varied). Energy is absorbed from the H_1 field when

$$H_0 = \frac{Ih\nu_1}{\mu} \qquad (1)$$

where

I = the spin quantum number

h = Planck's constant

μ = the magnetic moment of the nucleus involved

For polymers the nuclei of interest, ^{1}H, ^{13}C, ^{19}F, and ^{17}O, all have spin (I) = 1/2 and thus two energy states, with the magnetic moments parallel (low energy) or antiparallel (high energy) to the applied (H_0) field.

Consider a single proton (^{1}H) in the sample. If isolated it will absorb energy when H_0, as it increases, becomes equal to $Ih\nu_1/\mu$ (in actuality a small number of the excess nuclei in the lower energy state "flip" their spins to the higher energy state). However, if neighboring bonded or nonbonded nuclei have a magnetic moment ($I > 0$) their fields (H_{loc}) will add (vectorially) to the applied H_0 field. If the internuclei vectors are stationary, as at low temperature, the result is absorption over a range of values of H_0, each nucleus absorbing when the field at its position is

$$H'_r = H_0 + H_{loc} = \frac{Ih\nu_1}{\mu} \qquad (2)$$

That is, a broad energy absorption line is observed. On the other hand if the internuclei vectors rapidly randomize in space, as in solutions or melts, the local field due to the neighboring nuclei averages to zero and a narrow line would be observed at the characteristic value of H_0 except for the influence of the magnetic moments of the electrons around the nucleus.

The electrons surrounding the nucleus produce a local field H_{loc} proportional to the applied field, and in the opposite direction

$$H_{loc} = -\delta H_0 \quad \text{and} \quad H_r = H_0(1 - \delta) \qquad (3)$$

where δ is the shielding constant and is a measure of the chemical (bonded) environment of the nucleus. For example, the ^{1}H devoid of electrons, as in  groups, have small δ and thus absorb at applied fields close to (but above) that

given by Eq. (1), that is, when $H_r^* = H_r = H_0(1 - \delta)$. On the other hand the ^1H in $>CH_2$ groups have a large δ, the electrons shielding the nucleus, and therefore a larger H_0 is required before H_r^* is reached (i.e., resonance is obtained). The resonant field is "shifted."

Figure 4 shows the characteristic chemical shifts (in parts per million of the applied field since the shift is proportional to the field) with tetramethylsilane, in which the ^1H are more shielded than in any other organic compound being used as a standard. Its shift is defined as 10 ppm (τ scale) or 0 (σ scale), with all other resonances occurring at lower values of H_0.

With the development of FT-NMR it became possible to use ^{13}C despite its much lower abundance (relative to ^{12}C and ^1H). The advantage lies in the much larger shift, ≈ 600 ppm, versus <20 ppm for ^1H, permitting higher resolution. The general ^{13}H chemical shift chart is shown in Figure 5, ^{13}C spectroscopy is generally being used these days. Again, computer libraries aid spectra characterization.

Measurements of the chemical shifts for a polymer permit determination of its group composition, with the energy absorbed by a group (peak area) being proportional to its concentration. (For examples see Figs. 12–16.)

The chemically shifted lines in modern, high-resolution (large H_0) instruments are further split by spin-spin coupling (see later discussion) permitting determination not only of the constituent groups but also of their neighbors along the chain. So-called narrow-line NMR spectra (i,e., permitting resolution of both the chemical shift and spin-spin coupling) are most often obtained from solutions of the polymer, where the solvent should be devoid of the groups being measured in the polymer. This often requires deuterated (^2H) solvents for ^1H NMR and purified ^{12}C solvents for ^{13}C NMR.

Despite the broadening of the resonance band in solids, narrow-line spectra can be obtained by a combination of so-called "magic angle spinning" (MAS), in which the solid (fiber) sample is spun rapidly about an axis oriented at 57.4° to H_0, dipolar decoupling (DD), and cross-polarization (CP) (see Fig. 16a) techniques. For further description of this so-called "grand" experiment and its limitations (e.g., the chemical shifts may be affected by the conformation of the group involved) and of other special editing techniques (applications of various pulse sequences) applied to solution samples to enhance the resolution (over and above that resulting from higher H_0) and permit assignment of the peaks to the appropriate chemical groups the reader is directed to Ref. 8 or 15.

Ultraviolet (UV) and visible spectroscopy have more limited usefulness; many polymers show no absorption in the visible or near-UV range. Table 1 lists the groups whose absorption can be measured; in many cases these groups are formed by degradation during processing.

Group composition on surfaces of polymer samples, including fibers, can be determined by a number of techniques in which the surface is irradiated with

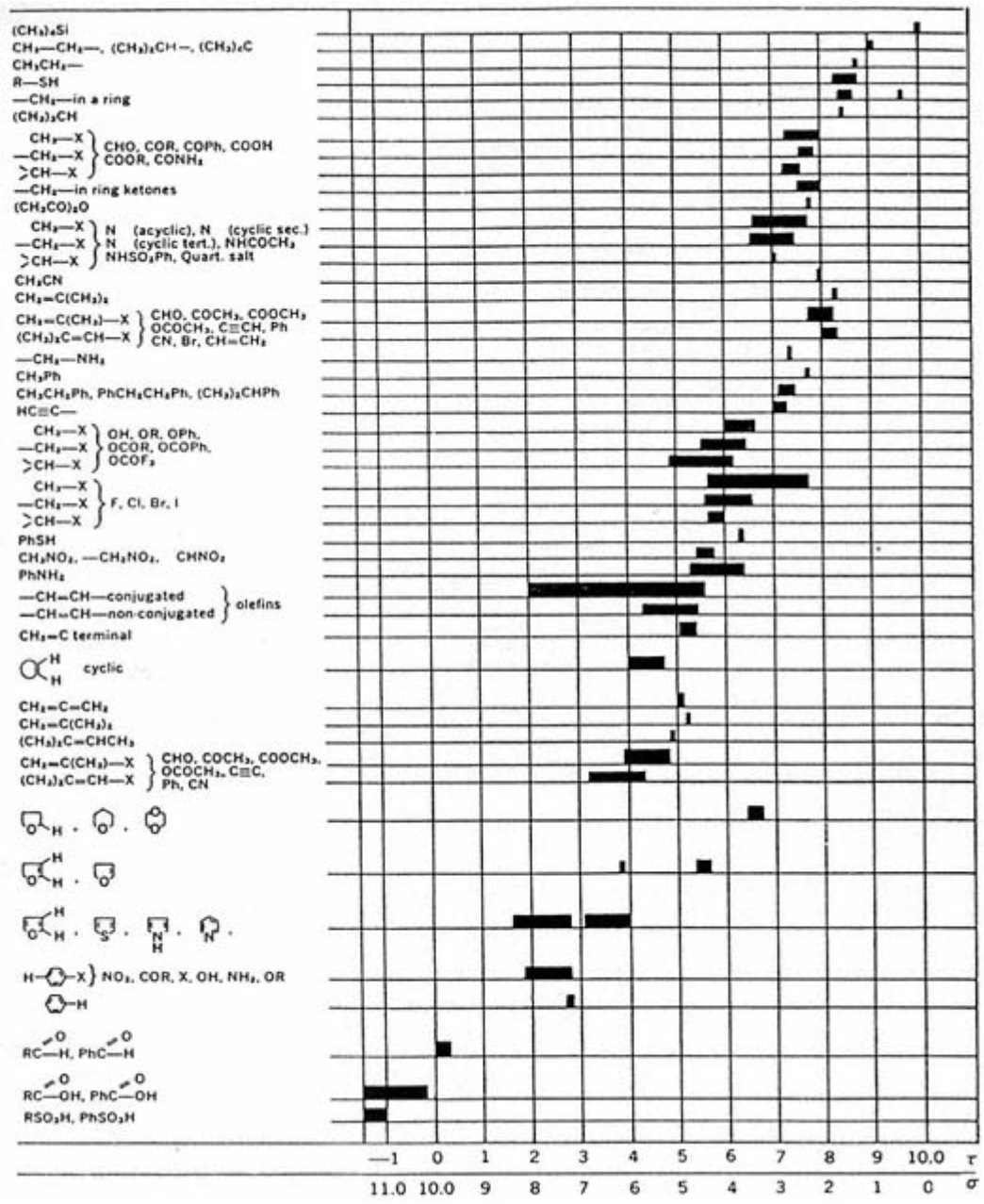

Figure 4

Characteristic NMR chemical shift spectral positions for ^{1}H in organic materials. Scale is in parts per million shift relative to $(CH_3)_4$ Si (top of list). (From Ref. 14b.)

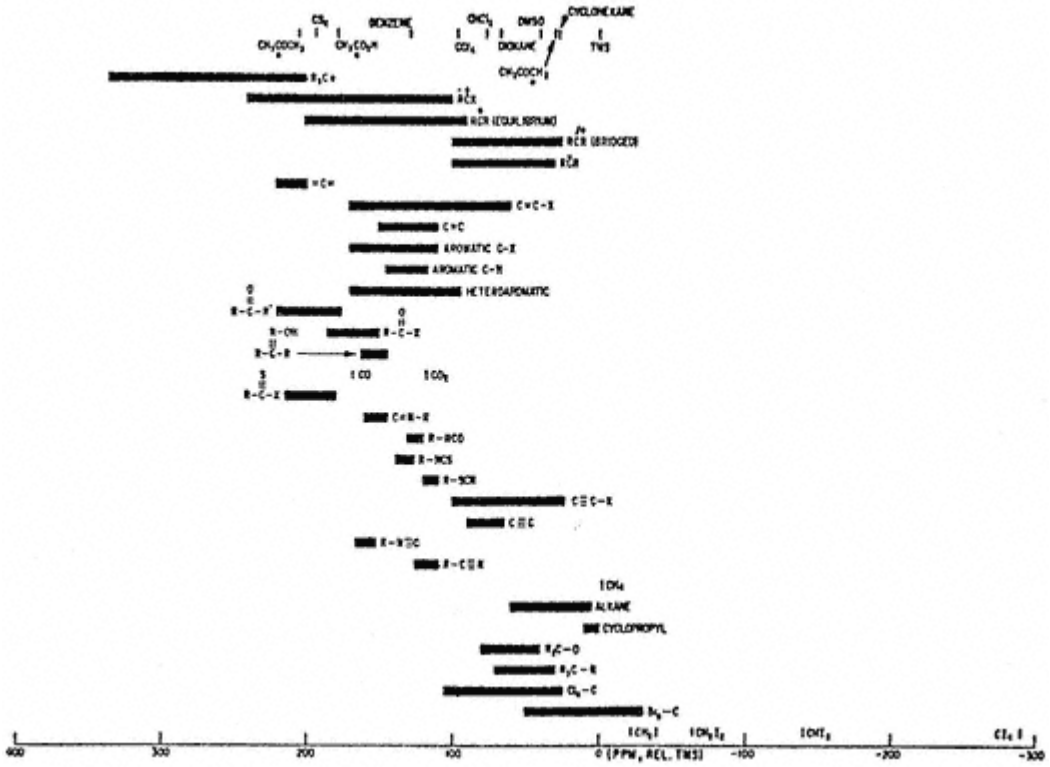

Figure 5
Characteristic ^{13}C NMR chemical shift spectral positions; the zero is relative to $(CH_3)_4$ Si (TMS).
(From Ref. 10a.)

Table 1 UV Absorption Ranges of Important Groups

Group (bond)	Absorption range (nm)	Transition energy (kJ/mol)
C-N (Amide)	250–310	478.8–386.0
C=O	187; 280–320	640.1; 427.5–373.9
C-C	195; 230–250	613.8; 520.4–478.8
O-H	230	520.4
C=C (isolated double bond)	180	665.0
-$[CH=CH]_n$- (conjugated double bond)		
n = 2	230	520.4
n = 3	275	435.3
n = 4	310	386.0

Source: Ref. 7.

photons (usually x-rays), electrons, or ions, with the energy of the resulting emissions being atom and group dependent. These techniques are of particular interest for the characterization of coatings, degradation effects, and surface treatments [see Refs. 1 (Chap. 24), 7 and 16]. For instance, in electron spectroscopy for chemical analysis (ESCA, also known as XPS, x-ray photoelectron spectroscopy) the sample is irradiated with monochromatic x-rays, knocking out electrons whose energy (which is measured) is characteristic of the atom type, electron shell from which removed, valency, and neighboring bonded atoms (i.e., group) (Figures 6 and 7). Other examples are Auger electron spectroscopy (AES), in which the excitation is by electrons, with resulting electron energies being measured, and secondary-ion mass spectroscopy (SIMS), in which ions are used to knock out ions whose mass is measured by a mass spectrometer. Depths characterized vary from a few atomic layers for SIMS to <30 layers for AES and <50 for ESCA. ESCA is particularly useful for polymers since, due to the use of x-rays, charging does not take place.

B—
Configuration

Considered here is the arrangement along the chain of the constituent groups, that is, the microstructure of the chain. Included are sequence arrangement in copolymers, tacticity, cis-trans isomerism, and branches and cross-links. IR and NMR

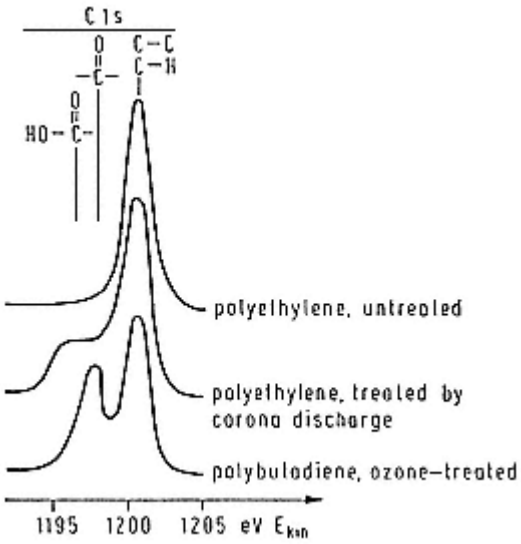

Figure 6
C_{1s} ESCA photoelectric spectra from the surface of the samples listed.
(From Ref. 17.)

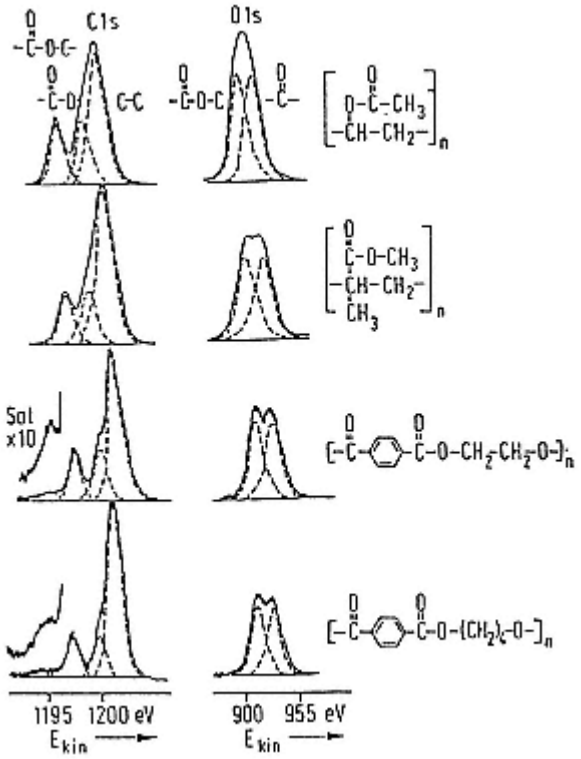

Figure 7
C_{1s} and O_{1s} ESCA spectra of polyvinyl acetate, PMMA, PET, and PBT.
(From Ref. 16.)

are again the primary techniques, with the absorption frequencies of the constituent groups being shifted slightly, depending on their neighbors.

In IR we have already noted the shift in the CH_2 δ (bending) band as a result of its neighbors. The γ, τ, and ρ bands are particularly sensitive to their local environment. Figure 8 shows the shift in frequency of the CH_2 rocking mode, while Figure 9 shows how it can be used to determine the configuration of an ethylene-propylene copolymer. In practice only a sequence distribution can be obtained, averaged over all of the chains in the sample. Table 2 lists the important IR group frequencies used for structure determination, while Figure 10 shows a detailed correlation table for the C=O ν vibration. As an example of IR's use for tacticity determination, Figure 11 and Table 3 show its use for predominantly isotactic and syndiotactic PMMA. All of the IR sample preparation techniques shown in Fig. 3 can be used. Although Figs. 8–11 are all examples of IR's use for characterizing configuration, differences in conformation (e.g., trans vs. gauche and different he-

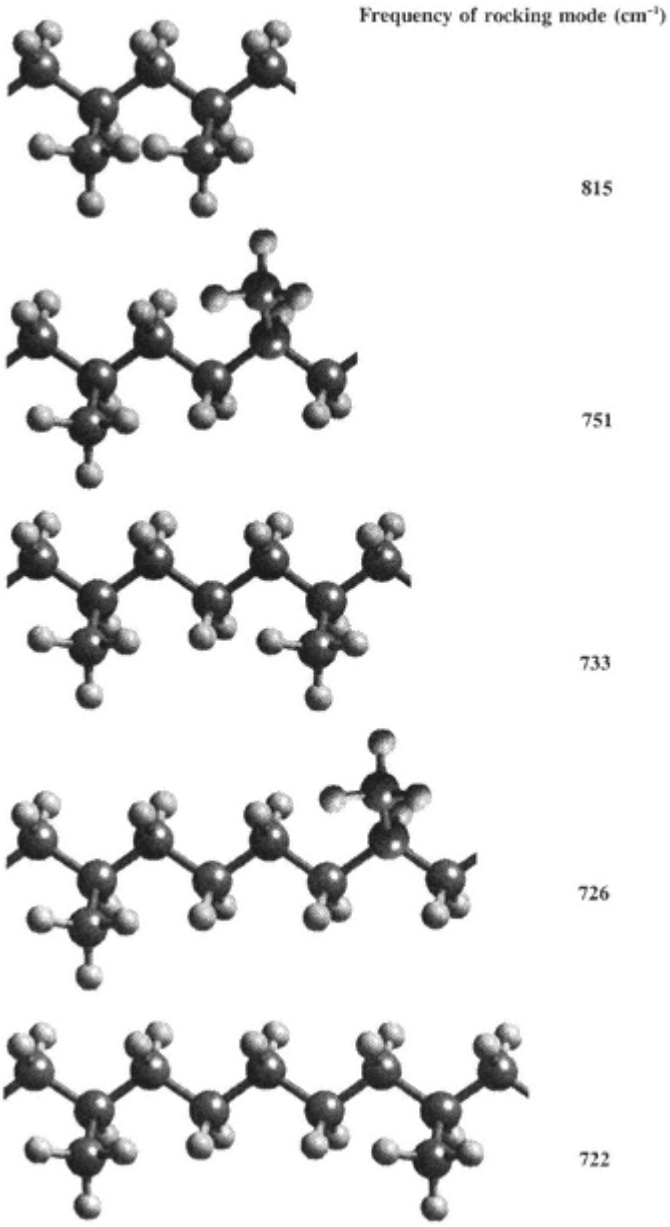

Figure 8
Frequency of the rocking mode as a function of number of CH_2 groups between "anchors" as determined from model compounds (data from Ref. 18). For more than 5 CH_{2s} absorption is also at 522 cm^{-1}.

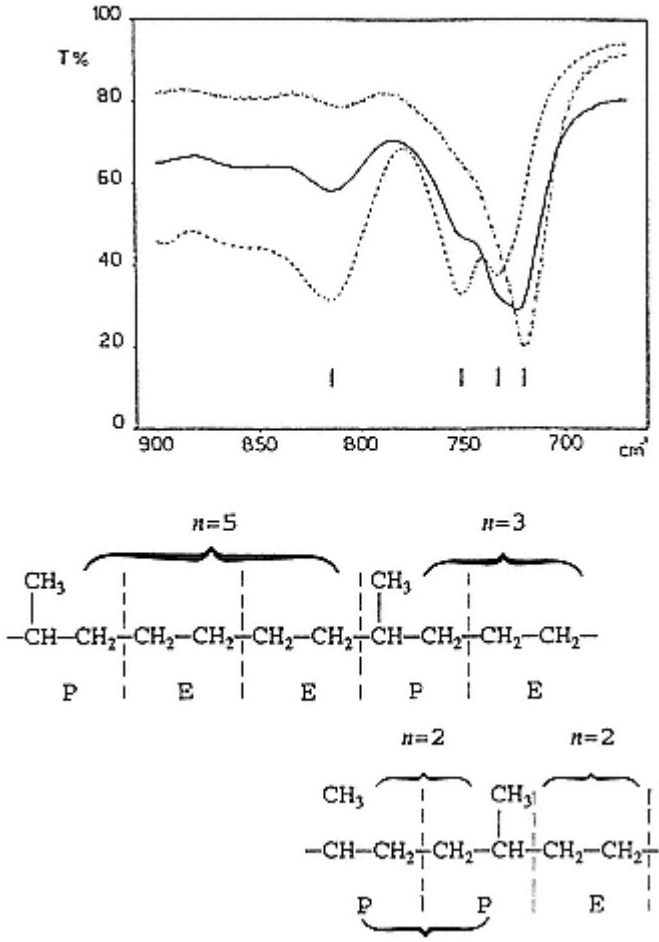

Figure 9
IR spectrum of ethylene propylene copolymers of 25% (-.-), 50% (—), and 75% (----) propylene composition in the CH_2 rocking region of the spectrum (compare with Figure 8). In pure PP the CH_2 rock band is 815 cm^{-1}. The presence of the 752 cm^{-1} band indicates reversal of PP chain direction, either by propylene tail-to-tail addition or by ethylene insertion between propylene heads.
(Graph from Ref. 18.)

lical forms as well as crystalline vs. amorphous, all as described in Section II) can also cause changes in absorption band position. Separating these effects is of concern and requires complementary use of other techniques.

Branches (from either the end groups or branch points and crosslinks) can also be identified by IR. An example is shown in Figure 12 for polyethylene (PE)

Table 2 Important IR Group Frequencies

Average band position (cm^{-1})	Assignment	Remarks
3500	OH stretching	Broad band
2950, 2890	CH_2 stretching	Strong polymodal band
2260	NCO stretching (isocyanate group)	Strong band
1850–1650	C=O Stretching (carbony1 group)	Very strong band, position varies according to environment (e.g., ketone aldehyde, ester)
1620	C=C stretching	
1600	NH bending	Important indication of polyamides
1450	CH_2 bending ("scissoring")	
1100	C-O stretching (ether group)	
1000	C-C stretching (skeletal vibration)	
900–700	Benzene ring, CH out-of-plane vibrations	Two to three usually strong characteristic bands, positions depend on type of substitution
815	triazine ring out-of-plane vibration	Very sharp band
700	Carbon-halogen stretching	

Source: Ref. 7.

(BPE = branched or low-density polyethylene vs. LPE = linear or high density polyethylene). The CH_3 1378 cm^{-1} band is due to CH_3-capped branches. It is, however, overlapped by several CH_2 bands (1304, 1352, and 1368 cm^{-1}), making the determination of the background difficult. Determination can be made either by subtraction of a (thickness-corrected) LPE spectrum or by deconvolution of the bands. However it must be noted that the absorbances of the CH_3 groups depend on the length of the branch to which they are attached (1.55:1.25:1 for CH_3 on methyl, ethyl, and longer branches). Thus the IR measurement is only a weighted average; high-resolution NMR can be used (see below) but is too expensive for general use, and thus the IR scale is commonly used.

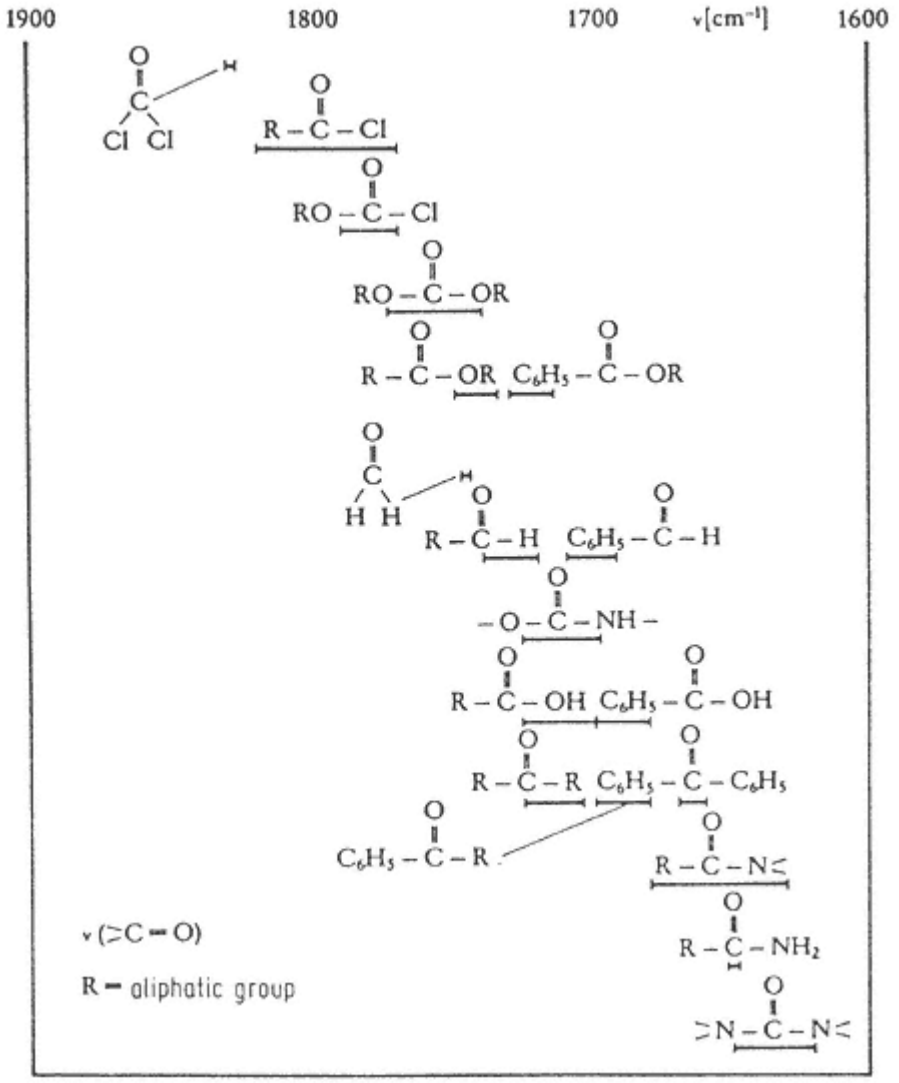

Figure 10
Correlation (*v* range in which observed) table of C=O stretching vibrations as affected by neighboring attached groups.
(From Ref. 19.)

NMR is, in general, an even more sensitive sequence characterization technique. In addition to the chemical shift effect described earlier, the-electrons around a nucleus produce additional, smaller (spin-spin coupling) shifts due to the effect of the magnetic moments of neighboring, nuclei whether or not the internuclear bonds are stationary or rapidly randomizing in space. The electron in

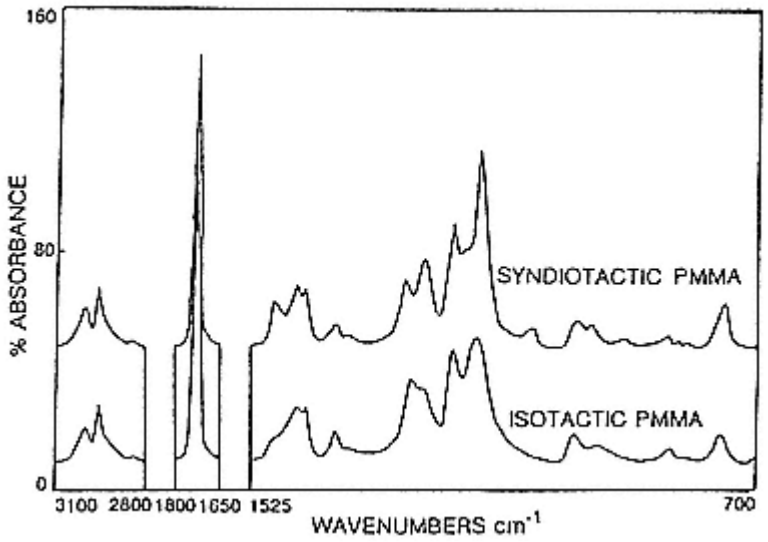

Figure 11
IR spectra of predominantly isotactic and syndiotactic PMMA.
(From Ref. 20.)

Table 3 Wavenumbers and Assignments of IR Bands for Isotactic and Syndiotactic PMMA

Isotactic	Syndiotactic	Assignment
2995		ν_a(C—H)
2948		ν_s(C—H)
1750		ν(C=O)
	1485	δ_a(α-CH)
1465	1450	δ(CH_2), δ_a(CH_3—O)
	1438	δ_s(CH_3—O)
	1388	δ_s(α-CH_3)
	1270	δ_s(α-CH_3)
1260		ν_a(C—C—O)
1252		coupled with
	1240	ν(C—O)
1190	1190	skeletal
1150	1150	
996	998	γr(CH_3—O)
950	967	γr(α-CH_3)
759	749	γ(CH_3) + skeletal

Source: Ref. 20.

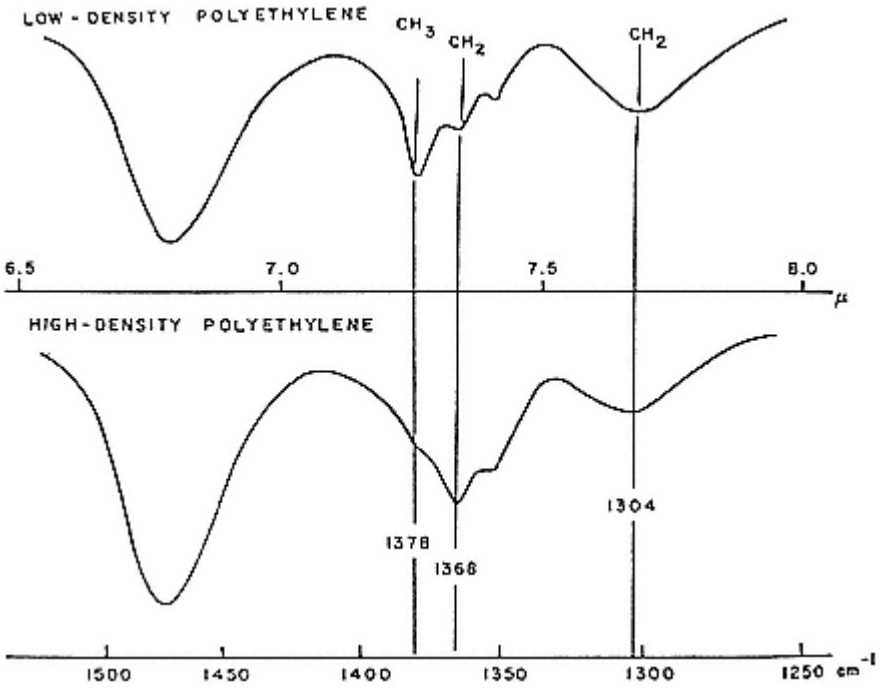

Figure 12
IR spectra of high-density (linear) and low-density (branched) PE. For determination of the degree of branching the 1378 cm^{-1} CH_3 band should be deconvoluted from its neighbors. (From Ref. 9.)

an atom having a neighbor with a spin 1/2 can see it with ±1/2; thus its chemically shifted line is split in two. As an example, consider CH_2C1-CH_3 (Figure 13). Each ^1H on the CH_2 can be parallel or antiparallel to the H_0, yielding four possible arrangements with the total spins 1, 0, 0, and - 1 as seen by the electrons on the CH_3 ^1H atoms. As a result the chemically shifted CH_3 line is split into three, with a ratio of 1:2:1. Likewise, the three ^1H on the CH_3 can have total spins of ±1/2, or ±1 1/2, yielding four CH_2 lines with an area ratio of 1:3:3:1. This spinspin interaction is over and above the chemical shift effect, but does not occur between ^1H atoms on equivalent groups (as in CH_3-CH_3) or in the same group. The amount of the shift is the same on both sets of ^1H atoms that are coupled (i.e., interaction of the CH_2 and CH_3 in Fig. 13), is independent of the field, and is affected by differences in chemical shift of the two groups. Thus one can determine the group involved by δ and the neighbors by the spin-spin coupling. With increasing field strength H_0, particularly with the advent of superconducting magnets, increasing resolution has permitted separation of spin-spin effects due not

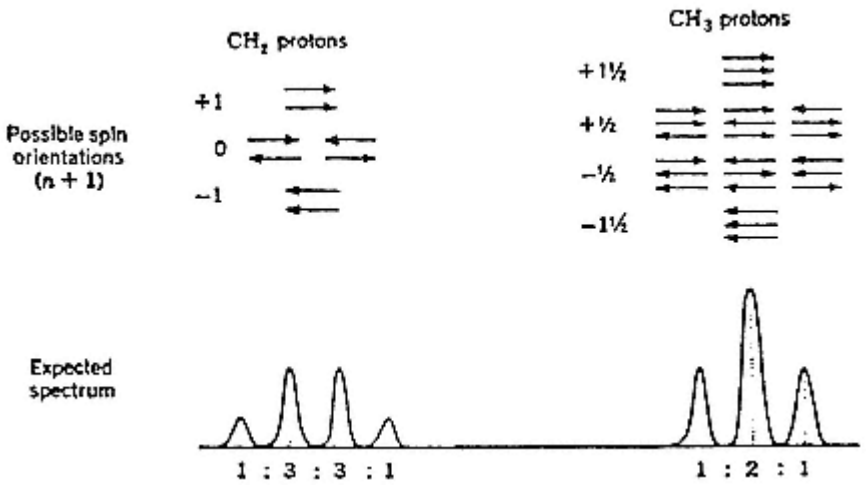

Figure 13
Spin-spin (^{1}H) coupling for ethyl chloride.
(From Ref. 2 1.)

only to neighboring groups but also to groups several backbone bonds along the chain. Examples, for predominantly *i*- and *s*- PMMA, are given in Figures 14–16 for two different values of H_0.

Consider first the CH_2 and CH_3 (backbone) groups at low H_0 (low resonance frequency) (Figure 14). In *s*-PMMA the CH_2 lines should be a singlet; the CH_3 groups are on opposite sides of the chain so that the ^{1}H atoms on the CH_2 are equivalent (the unit is racemic).

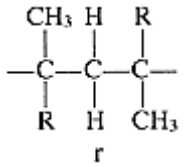 r	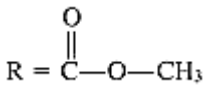	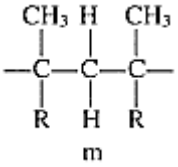 m
syndio-PMMA		*iso*-PMMA

In *i*-PMMA (*meso*) the CH_3 are on the same side of the chain, and thus the two ^{1}H on the CH_2 are not equivalent and four peaks (as in CH_2C1 - CH_3) are seen. Note that there is some fine structure to these bands and that neither form is pure. For

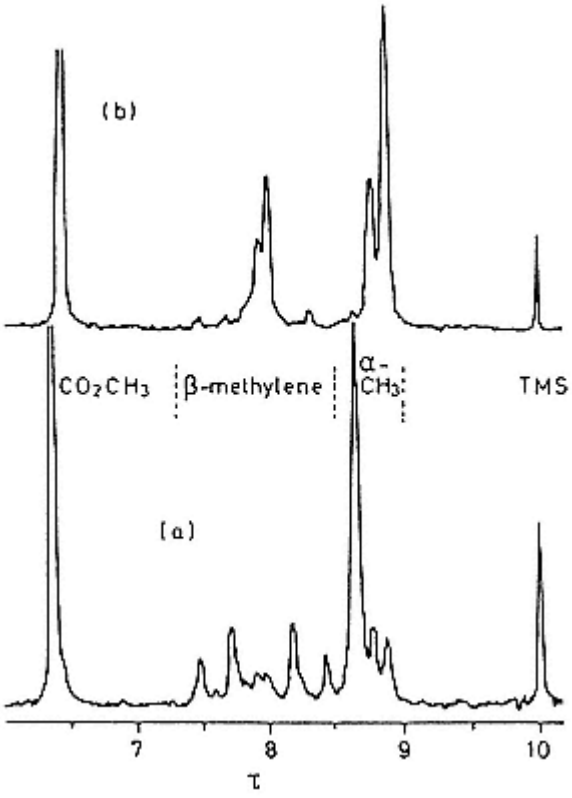

Figure 14
60-MHz NMR spectra of 15% solutions of predominantly (a) syndio and (b) iso-PMMA. The ester (β) methyl resonance is near 6.5τ the β methylene resonance is from 7.5 to 8.5τ and the α-methyl protons between 8.5 and 9.0τ
(From Ref. 22.)

the α-CH_3 group (on the backbone) the spin-spin coupling shift varies with the configuration of the neighboring CH_3, here considered as dyads.

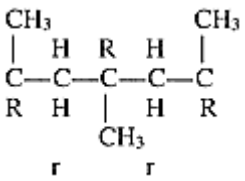	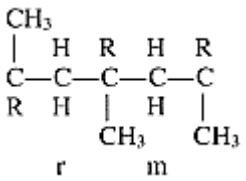
Syndio-PMMA	hetero-PMMA

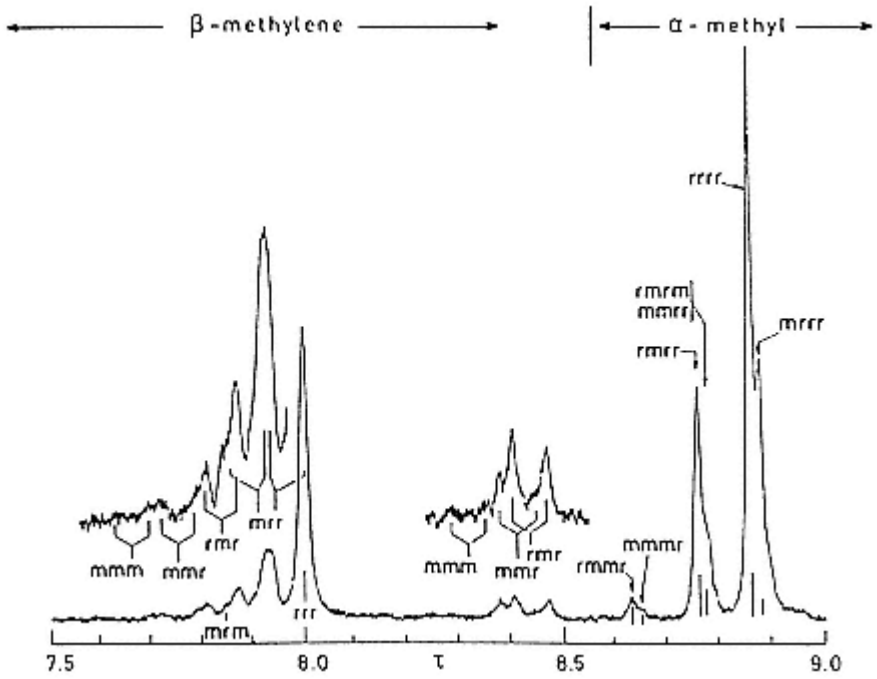

Figure 15
The β-methylene ^{1}H-220 MHz spectrum for predominantly syndiotactic PMMA in chlorobenzene at 120°C. The vertical markers for the spin-spin coupling positions for the triads (e.g., mmm) are joined by slanting lines that intersect at the positions (center) for the chemical shifts; tetrads can be resolved in the α-methyl region.
(From Ref. 23.)

and

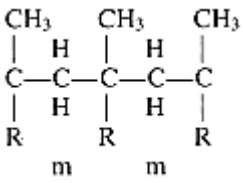

iso-PMMA

The three CH_3 peaks in Figure 14 are due to rr (*syndio*, at the highest field), rm (*hetero* or atactic), and mm (*iso*, at the lowest field) dyads. From the areas under the peaks the relative amount of the various types of dyads can be determined.

Figures 15 and 16 show the corresponding "high-resolution" (220 MHz, with current NMR machines operating at as high as 360 MHz) spectra for the same

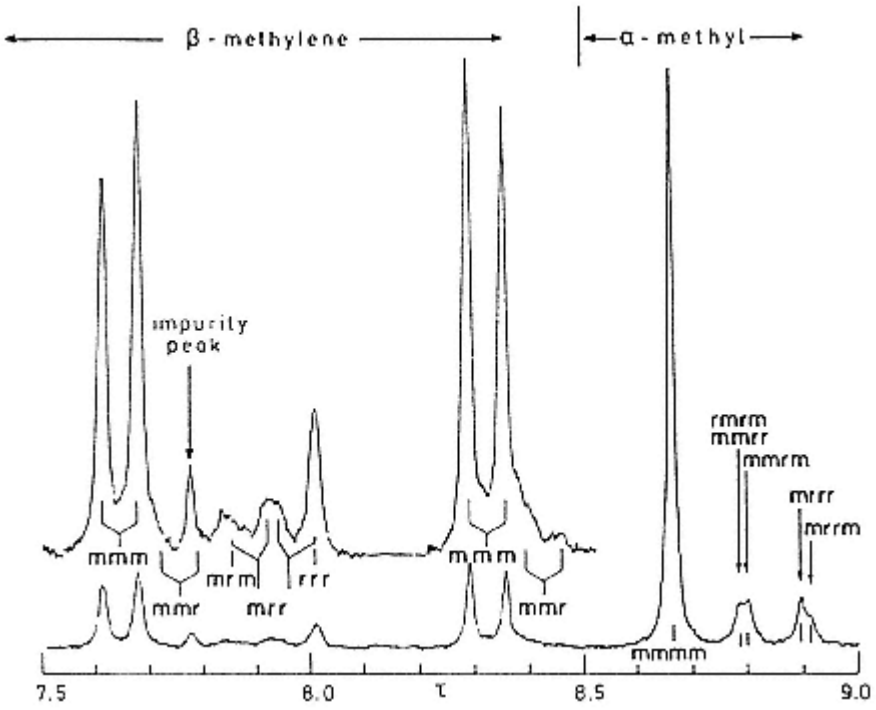

Figure 16
The ^{1}H 220 MHz spectrum for predominantly isotactic PMMA, as in Figure 15. (From Ref. 23).

types of samples. In both figures, the relative numbers of various types of triads can be determined from the CH_2 chemical shift region, while in the α-CH_3 region tetrads are identified. Similar techniques can be applied to isomerism, copolymer sequence, and so forth. The last example (Figure 17) shows the high-resolution scans used for determination of branch length in low-density PE.

Figure 18 shows the results of applying the various techniques utilized for producing narrow-line NMR spectra from solid samples; in this case ^{13}C spectra [25]. In (a), only scaler decoupling is applied, with no useful spectrum obtained. With dipolar decoupling (DD) and cross-polarization (CP), as in (b), broad resonances are obtained. With magic-angle spinning (MAS) and dipolar decoupling (c) the lines are narrowed but with considerable noise in the spectrum. In (d), the "grand" experiment (MAS + DD + CP), the various individual ^{13}C atoms can be resolved (not ^{1}H as in Figs. 14–16), but clearly tacticity could not be characterized.

Various other techniques, already discussed, can also be used for configuration characterization. In ESCA, for instance, the binding energies of the elec-

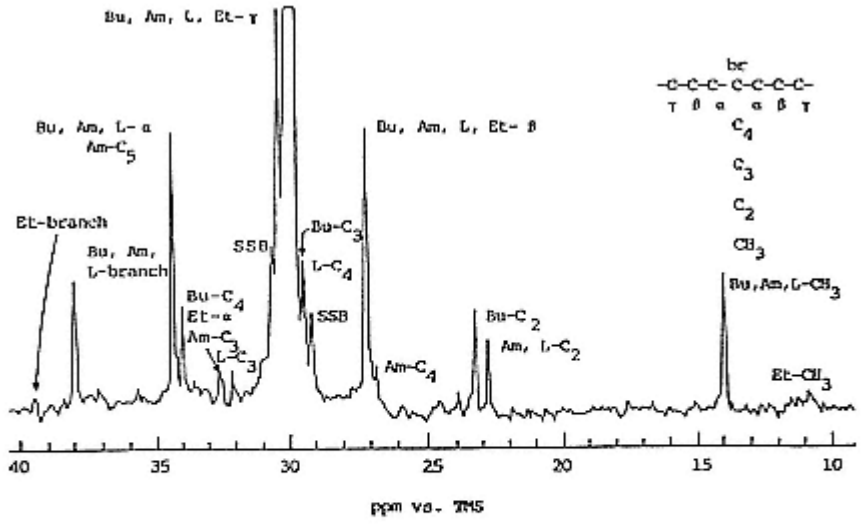

Branch Length	Methine	α	β	1	2	3	4	5	6
1	33.3	37.6	27.5	20.0					
2	39.7	34.1	27.3	11.2	26.7				
3	37.8	34.4	27.3	14.6	20.3	36.8			
4	38.2	34.6	27.3	14.1	23.4	–	34.2		
5	38.2	34.6	27.3	14.1	22.8	32.8	26.9	34.6	
6	38.2	34.6	27.3	14.1	22.8	32.2	30.4	27.3	34.6

Figure 17

^{13}C FT-NMR spectrum at 25.2 MHz for a low-density PE obtained in trichlorobenzene at 110°C with 9500 scans. The structure at upper right illustrates the C positions; the branch carbons are numbered from the methyl (1) end toward the methane C branch point. The table below indicates the corresponding chemical shifts. Branches longer than three carbons yield identical spectra. Terminology in the figure indicates the length of the branch (Am, amyl, C_5; Bu, butyl, C_4; Et, ethyl, C_2; L, long C_6 and longer), position of branches on the branch (e.g., Bu-C_2, butyl branch on C_2 of primary branch), and SSB, spinning side band (see texts, e.g., Ref. 8, for discussion). All values given in parts per million (±0.1) downfield from TMS. The solvent was 1,2,4-trichlorobenzene, and the temperature was 125°C.
(From Reft 24.)

trons emitted depend not only on the atom involved and its closely associated (bonded) atoms, but also on their neighbors. An example is shown in Figure 19 for polyethylene-polytetrafluoroethylene (PE-PTFE) copolymers for which it is claimed [26] that pentad sequences can be distinguished. Likewise, UV-visible spectroscopy can, on occasion, be used, with the absorption frequency again being dependent on neighboring groups.

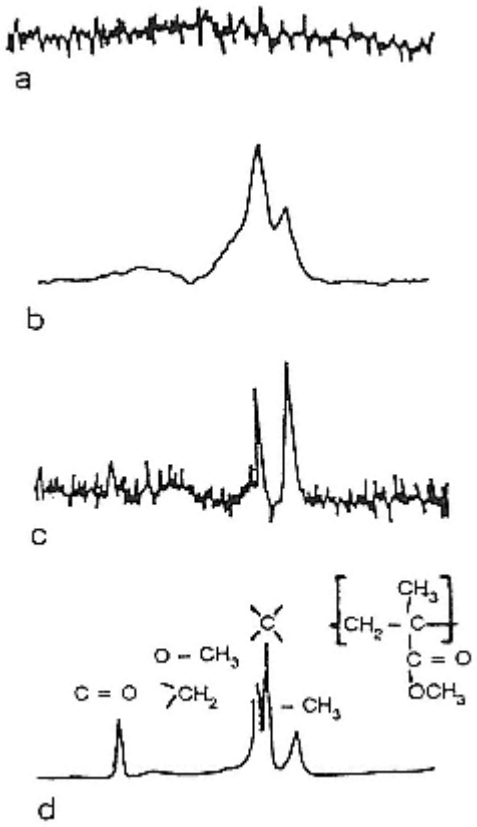

Figure 18
C^{13} solid state NMR spectra of PMMA:
(a) scaler decoupling only; (b) DD+CP;
(c) MAS+DD; (d) MAS+DD+CP.
(From Ref. 25.)

C—
Molecular Weight

Measurements based on colligative properties, dependent on the number of molecules in a given weight of sample (i.e.,M_n the number average molecular weight), include boiling-point elevation, freezing-point depression, osmotic pressure (the most sensitive), and vapor-phase osmometry [27]. For $\bar{M}_w$ light scattering has long been used, with low-angle laser light scattering being a modification reducing the effects of dust particles and the need for angle extrapolation [27]. In general these methods have been replaced, since the 1960s, by GPC. This method (see, e.g., Ref. 28) permits determination, with suitable calibration, of $\bar{M}_n$, $\bar{M}_w$, $\bar{M}_z$, in fact the full molecular weight distribution. Since the method effectively measures the spatial size or hydrodynamic volume distribution of the molecules in a solvent, it is af-

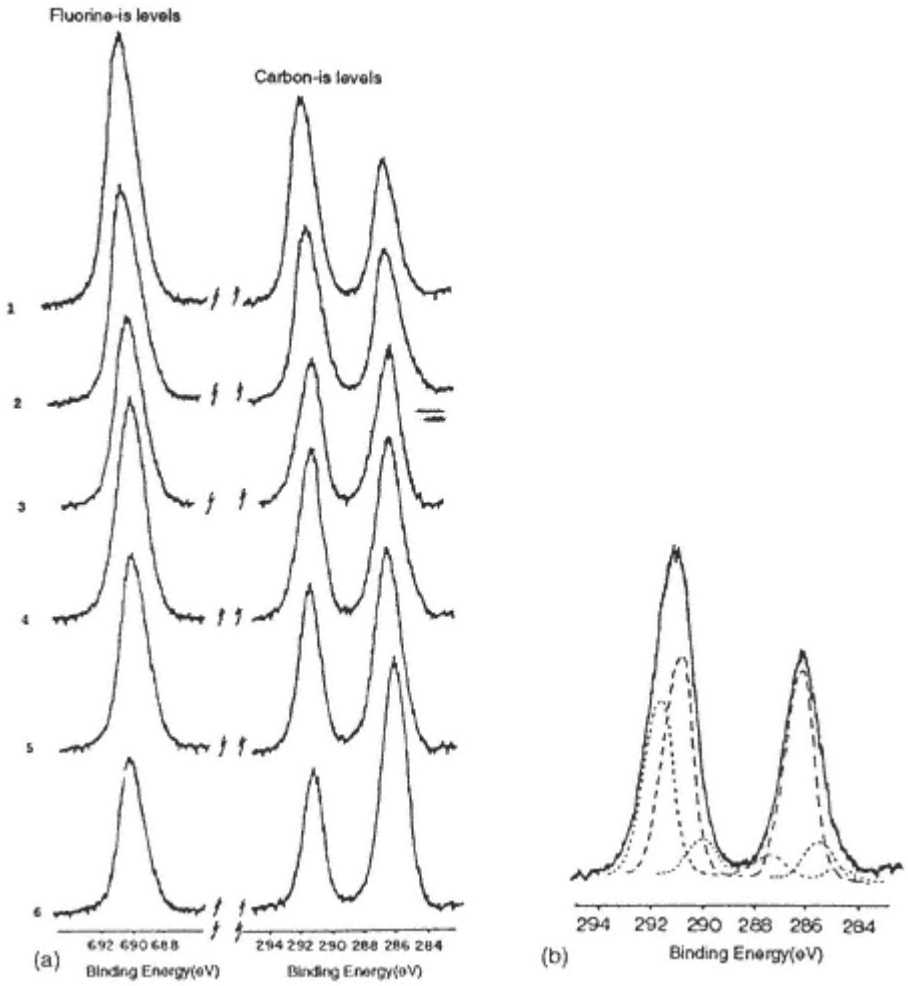

Figure 19

F_{1s} and C_{1s} ESCA levels for a series of copolymers of ethylene and tetrafluo-rocthylene (a) with the deconvoluted C_{1s} peaks for samples 1 (~ 62 mol % C_2F_4) in (b).
(From Ref. 26a.)

fected by branching, copolymer sequence, and composition as they affect chain stiffness and other properties. It also suffers from the cost of the equipment required and the lack of suitable (safe) solvents for some polymers.

Chromatography processes, in general, involve transfer of solute between two phases, one stationary and the other moving. In GPC both phases are liquid (and the same, the solvent), the stationary phase being the liquid filling the pores

in microporous gel particles packed in a column through which the solvent is flowing. As a "plug" of polymer solution is introduced into the solvent stream, a concentration gradient is set up between the solution outside the particles and the pure solvent in the particles, resulting in polymer diffusion into the pores, with the smaller molecules being more able to diffuse. As the "plug front" moves down the column, the larger molecules will be retained to a smaller degree, with the smaller molecules remaining in the pores for a longer time before diffusing out into the now less concentrated solution following the "plug end." With the concentration of the elution stream being measured (by index of refraction) a plot of concentration versus time (or elution volume) of retention is obtained that, by calibration, can be converted to a molecular weight (actually molecular coil size) distribution (Figure 20).

Using large columns, in preparative GPC, relatively sharp fractions of various molecular weight can be obtained. Prior to the development of GPC, fractionation was based on variations in solubility, either by adding a nonsolvent to a polymer solution, with the least soluble (e.g., highest molecular weight) molecules precipitating out first, or by differential elution in which a swollen polymer gel (swollen due to the presence of the solvent and needed to permit transfer of molecules from the "solid" to the liquid phase) coated on some support is eluted with liquid of gradually increasing solvent power. In both cases relatively broad distribution fractions are obtained. Improvements can be obtained by fractionally precipitating the polymer onto the column packing before elution and/or imposing a temperature gradient on the column in addition to the variations in solvent power. In the latter case, if the sample is present initially only at the top of the column it will undergo a series of precipitations and dissolution steps as it moves down the column. This is the basis of the relatively new TREF (temperature rising elution fractionization) technique used for fractionating linear low-density polyethylenes by both molecular weight and branch content [29].

Somewhat simpler, but less informative, techniques than GPC for molecular weight characterization are based on solution and melt viscosity [27]. The latter can be directly related to the melt spinnability of the polymers, and both are often used in technical data sheets for specific grades of a polymer. Solution measurements yield a "molecular weight" whose value (M_v) lies between M_n and M_w [30], while M_w can be obtained from the melt viscosity [usually it is the intrinsic viscosity, sometimes the inherent viscosity (discussed later,) or from the melt index (MI) or melt flow rate (MFR) that is given, with MI and MFR directly related to η (melt)].

In the simplest situations, solution viscosities are measured at appropriate temperature using either Ubbelohde or Ostwald-Fenske viscometers. Both permit measurement of the flow rate of the solution [time of flow for a given quantity of solution (t) or solvent (t_o)] through a calibrated capillary, with the measurements being made as a function of concentration. Extrapolation to zero concentration removes effects due to interaction of the molecules, as the viscosity due to the size of individual, noninteracting molecules is desired. Definitions of the relevant

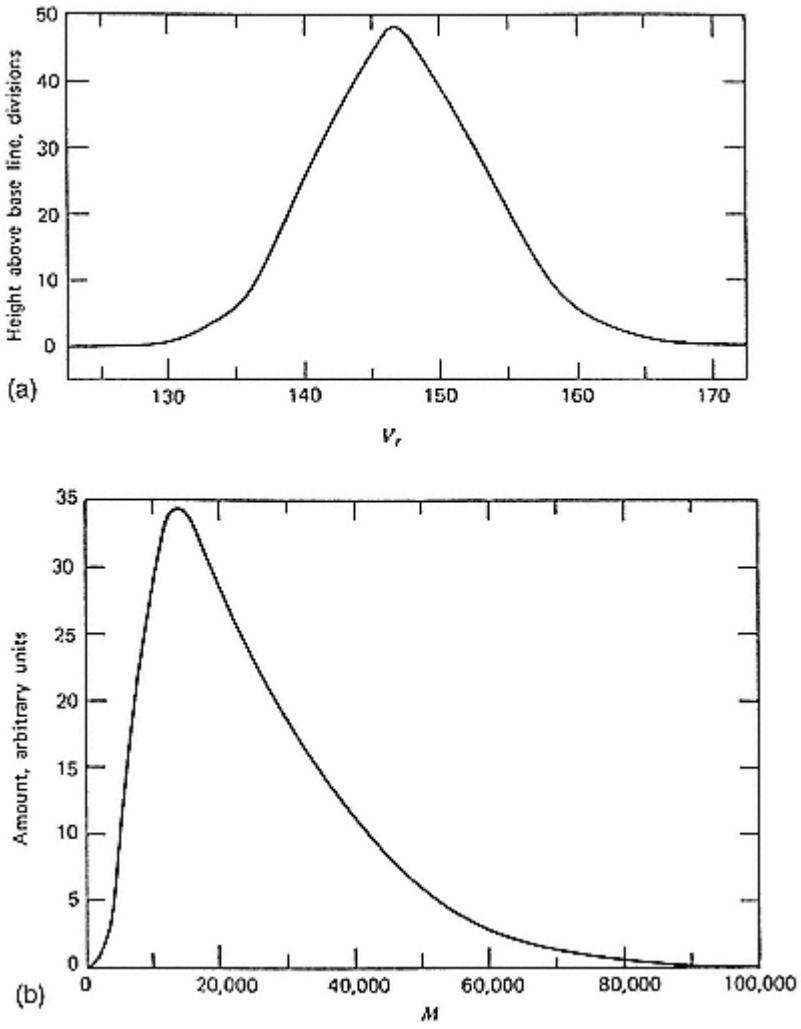

Figure 20
GPC curves for PMMA samples: (a) as measured and (b) calibrated molecular weight distribution.
(From Ref. 28a.)

terms are given in Table 4, The last relation is related to the empirically determined expressions

$$\frac{\eta_{sp}}{c} = [\eta] + k'[\eta]^2 c + \ldots \quad (4)$$

$$\frac{\ln \eta_r}{c} = [\eta] + k''[\eta^2]c + \ldots \quad (5)$$

Table 4 Definition of Solution Viscosity Terminology

Common name	IUPAC recommended name[a]	Symbol and defining equation
Relative viscosity	Viscosity ratio	$\eta_r = \eta/\eta_o \simeq t/t_o$
Specific viscosity	—	$\eta_{sp} = \eta_r - 1 = (\eta - \eta_o)/\eta_o \simeq (t - t_o)/t_o$
Reduced viscosity	Viscosity number	$\eta_{sp} = \eta_{sp}/C$
Inherent viscosity	Logarithmic viscosity number	$\eta_{inh} = (\text{In } \eta_r)/C$
Intrinsic viscosity	Limiting viscosity number	$[\eta] = (\eta_{sp}/C_{c=o} = [(\text{In } \eta_r)/C]_{c=O}$

[a]The IUPAC names are almost never used. They were proposed to eliminate the inconsistency that the common names do not have units of viscosity.
Source: Ref. 27.

where Eqs. (4) and (5) are the Huggins and Kraemer relations [31,32] and $k´ + (-k´´) = 1/2$ if additional terms are not needed, [η] is related to *M*v through the Mark-Houwink relation [33],

$$[\eta] = KM_v^a \qquad (6)$$

where *K* and *a* depend on polymer, solvent, and temperature, which are tabulated for many polymer-solvent pairs in the Polymer Handbook [4]. The solution viscosity can also be measured with various types of rheometers (capillary flow, cone and plate, couette, etc.) permitting determination of both [η], if desired, and the more concentrated η of direct concern to fiber spinning from solution (see, e.g., Ref. 34). Note that the relation between [η] and M_v applies to linear polymers since [η] is actually a measure of molecular size (hydrodynamic volume); application to branched polymers of varying degrees of branching is inappropriate.

Melt viscosity, to obtain the MI or MFR (the term used depends on the polymer), is obtained using a simple capillary viscometer, a specified (e.g., ASTM D1238) load being applied to a polymer melt at a specified temperature. The weight of polymer extruded through the specified die in, usually, 10 rain is the MI or MFR; the higher η, the lower the amount. With Newtonian flow occurring in the system, $\eta = kM$ *w$^{3.4}$, with k again being tabulated for various polymers [4]. Again various rheometers can be used to characterize η, yielding such further information as effects of variations in shear rate, normal stress effects, etc. [34,35]. These

are of particular concern in melt spinning, with high shear rates being desired for both economics and molecular orientation (see, e.g., Ref. 36).

II—
Physical Structure

The physical structure of polymers in general, and fibers in particular, occurs over a range of size scales, thus requiring a range of techniques for characterization. Of concern are structures on (1) the size scale of the individual molecular segment (e.g, their conformation), (2) the relative number of regular and random conformations and their arrangement in space (i.e., degree of crystallinity and orientation), (3) the size and shape of the crystalline and amorphous regions, including defects and disorder in the crystals, and (4) the organization and interaction of these crystals in larger structures (e.g., spherulites and fibrils for crystallizable polymers, and domains of various shapes in block copolymers and blends.) The size scales of concern overlap, extending from 1–2 nm for (1) to as large as 100 μm for (4). Techniques of primary concern include x-ray, neutron, and electron diffraction, infrared spectroscopy, and transmission and various types of scanning electron and optical microscopy, but with a wide range of other techniques being of collaborative usefulness,

A—
Molecular Conformation

Polymer conformation means the relative physical arrangement in space of the atoms of a molecular or molecular segment as affected by both intra- and intermolecular atomic interactions (e.g., covalent, hydrogen and van der Waals bonds). Although the overall dimension of the molecule, as characterized by the mean square end-to,end distance $<r^2>$, or radius of gyration, R_g, in either amorphous or crystalline regions could be considered here, we postpone its discussion to the next section. Here only the local segmental conformation is considered. In crystalline regions this is most often determined by x-ray (or electron) diffraction, that is, the determination of the shape of the molecule in the unit cell. For molecular conformation in the amorphous regions, and supplementing the diffraction studies for crystalline regions, infrared spectroscopy is the primary tool. Both of these, other than for recent developments in diffraction, rely on traditional techniques but with continued improvement in instrumentation and application of computer-based calculations and simulations.

Characterization of the unit cell of a polymer crystal requires determination of the spatial position of all of the atoms, from one or more molecular segments, each one physical repeat unit long, within the unit cell—that is, the conformation of the physical repeat unit and their relative positions. While this can be done by standard x-ray diffraction techniques, their application to polymers is made difficult by (1) the complexity (number of atoms and low symmetry) of the unit cells,

(2) general lack of availability of macroscopic single crystals permitting application of x-ray single-crystal techniques, (3) disorder of various forms in the crystalline regions that can be produced, and (4) the C, H, N, O atomic composition (low scattering power) of most polymers. See Ref. 37 for discussions of applications of standard x-ray techniques of crystal structure (lattice and unit cell) determination to organic nonpolymeric molecules; although there are numerous texts on crystal structure determinations for inorganic crystals, the problems involved in the determination of the crystal structure of organic molecular crystals are much closer to those involved in the determination of the crystal structure of polymers.

X-ray unit cell characterization of polymers generally takes advantage of two features relatively unique to macromolecular systems, the helical conformation of most polymers (synthetic and biological) in crystalline regions (Figure 21) and the ability to produce fibers in which there is an alignment of the molecular (back-bone) axes along the fiber axis [39]. The latter isolates the Bragg reflections from one of the axes of the unit cell (usually **c**) along the meridian of the diffraction pattern,* and the former somewhat simplifies the determination of the molecular conformation from that pattern. For instance, the layer line spacing corresponds to the length of the physical repeat unit; the number of layer lines and distance to the layer line with the first meridional reflection correspond to the number of chemical repeat units per physical repeat and the axial distance per chemical repeat unit. The type of helix, that is, number of turns of continuous helix per physical repeat unit, can also be determined from the form of the pattern. Although these do not determine the relative spatial positions of each atom in the repeat unit, chemical or physical, knowledge of this type is of major assistance. Furthermore, this and a knowledge of the dimensions of the lattice are sufficient to determine the density of the perfect crystal needed, discussed later. Determining the positions of the atoms is generally aided by knowledge of the chemical structure and typical bond lengths and angles, as determined from low-molecular-weight "model compound" crystal structures. It is "confirmed," in the end, by comparison of calculations of the structure factors or intensities of the various reflections based on the positions and scattering of the individual atoms in all of the physical repeat units in the unit cell (as related by the symmetry of the lattice) and the experimental intensities. Details of the determination of the helical conformation and the unit cell are discussed in several texts [39,40], with that by Vainshtein [40] particularly recommended. Examples will be drawn from the use of electron diffraction, as described later. As pointed out in Ref. 39e, drawing, as well as defects, crystal thickness, and, in particular, temperature can have a significant effect on the unit cell parameters. For example, Bhatt et al. [41] have suggested that the angle between **c** and **b** (α)

*In triclinic and some monoclinic unit cells $\mathbf{c}^*$ is not parallel to the fiber axis; see electron diffraction patterns in Fig. 37. This makes the determination more difficult.

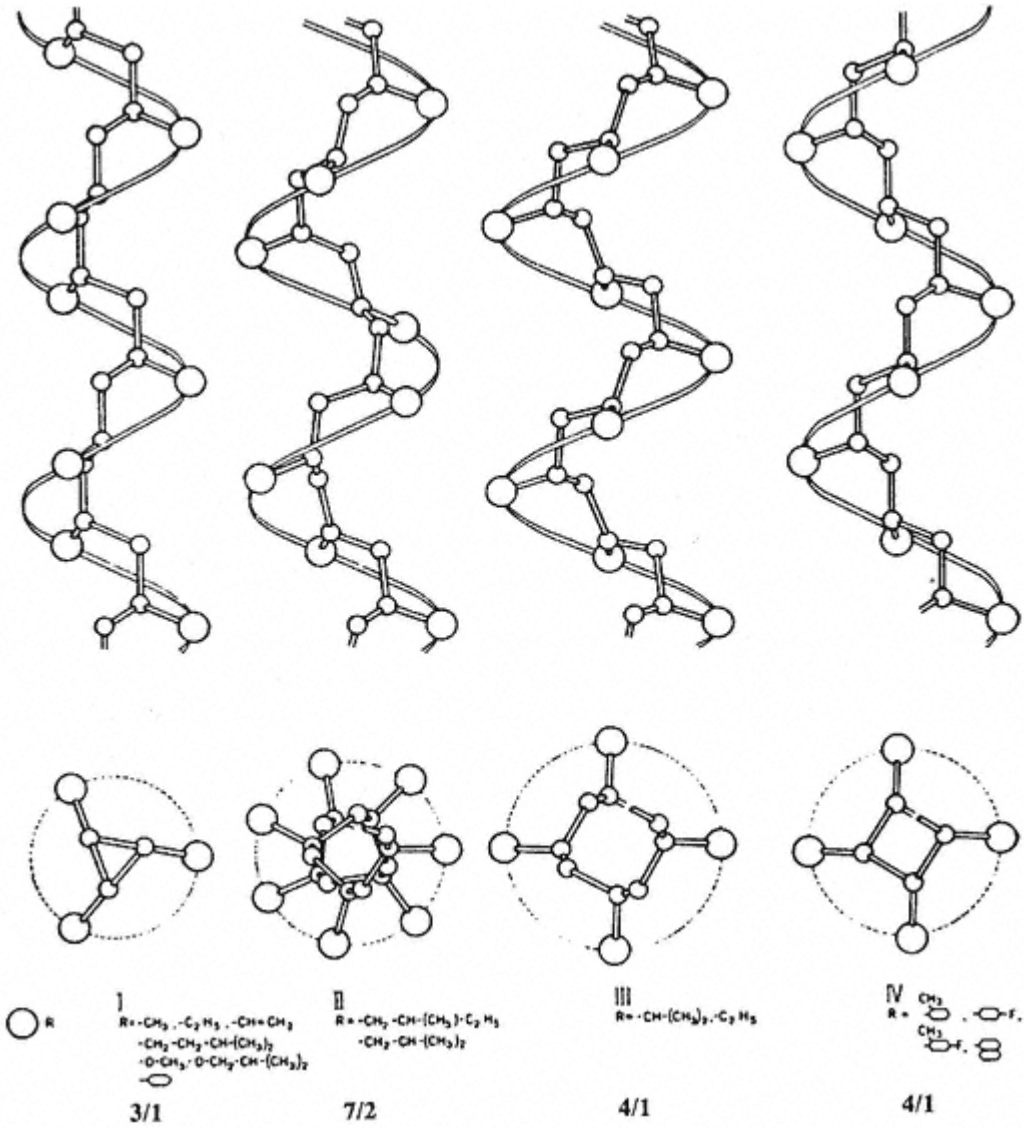

Figure 21
Representative helical conformation of isotactic polymers. The same pitch helix (different radius and starting point) can be drawn through any identical atom in the chemical repeat units (e.g., the backbone C containing the side group). The side groups, represented by R, corresponding to each helix are listed. A number of other helices are also found, such as 11/3 as well as 3/1 and 4/1 for polybutene (R = C_2H_5, 15/7 and 13/6 for PTFE, 9/5, or 28/16 for polyoxymethylene, etc.
(From Ref. 38.)

in polyethylene terephthalate (PET) increases linearly with draw ratio, based on the separation of the $\bar{5}$ peaks. The value of 98.5° usually reported corresponds to a draw ratio of 6–6.5. On the other hand, the separation may be due to the known tilt of the e axis relative to the fiber [45], varying with the amount of draw.

As indicated in Section I, infrared (and Raman) absorption spectra result from molecular vibrations that cause changes in the dipole moment (and polarizability) of the molecule; these spectra are unique to each molecule. They are used for configuration determinations but also depend on the conformation and molecular packing as they affect the intra- and intermolecular forces, respectively. For both IR and Raman, the normal mode vibrations of small atomic groups, such as CH_2 and C=O, are of concern, as affected by their local environment.

Conventional Raman spectroscopy, even though yielding equivalently useful information, has been used much less widely than IR for the study of polymers (see Refs. 8 and 42). Estimates are that it fails to produce usable spectra in more than 50% of normal samples [8], primarily due to fluorescence and self-absorption of the Raman photons. FT-Raman, with an attachment that can be added to some FTIR instruments in the near-infrared region, has improved the situation. Figure 22 is an example of the use of Raman for characterizing changes in the conformation of polyethylene terephthalate as it is annealed [43]; complementary studies by DSC and IR are described in Ref. 44 and Figs. 23 and 24.

It is well known that amorphous PET will crystallize when heated above T_g; at the heating rates used in a DSC it crystallizes at temperatures near 110°C. Figure 22(A) shows the Raman spectra in the region 750–1050 cm^{-1}; the peaks at 998 and 886 cm^{-1}, respectively, are assigned to trans ($O\text{-}CH_2$ stretch) and gauche conformations of the ethylene glycol segments. The 795 cm^{-1} band, shown to be independent of thermal treatment, was used as an internal thickness band. In IR the corresponding bands used were 973 ($O\text{-}CH_2$ stretch, trans), 898 (CH_2 rock, gauche) and 793 cm^{-1} (internal thickness). From the ratio of intensities of these bands, that is, $I(998)/I(795)$ and $I(886)/I(795)$, the fraction of trans and gauche conformations of the flexible $\text{-}O\text{-}CH_2\text{-}CH_2\text{-}O$ segment (shown to be trans in the CryStal by x-ray diffraction [45] can be obtained (Figure 22(B)). In agreement with DSC results (Figure 23(A)); crystallization (conversion of gauche to trans conformers) begins above T_g—for the annealing conditions used here, at ~90°C. Note that the initial bulk sample, an injection molded plate 3 mm thick, with the back-scattered Raman spectra being obtained, has a degree of crystallinity as determined by DSC of ~30% (Figure 23(B)). With a portion of the trans conformation known to occur in the amorphous regions, there is a clear discrepancy with the 25% trans conformer obtained by Raman. The "discrepancy," indicative of the power of the technique, is attributed to a skin-core morphology for the sample. The skin, being more rapidly quenched, is initially more amorphous than the core, with DSC giving a bulk crystallinity value and Raman sampling only, in this case, less than the 500 μm thickness observed by optical microscopy for the skin. Determination of the trans conformer content in a glassy amorphous sample (~15%) permitted separa-

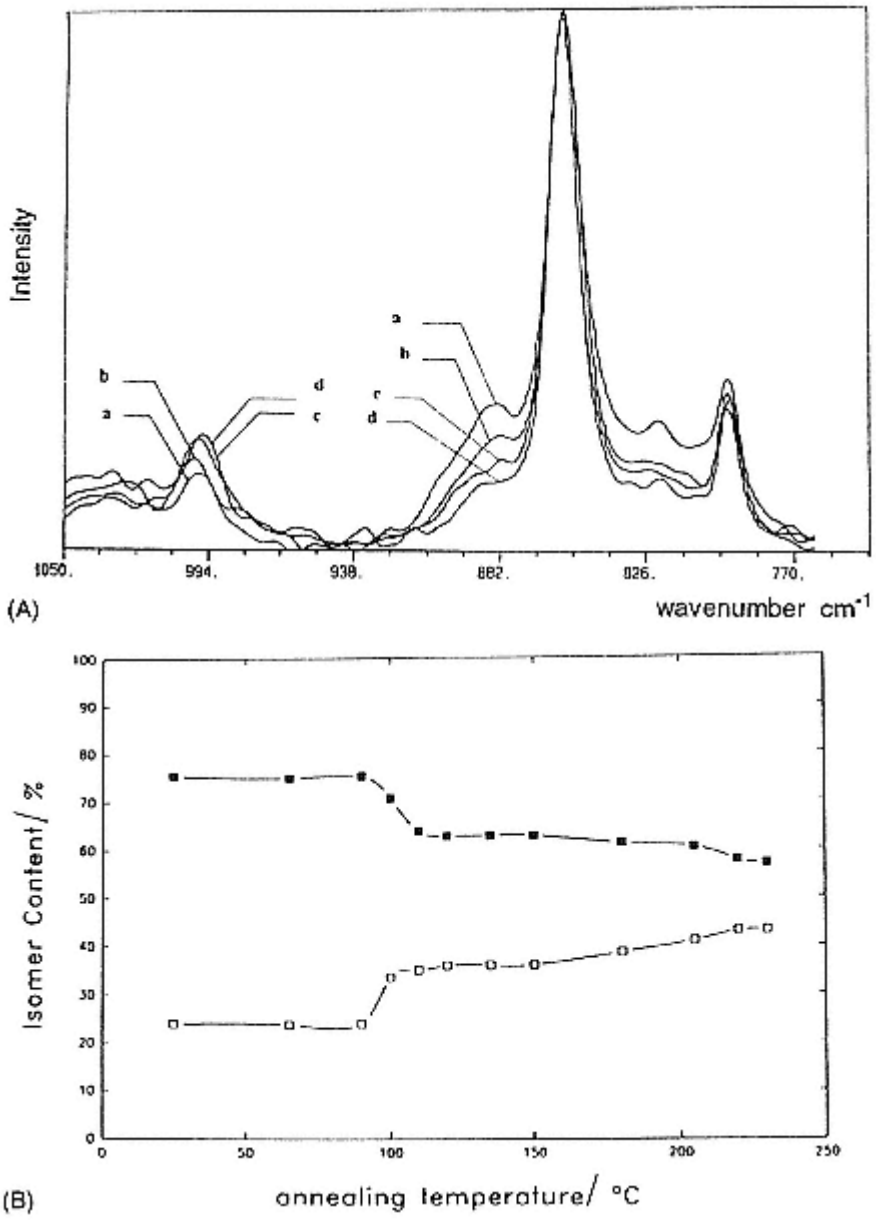

Figure 22
(A) FT-Raman spectra of PET: a) as molded and as annealed at b) 110°C, c) 150°C and d) 205°C for 1 hour. (B) Plot of distribution of trans (□) and gauche (■) conformers in PET based on Figure 22(A).
(From Ref. 43.)

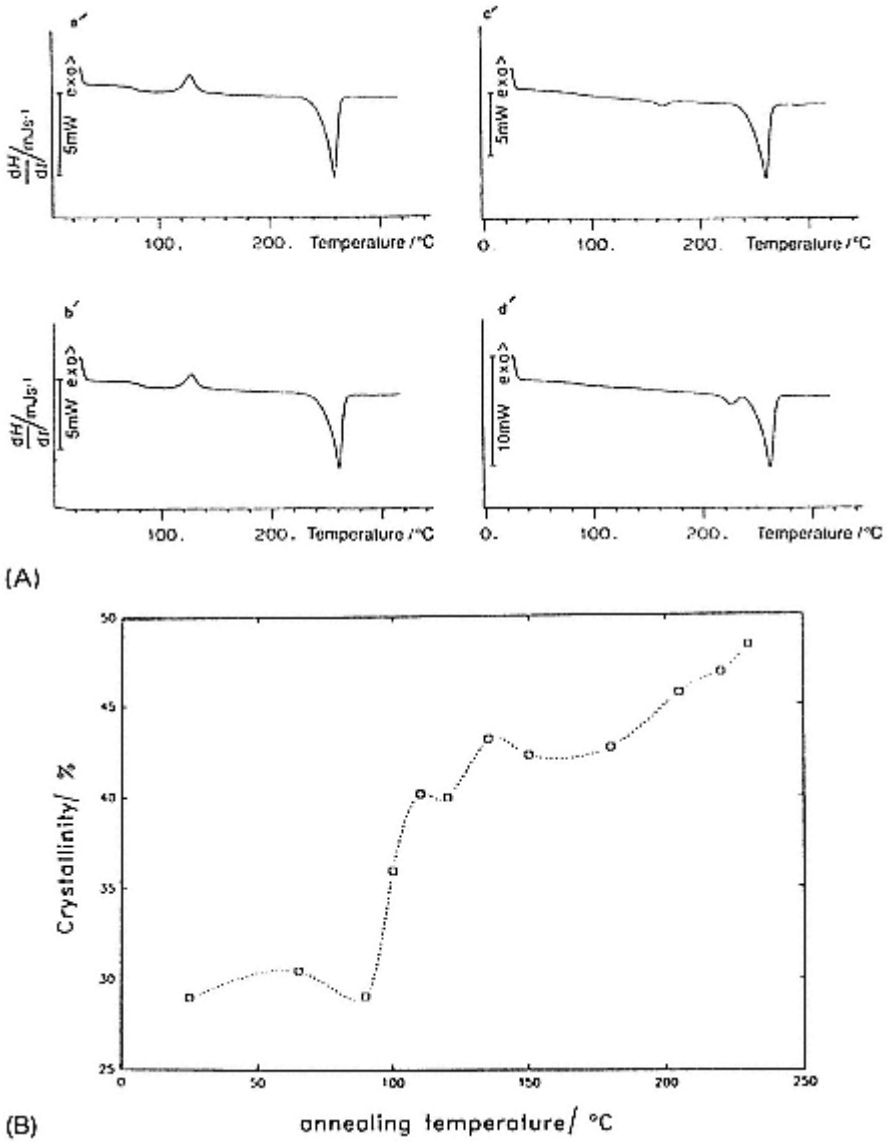

Figure 23
(A) DSC scans of PET as quenched (a´) and annealed at (b´) 90°C, (c´) 150° and (d´) 205°C for 1 hr. The exothermic peak in (a´) and (b´) results from crystallization during heating. (B) Plot of the DSC-determined crystallinity of an injection molded PET sample as a function of annealing temperature (1 hr). The crystallinity was calculated based on the ΔH_f measured relative to a 28.1 cal/g ΔH_f for 100% crystalline PET. (From Ref. 43.)

tion of the distribution of gauche (amorphous), trans (amorphous), and trans (crystalline) conformer as a function of annealing temperature (Figure 24(A)), with Figure 24(B) showing the (excellent) correlation between the DSC-determined skin-layer crystallinity and the crystalline trans content determined by Raman spectroscopy. Figure 25 show similar correlations obtained by IR, using the 973, 898 and 793 cm^{-1} bands (see also Figure 50).

As shown in Figure 22(B), in addition to the step change at about 100°C, there is a change in slope at ~140°C. Similar step changes and changes in slope are seen, for instance, for the width of the 858 cm^{-1} [complex mode consisting of ring C-C and C(O)-O stretching] and 1725 (C=O stretch) cm^{-1} bands (see original paper [43]). The step change is again related to conformation changes accompanying the crystallization above T_g, while the change in slope at ~140°C is attributed to the development of sufficient segmental mobility to permit further segmental rearrangement and an increase in crystallinity. We suggest the initial crystallization constrains the mobility of the remaining amorphous segments, with 140°C corresponding, in terms of Boyer's double-T_g model [46], to the higher T_g.

As an additional example of the application, in this case of IR, to details of the conformation of PET, we take an even earlier report by Koenig and Harmon [47]. Using solution-crystallized and annealed, molded as well as etched (fold surface removed) samples, in comparison with glassy and molten amorphous samples as extremes, they attributed the 988 cm^{-1} (and 1380 cm^{-1}) band to the (tight) gauche conformation of an adjacent reentry fold. With the 973 cm^{-1} band as a measure of the degree of crystallinity (trans content, discussed earlier) and the 793 cm^{-1} band as an internal thickness band, they could then follow the changes in numbers of tight folds and crystallinity with thermal treatment in both molded and drawn film (fiber-like) samples. As shown in Figures 25(A—D), the number of tight folds is zero in the melt and quenched amorphous samples, near zero in as-drawn films, but increases with annealing in both types of samples. As noted by the authors, the absence of the 988 cm^{-1} band does not necessarily indicate the absence of folds; its presence is interpreted as being due to the particular sequence of gauche conformations in a tight, adjacent reentry fold.

The preceding experimental methods have been supplemented (and in some views replaced) in recent years by semiempirical force-field calculations and molecular orbital calculations. Commercially developed programs (e.g., Ref. 48) permit determination of minimum energy conformations both for single molecules and as they are packed in a crystal (Figure 26). The Cerius^2 program, from Molecular Simulations, Inc., is of particular interest in that it also, based on the crystal packing module, permits display of the corresponding powder, fiber, and electron diffraction patterns for direct comparison with experimental results (Figure 27; see later discussions for ED pattern simulation and comparison). However, even within the same program, the use of different force fields for the description of inter- and intramolecular interactions yields different results.

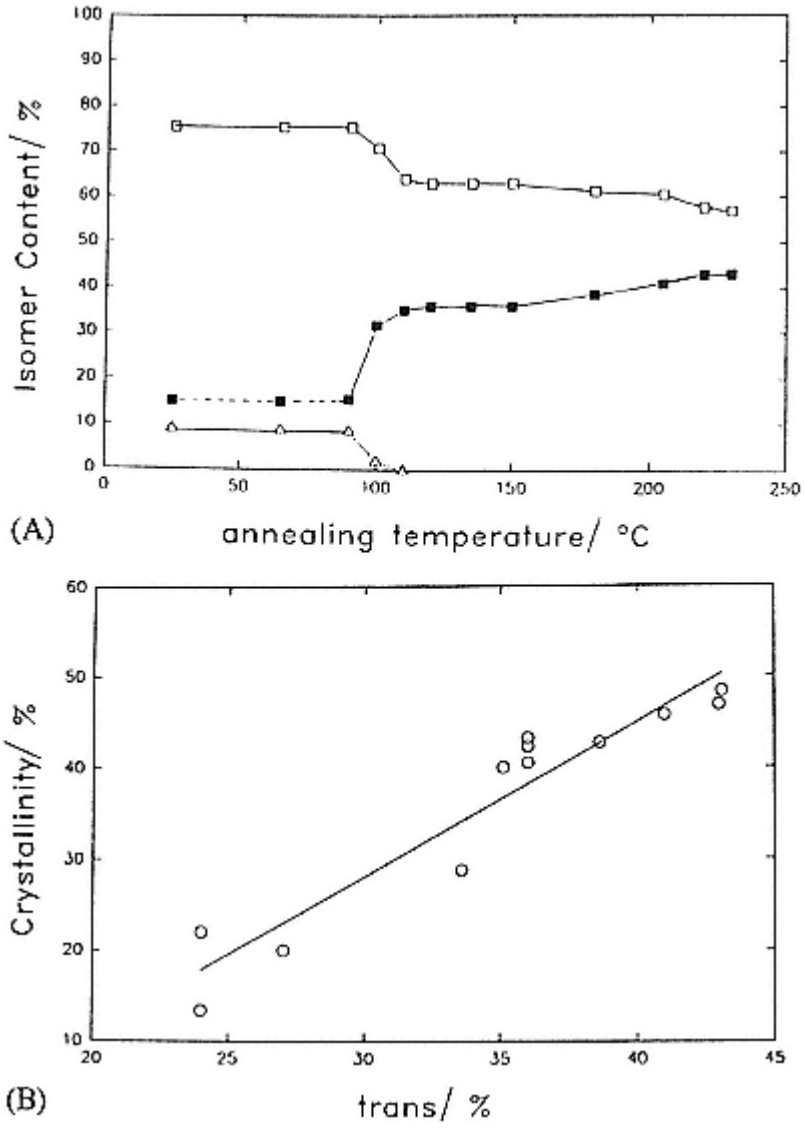

Figure 24
(A) Corrected distribution of trans and gauche conformers in injection molded PET: (□) gauche; (■) crystalline trans; (Δ) amorphous trans. (B) Correlation of crystallinity in the skin layer as determined by DSC and the Raman-determined crystalline trans fraction.
(From Ref. 43.)

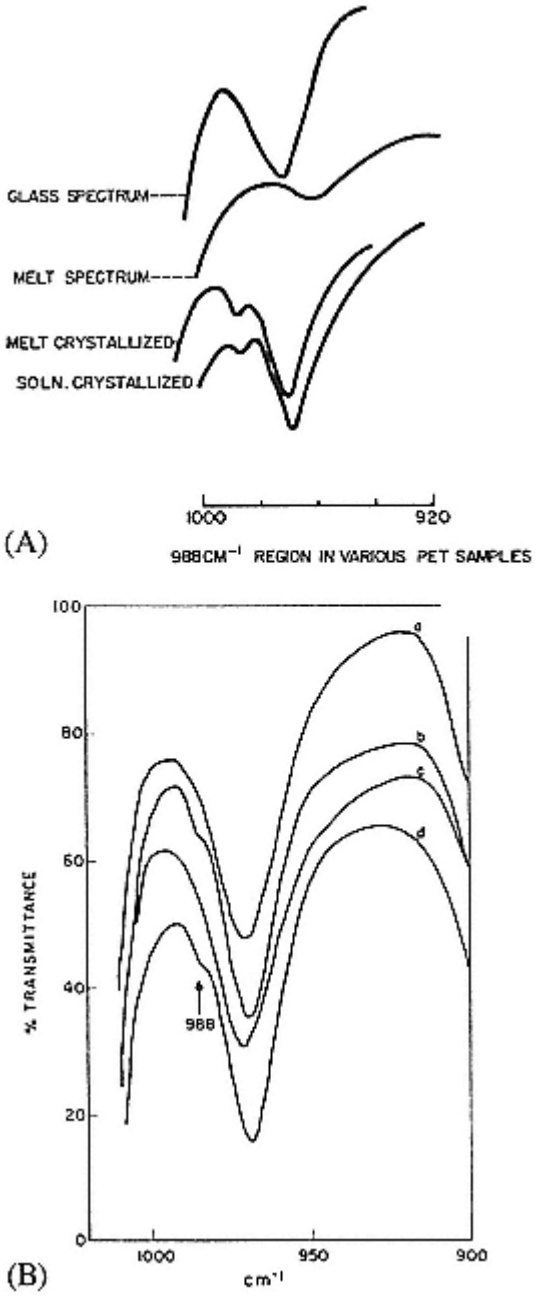

Figure 25
(A) 988 cm^{-1} IR band in various PET samples. (B) IR spectra (900–1000cm^{-1}) of an amorphous PET sample (a´) stretched 430%, (b´) annealed taut at

Sample	$\frac{A_{973}\ (cryst.)}{A_{795}}$	$\frac{A_{988}\ (fold)}{A_{795}}$	$\frac{A_{988}}{A_{973}}$
Melt-cry stallized	2.94	0.44	0.15
PET high-IV (0.89) melt-crystallized	2.85	0.52	0.18
Crystallized from 2-(2-butoxy ethoxy) ethanol (slow cool)	2.75	0.17	0.06
PET high-IV (1.60) melt-crystallized	2.65	0.41	0.16
Crystallized from 2-(2-butoxy ethoxy) ethanol (190°C)	2.42	0.25	0.10
Crystallized from dimethyl phthalate	2.04	0.24	0.12
PET high-IV (0.89) as polymerized	1.66	0.10	0.06
(C) PET high-IV (1.60) as polymerized	1.64	0.16	0.09

Sample	$\frac{A_{973}\ (cryst.)}{A_{795}}$	$\frac{A_{988}\ (fold)}{A_{795}}$	$\frac{A_{988}}{A_{973}}$
(a) Amorphous film	0.33	0	0
(b) Sample (a) stretched 430%	1.28	0	0
(c) Sample (b) annealed at 140°C, 1/2 hr	1.49	0.08	0.05
(d) Sample (c) stretched 50%	1.76	0	0
(e) Sample (d) annealed at 140°C, 1/2 hr (D)	1.89	0.10	0.05

Figure 25
(continued) 140°C, 30 min (c´) part (b´) restretched 50% and (d´) reannealed at 140°C, 30 min. (C) Table of ratios of absorbances of the 973 cm^{-1} (trans), and 988 cm^{-1} (fold) bands to the internal thickness 795 cm^{-1} band for the samples in Figure 25(A). Note the ratios needed to be corrected by the molar extinction coefficients in order to determine the "actual" degree of crystallinity and numbers of folds.
(D) Absorbance ratios for the drawn samples in Figure 25-B.
(From Reft 47).

Although, as indicated at the beginning of this section, x-ray diffraction characterization of polymer

conformation (in crystalline regions) is aided by the use of fibers, it still requires development of a model from which calculated intensifies of the reciprocal lattice "points" are compared with those measured. The x-ray fiber pattern corresponds to the rotationally averaged projection of the reciprocal lattice, with rotation about **c** (rather than $\mathbf{c}^*$, which complicates determination of crystal structures of triclinic and monoclinic unit cells). We have contended for some time [50] that if appropriate samples are available, electron diffraction rather than x-ray diffraction is a better (simpler to interpret) method of determining crys-

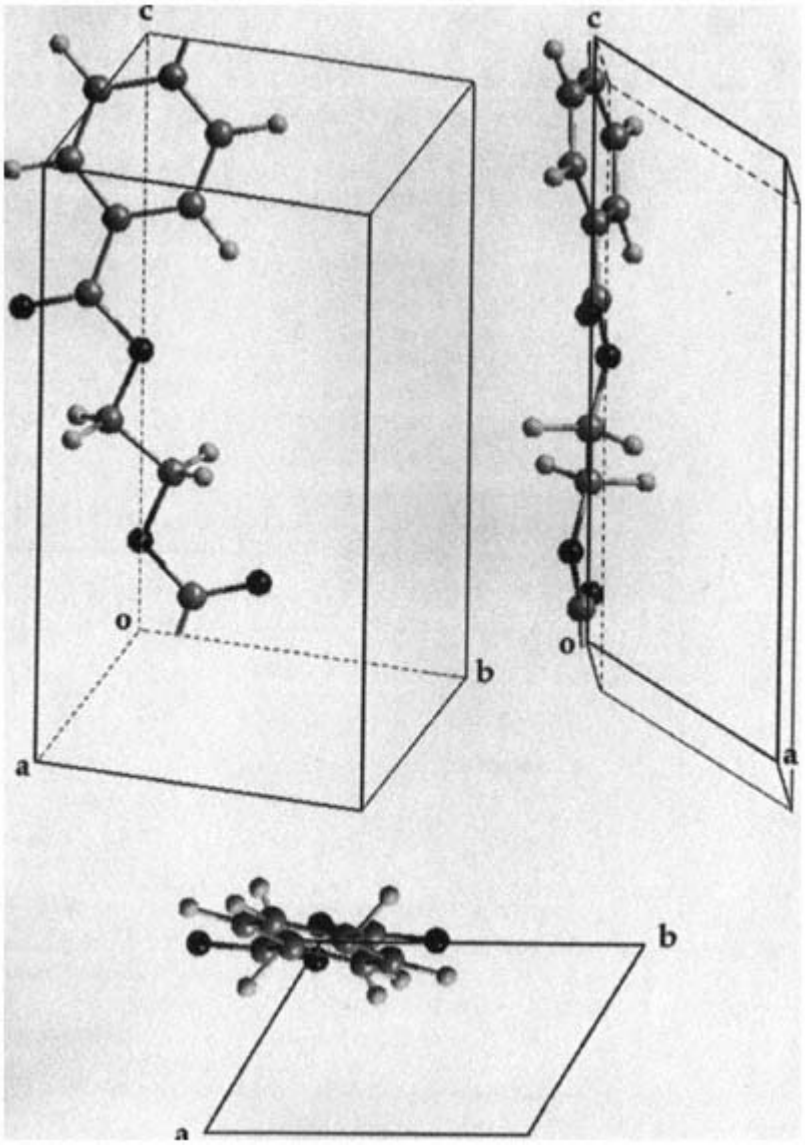

Figure 26
Simulation of the conformation of a single PET chain (one chemical repeat unit shown) and their packing in the crystal lattice. Additional segments are at each comer of the cell. The simulation was done using the Cerius^2 program [48a] (Universal force field) and the unit cell parameters described in Ref. 45.
(From Ref. 49.)

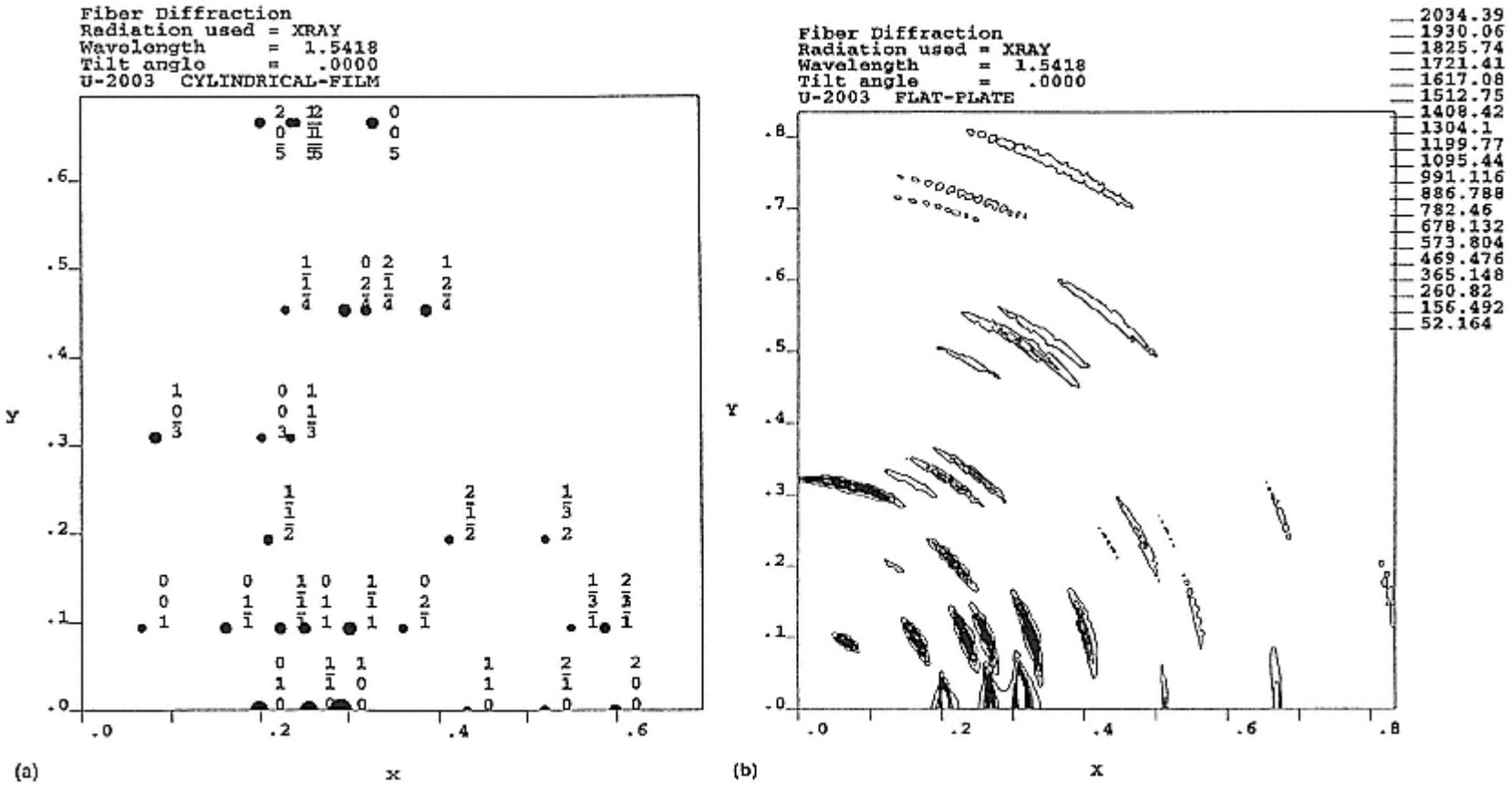

Figure 27
Simulated fiber (a,b) and powder (c) x-ray diffraction patterns for PET based on the crystal packing shown in Figure 26. 105 at 42.5°C in the powder pattern is normally used for measuring the orientation of PET fibers. It is not seen in the "spot" fiber pattern (a) for which perfect orientation was assumed. In (b) a 5°C distribution (Gaussian, value at half maximum) was assumed for the simulation. (From Ref. 49.)

tal structure either by itself or at least in conjunction with x-ray diffraction. The potential of using ED has been greatly enhanced recently by Dorset's development [51] of *ab initio* direct phasing of the ED patterns permitting direct calculation of electron density projections. For general discussions of

the application of electron diffraction to crystal structure determination see Ref. 52, with a number of recent papers on its application to synthetic and natural macromolecules in Ref. 53.

The advantage of electron diffraction is that, if appropriate samples are available, single-crystal or, if necessary, fiber diffraction patterns can be obtained. The single-crystal patterns are displays of the intensity distribution on a single plane

(or zone, due to the flatness of the sphere of reflection resulting from the small value of λ) of the reciprocal lattice from which, using Dorset's technique, the electron density of the unit cell projected on the corresponding real space plane can be calculated. On the other hand, with the simulation techniques the calculated intensities can be compared directly with the measured ones, with the results of small changes in conformation, packing, and various types of disorder being "immediately" visualized.

The problems in utilizing electron diffraction primarily are due to the need for "appropriate" samples:

1. The samples are preferably single crystals with lateral dimensions on the order of at least 1 μm (to yield sufficient intensity within the lifetime of the crystal as determined by beam damage and to permit isolation by selected area apertures).

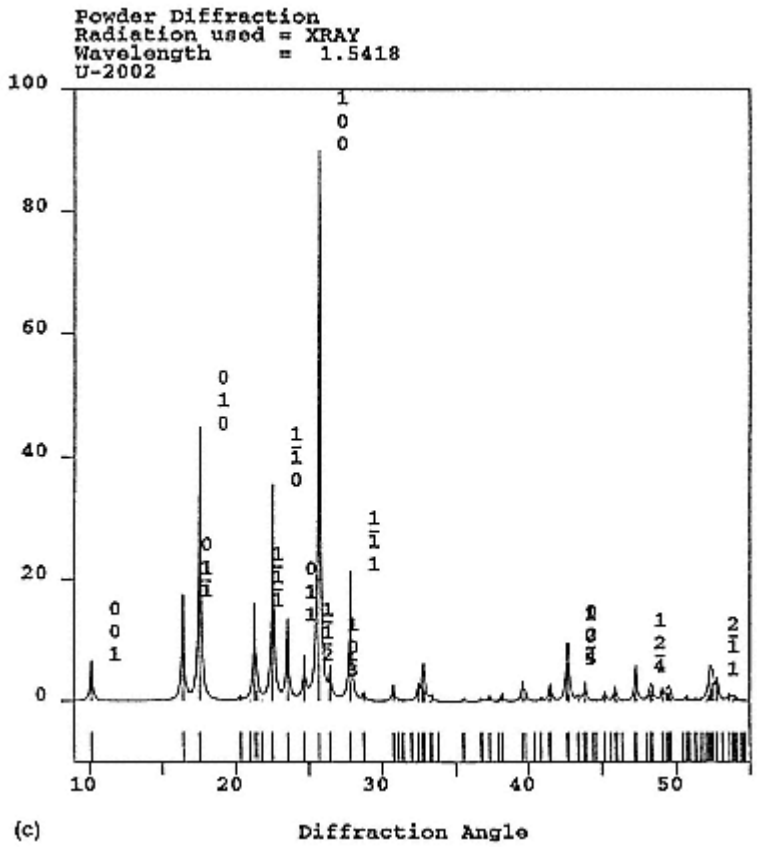

Figure 27
(continued)

2. They should be on the order, preferably, of 100 Å thickness to reduce or eliminate dynamic (double) diffraction. The scattering power for electrons is sufficiently high that diffracted beams in thicker samples are rediffracted one or more times, resulting in "incorrect" intensity distributions.

3. If single crystals are not available, fibers (usually sheared films) can be used. These generally are annealed to develop as high crystallinity as possible, but still yield only rotationally averaged patterns. They still have advantages over x-ray patterns in that the flatness of the sphere of reflection permits obtaining 001 reflections (meridian), as well as the averaged hk0 and hkl (equator and quadrant) reflections, without tilting the sample.

4. Assurance that the samples used are representative (same crystal structure as the bulk samples [fibers, films, or molded objects] of interest). This can be done by comparison with x-ray results. As shown later, the single-crystal

samples are often more perfect and may have different packing. For instance, parallel chain packing in crystals grown by simultaneous polymerization-crystallization, antiparallel chain packing in folded chain crystals, and statistically random chain direction in drawn fibers and films are to be expected, with different chain conformations in all three.

Sample preparation, as suggested earlier, is probably the critical factor in obtaining ED patterns, with it being in many cases more an art than a science. In the following we consider the methods, representative results, and potential difficulties.

1. *Crystallization from Dilute Solution.* As is well known (and discussed later), almost all polymers that are crystallizable can be crystallized from dilute (<0.1%) solution as lameliar, ~100Å thick, single crystals composed of folded (and therefore antiparallel or at least statistically random chain packing) molecules. This is independent of ongoing debates over the adjacency and regularity of the folding. These crystals yield hk0 ED patterns (Fig. 28), which are, in a sense, images of the hk0 plane of the reciprocal lattice permitting calculation of the electron density of the crystal projected on that plane in real space (Fig. 29). Interpretation of the electron density map, particularly if only the single hk0 map is available, in terms of the chain conformation is not straightforward; as in the case of interpretation of x-ray diffraction, it is usually compared with predictions from modeling.

2. *Epitaxial Crystallization*. For a reasonable number of polymers, epitaxial crystallization from dilute solution (see, in particular, papers by Wittman, Lotz and co-workers [56]) on various substrates (e.g., alkali halide or low-molecular-weight organic single crystals, or oriented polymer films) results in lamellar crystals in which the molecular axes are parallel to particular directions on the substrate surface, with, in many cases, one of the hk0 planes parallel to the surface. The lamellae grow out from the surface (Figure 30). Resulting ED patterns, with a greater potential for double diffraction due to the sample thickness parallel to the beam, permit determination of c axis spacings and may yield single, crystal patterns (or single-crystal patterns "crossed" at angles determined by the substrate lattice) of an hk0 zone. If so, electron density maps in a projection direction normal to the chain axis rather than parallel (as in crystallization from dilute solution) can be obtained.

3. *"Practical" Samples*. Much more difficult is the obtaining of appropriate (thin) samples from objects of practical interest, that is, bulk melt crystallized samples, fibers, films, etc. In a few cases Crystallization of thin films (i.e.,<1000 Å) from the melt on, for example, glass slides has yielded single crystals, or spherulitic structures in which the lamellae in a large enough area yield a common lattice orientation, suitable for ED [58,59]. Dynamic diffraction is of more concern than for crystallization from dilute solution. In other cases slow crystallization (i.e., at low supercooling) of normal-thickness samples

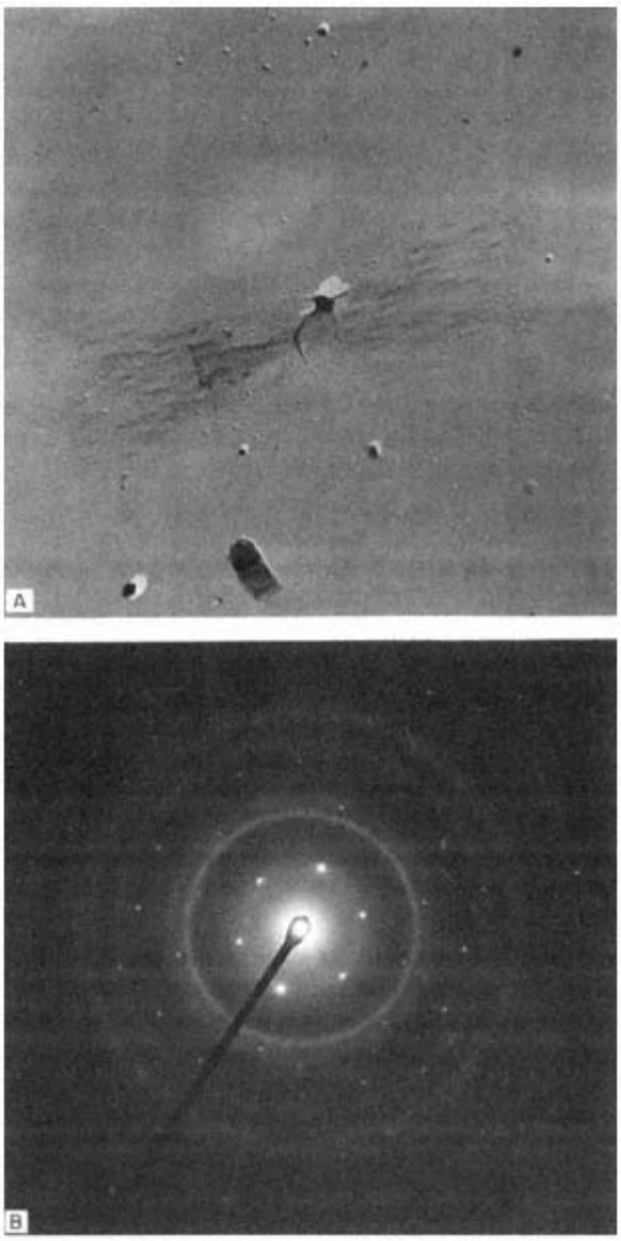

Figure 28
Electron diffraction pattern (B) from a solution grown single crystal of polyethylene sulfide (A).
(From Ref. 54.)

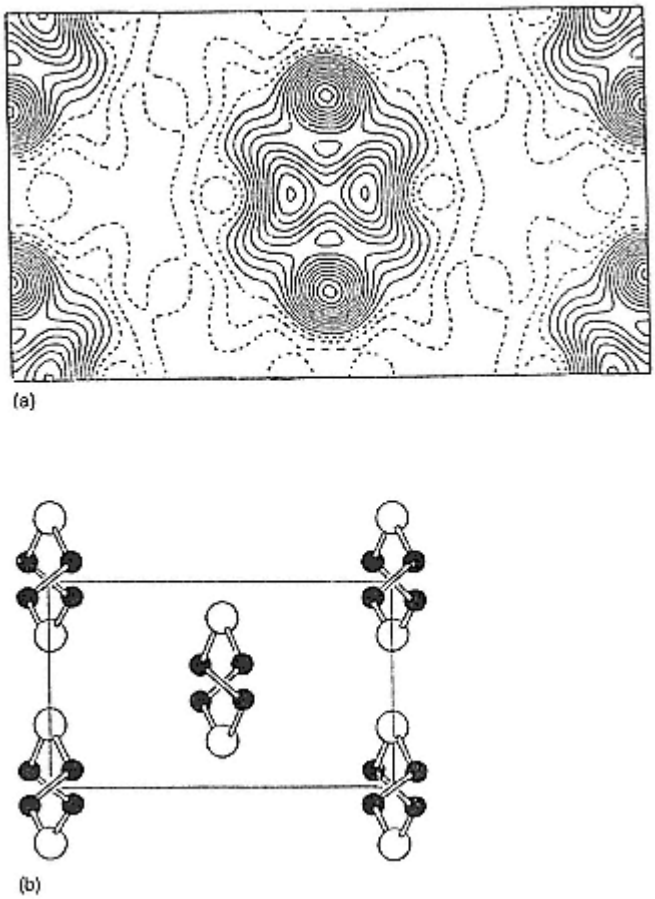

Figure 29
(a) Electron density of the polyethylene sulfide crystal projected on the hk0 plane and (b) corresponding projection of the unit cell.
(From Refs. 54 and 55.)

with free surfaces will yield samples with few tie molecules. When single stage replicas are made, one or a few lamellae may adhere to the replica, permitting electron diffraction. It must be recognized, however, that in "thick" samples, particularly with free surfaces, low-molecular-weight and less crystallizable polymer molecules may exude to the surface during crystallization, causing concern over the representativeness of the patterns obtained.

Fibers often have a skin—core as well as a fibrillar morphology, with weaker cohesion between the skin and core and between the fibrils than between the molecules within the structural units. R. Scott showed many years ago [60] that it was

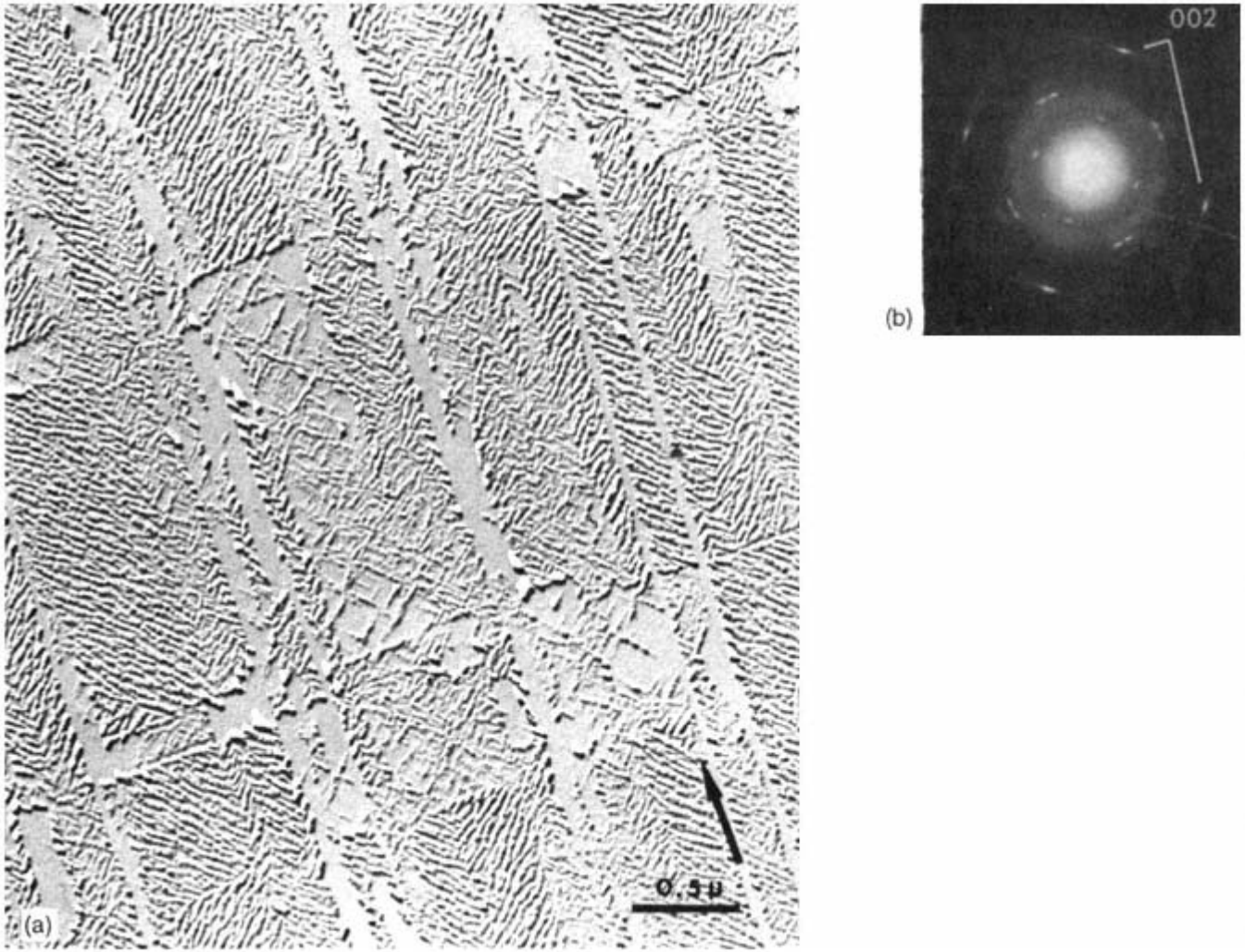

Figure 30
(a) Lamellar crystals of LPE crystallized from xylene solution at 108°C on a cleaved NaC1 crystal. Arrows indicates an NaCl [100] direction. (b) Corresponding ED pattern from a thicker sample crystallized at 88°C. (From Ref. 57.)

possible, for some fibers, to nick the surface with a razor blade and strip off a thin "ribbon," thin enough in some areas to obtain ED patterns and dark-field micrographs even in normal (100 kV) TEMs. These yield, however, fiber rather than single-crystal patterns.

Another "neat" technique for producing drawn films suitable for ED was developed by Gohil and Petermann (for detailed description see Ref. 61). The films are "extracted" from a molten pool, being drawn to varying degrees in the molten state and cooled rapidly, resulting in crystallization from an oriented state. The resulting shish-kebab morphology before and after annealing yields fiber-type ED patterns.

Fiber patterns can also be obtained, and most often have been obtained, by shearing (or "smearing") a polymer melt (e.g., with the edge of a razor blade or glass slide) on a glass slide. Following cooling, usually rapidly to prevent relaxation, the films are often annealed below T_m to develop improved crystallinity. Examples are shown in Fig. 31 for poly(2,6-oxynaphthoate) (PONA); after annealing below $T_{k\text{-}m}$, the film was sheared above $T_{k\text{-}m}$, that is, in the liquid crystal state. This pattern, which is similar in the diffuseness of the equatorial reflections to that in x-ray patterns from fibers of the same polymer (with 006 only being seen by tilting), should be compared with the single-crystal whisker patterns in Fig. 37.

On occasion, preferred orientation of an hk0 plane relative to the substrate is obtained. For a family of polyether liquid crystal polymers, single-crystal patterns (h01) were obtained, but this is not normally the case. The polyether patterns (Figures 32(a) and 32(b) demonstrate the problems arising from triclinic and monoclinic cells; although c (the molecular axis) is parallel to the shear direction, $\mathbf{c}^*$ is not. Rotationally averaging this type of pattern, as observed from fibers, makes determination of indices much more difficult.

Recently [64] we have described the confined thin-film melt polymerization (CTFMP) technique for preparing lamellar (single crystal and single disclination

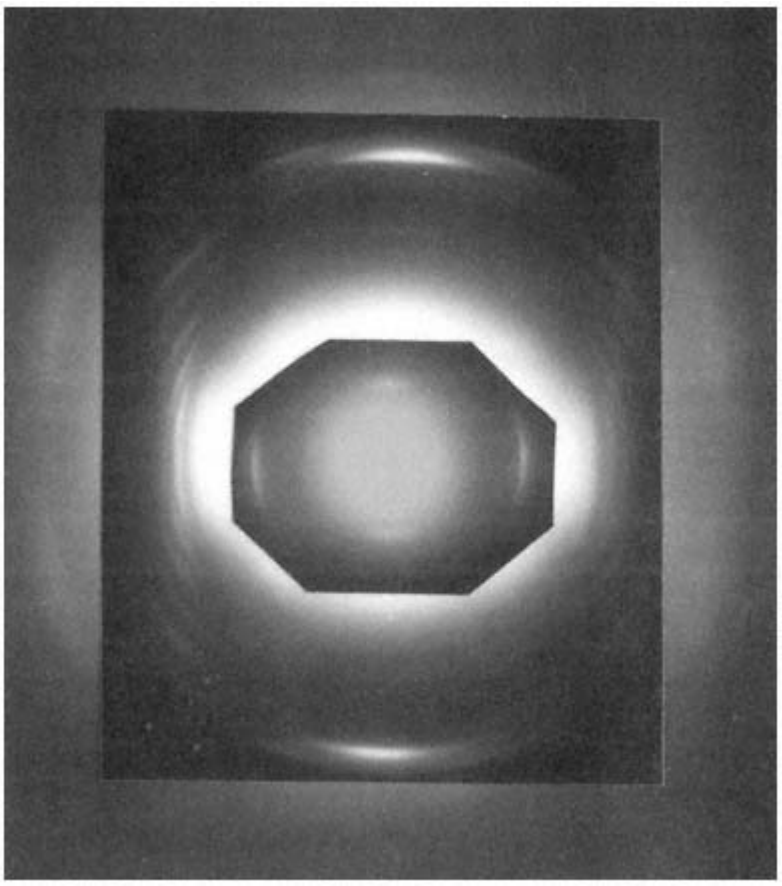

Figure 31
CTFMP-polymerized PONA sheared at 280°C.
(From Ref. 62.)

domain) samples suitable for ED. Initially applied to thermotropic liquid crystal polyesters, it appears more broadly applicable (for review see Ref. 65) to condensation polymers in general, including copolymers. The CTFMP technique involves the simultaneous polymerization-crystallization (in some cases in the liquid crystal form initially) of the monomers in a thin film between glass cover slips; the result is extended chain lamellae, which, for reasons unknown as yet, are often ~100 Å thick, regardless of polymerization times and temperatures. An example, for poly (2,6-oxynaphthoate) (PONA) [34a] is shown in Figure 33, with ED patterns (phase I and phase II) in Figure 34. The availability of patterns such as this, even if only they are available, greatly simplifies indexing of x-ray or ED fiber

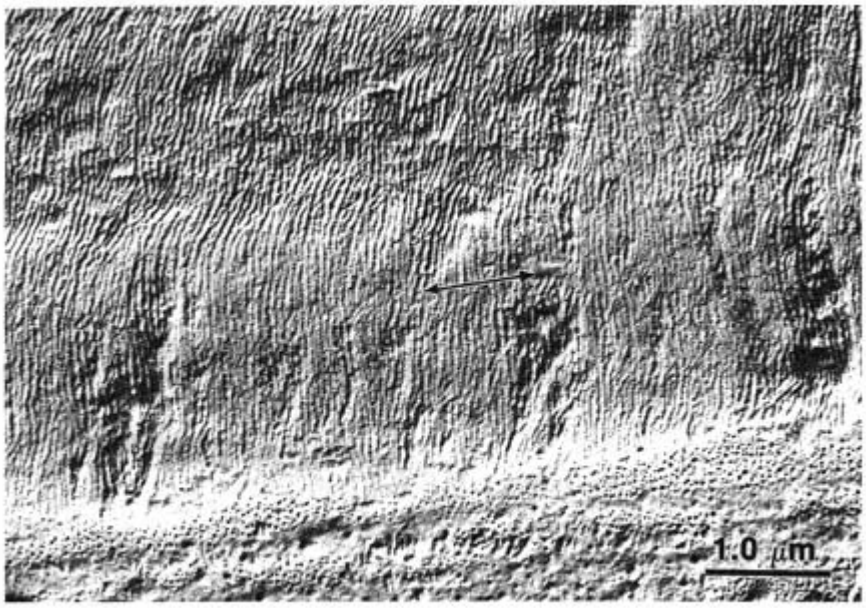

(a)

Figure 32
(a) TEM micrograph of a sample of an aromatic aliphatic azomethine polyether (C_{10} aliphatic segment) sheared et 195°C and annealed at 150°C, 2 hr ($T_{k\text{-}m}$ = 175°C). The thickness of the lamellae, which are normal to the substrate and shear direction, is ~400Å; they consist of extended chains.

patterns. This is particularly true if two (or more) phases are present simultaneously in the "fibers."

Figure 35 shows micrographs and ED patterns of PET crystals prepared by the CTFMP technique. PET has a triclinic unit cell; thus if the **a** — **b** (hk0) real space plane is parallel to the substrate, **c** will lie at an angle (here substantial) to the beam direction (the normal to the substrate) as well as $\mathbf{a}^*$ and $\mathbf{b}^*$. This appears to be the case for the PET crystals polymerized-crystallized at 200°C, and only a few or no reflections can be obtained without tilting the sample in the microscope. On the other hand, for the crystals in Fig. 35c, **c** is parallel to the beam, $\mathbf{a}^*$ and $\mathbf{b}^*$ lie in the plane of the substrate, and hk0 ED patterns with several orders of reflections are obtained (Fig. 35d). Unfortunately, the thickness of these crystals, which consist of numerous (twinned) lamellae lying at an angle to the substrate, is such that dynamic diffraction is occurring; the relative intensities of the various reflections are "incorrect," and normal kinematic diffraction equations for the relation between intensity (amplitude) and atomic positions cannot

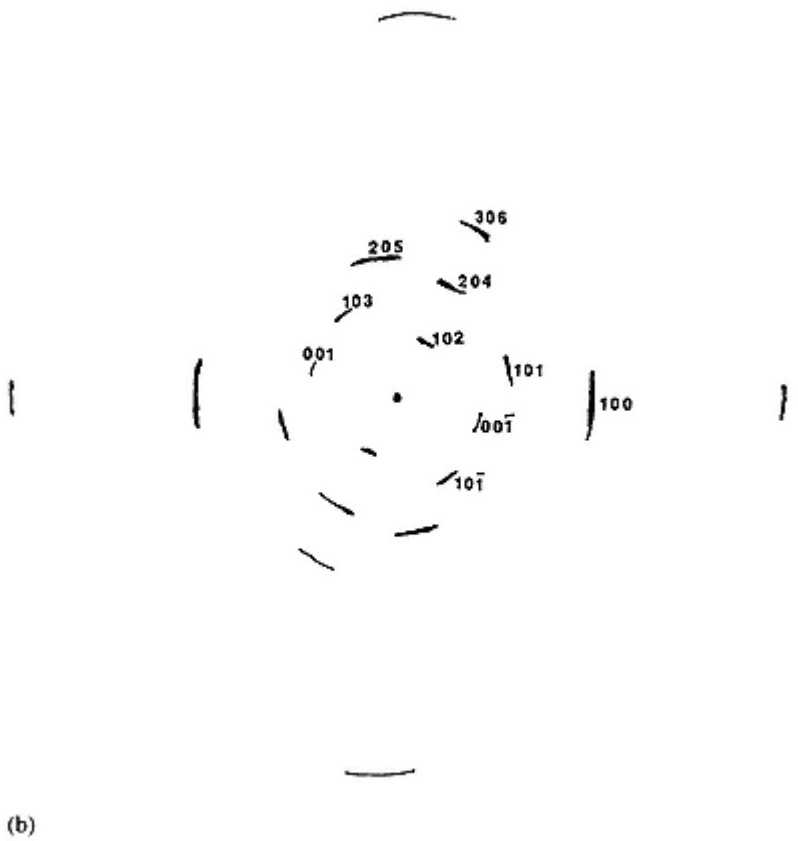

Figure 32
(continued) (b) Schematic diagram of an ED pattern from the sample in (a). This is a single crystal h01 pattern with the polymer having a triclinic unit cell (i.e. c^* is at an angle to c). The fiber axis is vertical. (From Ref. 63).

be used. The "correct" distribution of intensities, based on the crystal structure described by Daubeny et al. [45], is shown in Figure 36. The Wilson test can be used to determine if the observed variation in intensities is affected by dynamic diffraction [67].

In a few cases hk0 zone (i.e., containing 001 reflections) single-crystal patterns have been obtained for polymers by both x-ray and ED. For the former solid-state polymerization (e.g., of POM from needle crystals of trioxane [68]) has been used. For the latter, whisker-type single crystals have been grown, by polymerization-crystallization, from solution for a number of thermotropic liquid crystal polymers (see Ref. 69 and references therein). An example, for PONA, is

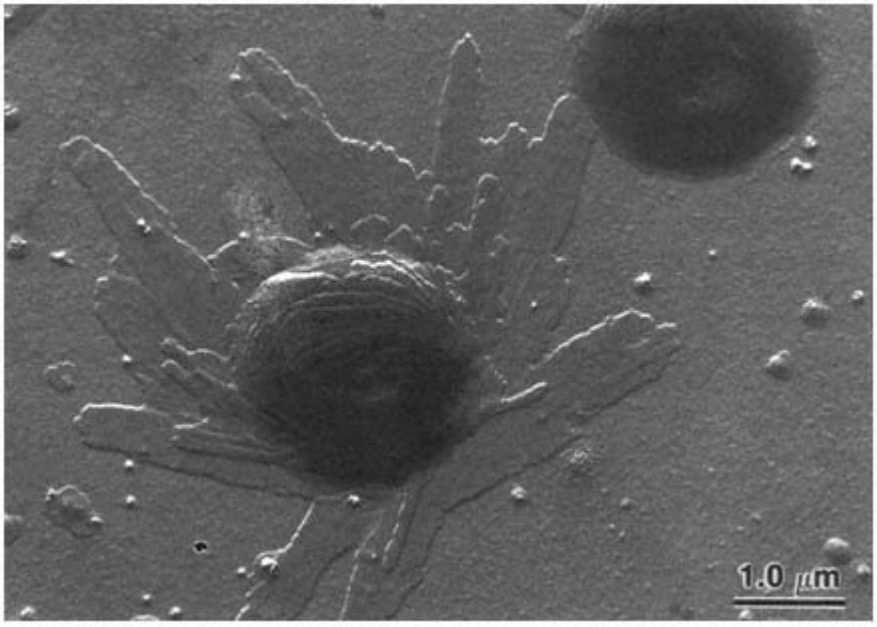

Figure 33
Lameliar single disclination of PONA, with protruding single-crystal lamellae, grown by the CTFMP technique at 180°C.
(From Ref. 66.)

shown in Figure 37. Although x-ray powder patterns have been interpreted in terms of an orthorhombic unit cell [70], clearly these patterns (with the equatorial reflections corresponding to phase I, Figure 34) indicate a monoclinic unit cell. Crystal packing simulation, using Cerius^2, suggests the conformation and packing (parallel chains) shown in Figure 38, with the corresponding predicted patterns. The agreement, while close, is not totally satisfactory. Antiparallel (or statistical) chain packing is not expected, based on the polymerization process. The lateral streaks on some of the meridianal reflections is attributed to an axial disorder, for instance an occasional reversed chain direction.

Dark-field microscopy (Figure 37a, insert) shows a clear center line in the whiskers (also seen in PpABA whiskers); it is assumed this is the location of the H-bonded region of the original dimers, with growth in both directions on the acetoxy ends of the monomers, that is, parallel chain packing in each half of the whisker but in opposite directions. In the CTFMP lamellae the carboxy ends are presumed to attach to the glass surface (resulting in excellent adhesion), the chain direction being the same (acetoxy upward) in all of the lamellae in a given crystal or disclination domain. This permits rapid end-linking (chain extension), as is observed when the samples are heated above their $T_{k\text{-}m}$.

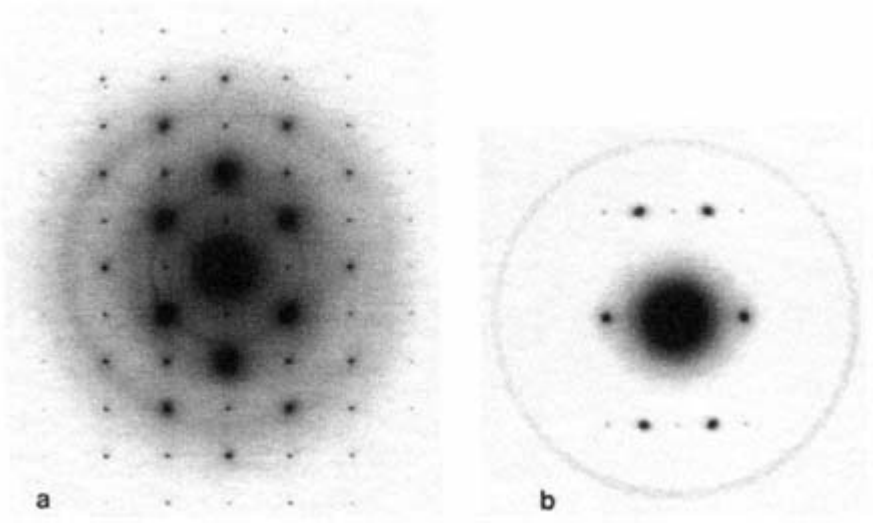

Figure 34
ED patterns of PONA phases I (a) and II (b) from CTFMP single crystals.
(From Ref. 66.)

Both x-ray and ED can be used to follow changes in the molecular packing and conformation with temperature. Again ED has an advantage, if the samples are suitable, of being able to follow the changes in a single crystal (patterns). Examples, for PpOBA phase I and II (similar to the PONA lattice packings in projection along **c**), are shown in Figure 39. Although in most polymers beam damage is sufficiently high that different crystals are used for patterns at successively higher temperatures (or longer times at a given temperature), in these aromatic ring-containing polymers several patterns could be obtained from the same crystal as it was heated. Clearly there is a gradual change from the low-temperature crystal form to the high-temperature form (here over a 50°C temperature range) within an individual crystal, with diffuse scattering streaks (representing disorder) connecting pairs of reflections, a superlattice type structure at intermediate temperatures (shown by the satellite reflections), and considerable order in the hightemperature forms. The proposed transformations are shown in Figure 40-a. Furthermore, on cooling, there was shown to be a memory effect, of both phase and lattice orientation, with none of these effects being observable by x-ray diffraction, which averages over the entire illuminated volume. On the other hand, it is possible some of the observed ED effects are caused or affected by the adhesion to the substrate, with this adhesion preventing free rotation of the chains. The latter has been suggested to occur in the high-temperature form, at least segmentwise (phenyl rings and carbonyl groups), based on dielectric and broad-line NMR

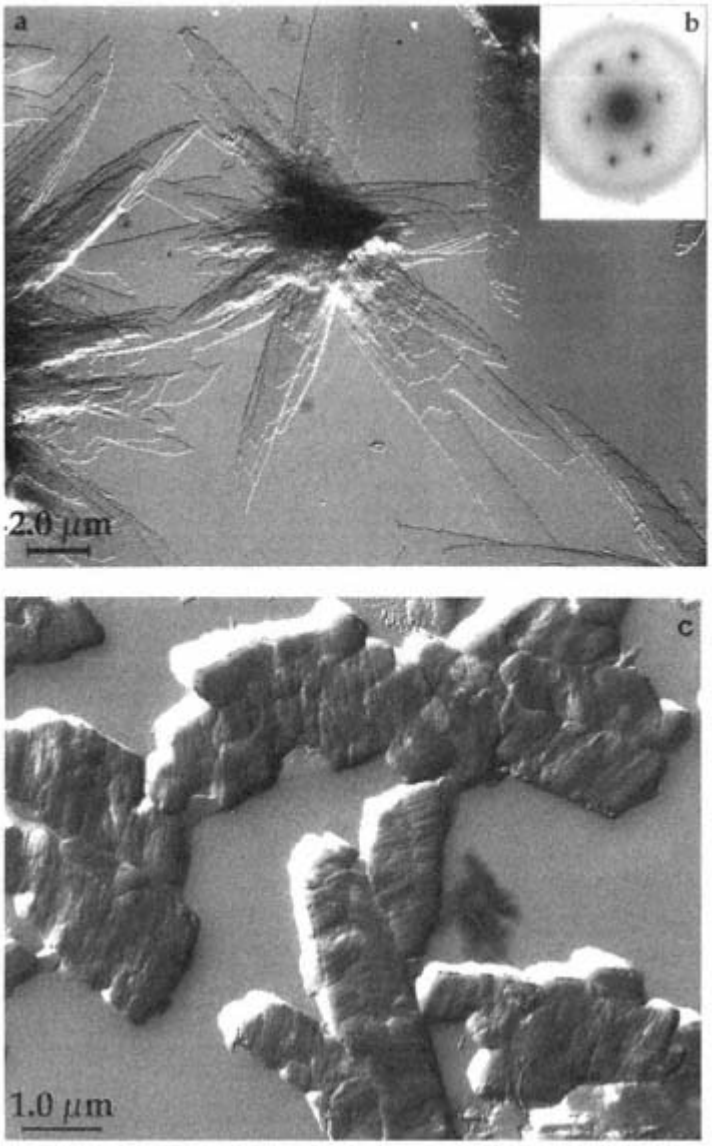

Figure 35
CTFMP single crystals of PET polymerized at (a) 200°C, 10 hr and (b) its ED pattern obtained by tilting the crystal 27°C, (c,d) Micrograph and ED pattern (no tilt) of a PET crystal grown (polymerized) at 225°C, 6 hr.
(From Ref. 49.)

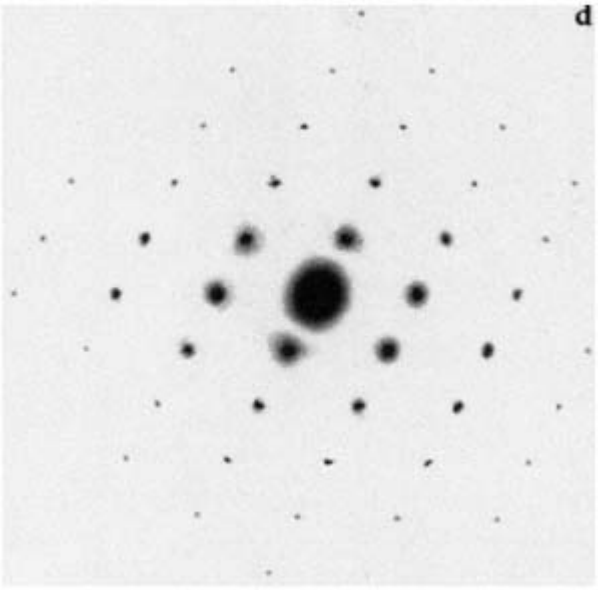

Figure 35
(continued)

measurements [72,73]. In our samples, in which the high-temperature forms (Figure 40-b) are metrically hexagonal, but are both orthorhombic, the phenyl ring orientation is maintained, leading to a difference in intensity of the 200 and 110 reflections, despite their identical spacings. If this occurs in the bulk samples, it again could not be observed by x-ray diffraction.

An important factor to note in all of the foregoing discussions of interpretation of diffraction results is that while disagreement between the intensities predicted on the basis of particular model of molecular conformation and packing can prove the model incorrect, agreement does not prove it to be correct. Another model may also be found leading to similar or better agreement. Furthermore, even if disagreement occurs, caution is needed in rejecting a model; we have found that only slight shifts in axial position or molecular conformation can lead to substantially improved agreement.

There have been limited applications of high-resolution TEM to lattice imaging of polymers, with recent image processing techniques permitting resolution of individual molecules (for review see Ref. 74). Although they were initially thought limited to highly radiation-resistant polymers, such as poly(*p*-xylene) (PPX) and poly(*p*-phenylene terephthalamide) (PPTA), even PE single crystals have yielded lattice fringes (Figure 4 l-A).

Figure 41-B is an example of the application of image processing to a PPX single crystal. Figure 41-B (b´) is the ED pattern from a β form crystal as shown

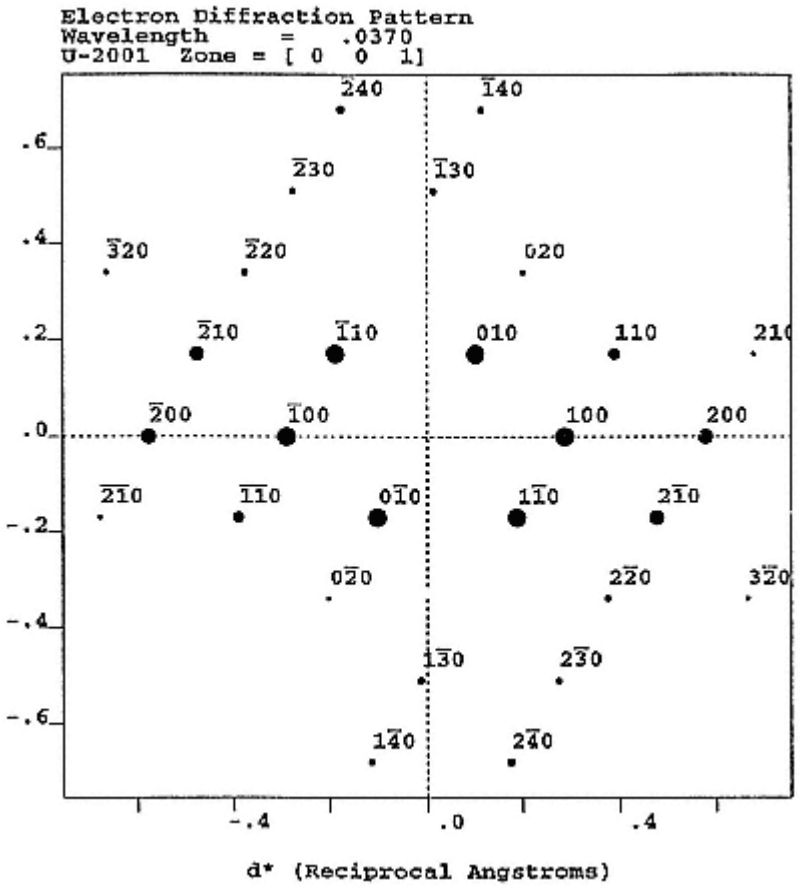

Figure 36
Simulated ED pattern based on the crystal diagrammed in Figure 26. Note the 020 and higher order 0k0 reflections are much weaker than in the pattern; this is tentatively attributed to dynamic diffraction. (From Ref. 49.)

in Figure 41-B (a´). Its high-resolution dark-field image, taken using the encircled 400 reflection and its satellites, is shown in Figure 41-B (c´); and 18-Å 400 planes can be seen in two of their three directions. In Figure 41-B (d´) an optical diffraction pattern taken from the original negative (currently the negative would be scanned and the Fourier transform calculated using a computer) is shown; the similarity to that in (b´) is clear. An optically filtered (mask with holes placed over the diffraction spots in the optical bench used to reform the image) image is shown in Figure 41-B (e´); in the image one is looking down the molecular axis. This corresponds to taking the inverse Fourier transform with only the "spots" of

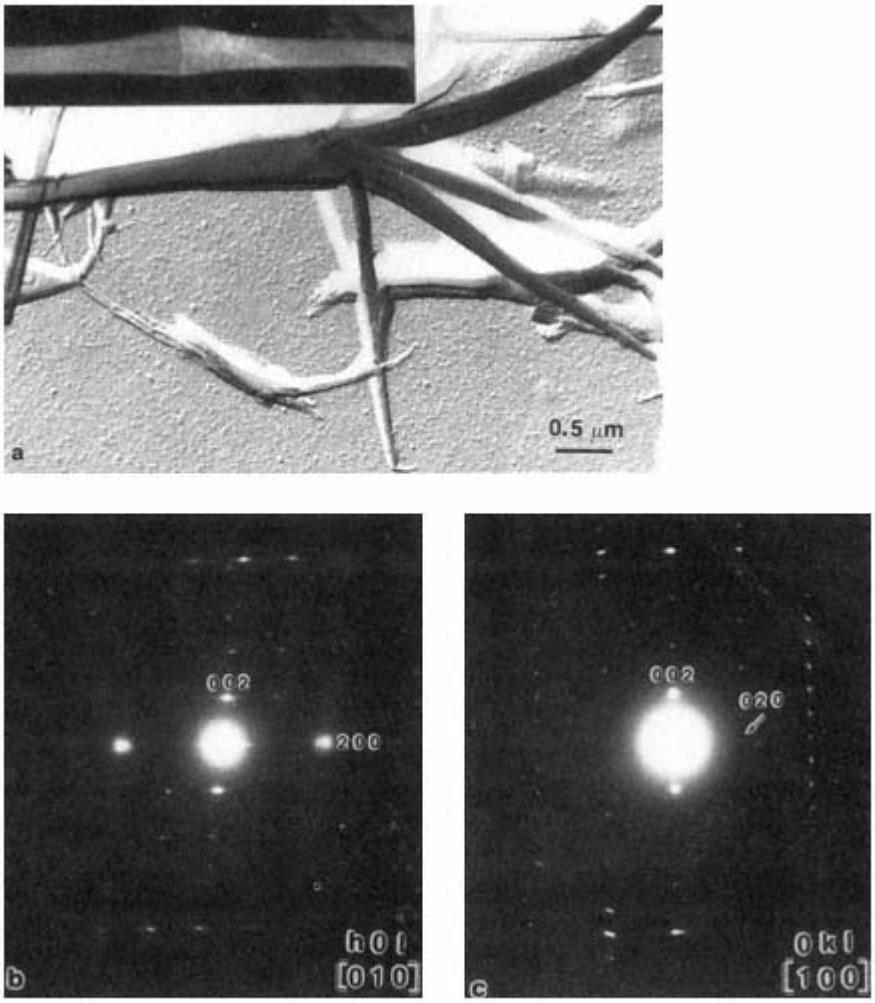

Figure 37
(a) PONA whisker with (b) [010] (h0*l*), and (c) [100] (0k*l*) zone ED patterns.
A dark-field micrograph using hk0 reflections is inset in (a).
(From Ref. 69a.)

the initial transform being used. Figure 41-B (f´) is a representation of the image, with (g´) being the unit cell as derived from a crystal structure analysis using WAXD [76b].

Figure 41-C is an example of the application of high-resolution TEM to fragments of a PPTA fiber. Using 006 and 110, 200 reflections of the ED pattern (a´)

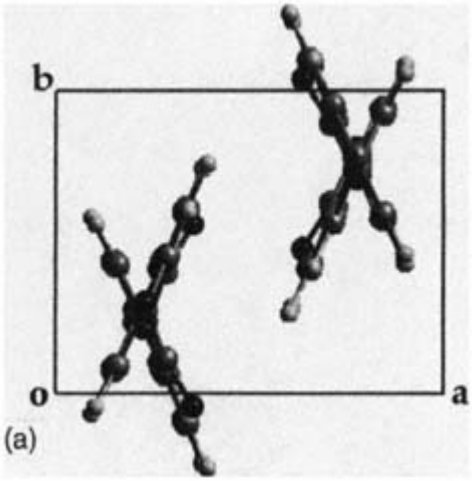

Figure 38
(a) Crystal structure (a,b,c) suggested by the Cerius [2] simulation program for PONA phase I with corresponding simulated ED patterns, (d) [001], (e) [100], and (f) [010]). (From Ref. 66.)

the dark-field images in (b´) and (c´) were obtained. The 006 image suggests alternating domains in and out of diffracting position; this can be related to the pleated sheet conformation of the fibrils and molecules in the fiber [76d]. Using the 110, 200 reflections, from planes parallel to the molecular axes, small crystallites are seen randomly everywhere along the axis. In Figure 41-D is shown a highresolution image of the sample along with its optical diffractogram. The 4.3-Å lattice fringes correspond to the 110 planes, with the bright areas with fringes being of the same size as the bright spots in the dark-field image. Some fluctuation in the fringe direction can be seen in the image with a slight curvature of the image being seen near the arrow.

In all of the foregoing the concentration has been on the conformation (and packing) of the molecule in the crystalline regions of a polymer. Conformations in the amorphous regions, being, almost by definition, more random, are more difficult to determine. As already shown, IR and Raman are useful for local conformations, such as relative numbers of trans and gauche conformers. Mobility of these constituent groups can be characterized by "broad"-line NMR, including spin—lattice and spin—spin relaxation-time measurements permitting determination of the temperatures (relaxation or T_g) at which the various types of groups can undergo rotation (see, e.g., Ref. 77). For characterization of the molecular conformation in amorphous regions, particularly of totally amorphous polymers, on a

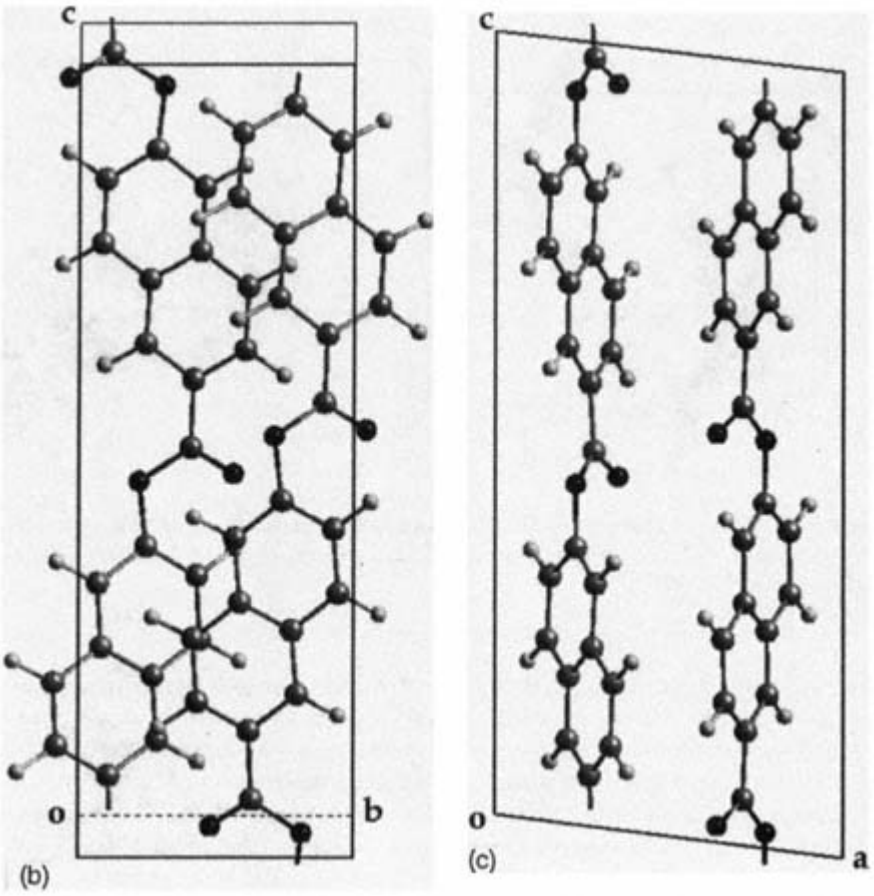

Figure 38
(continued)

larger scale, normally stated in terms of the mean square end-to-end distance, $\langle r^2 \rangle$, or radius of gyration, R_g, neutron scattering has been the primary tool. It depends on the difference in scattering power of ^1H and ^2H. In practice a dilute solution of deuterated polymer in hydrogenated (or vice versa) is prepared. The resulting (small-angle) neutron scattering pattern, interpreted in the same way as the light-scattering patterns from dilute solutions of a polymer in a solvent, yields R_g and, by assumption of a random coil, $\langle r^2 \rangle$. The interpretation also assumes the deuterated and hydrogenated molecules are thermodynamically perfectly miscible, a feature that does not always occur. However, for glassy amorphous samples, which can be quenched from the melt, this is of less concern than when similar studies are used to describe the conformation of chains in the crystalline regions of partially crystalline samples.

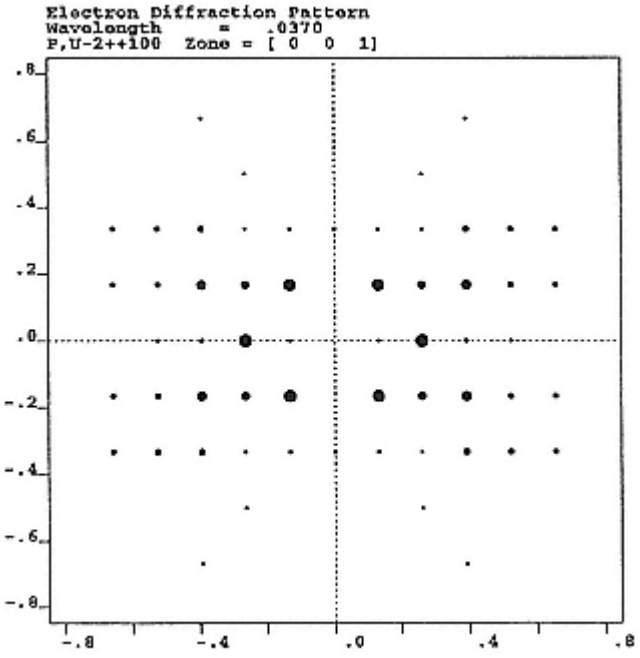
Electron Diffraction Pattern
Wavelength = .0370
P,U-2++100 Zone = [0 0 1]
.8
.6
.4
.2
.0
-.2
-.4
-.6
-.8
-.8
-.4
.0
.4
.8
d* (Reciprocal Angstroms)

(d)

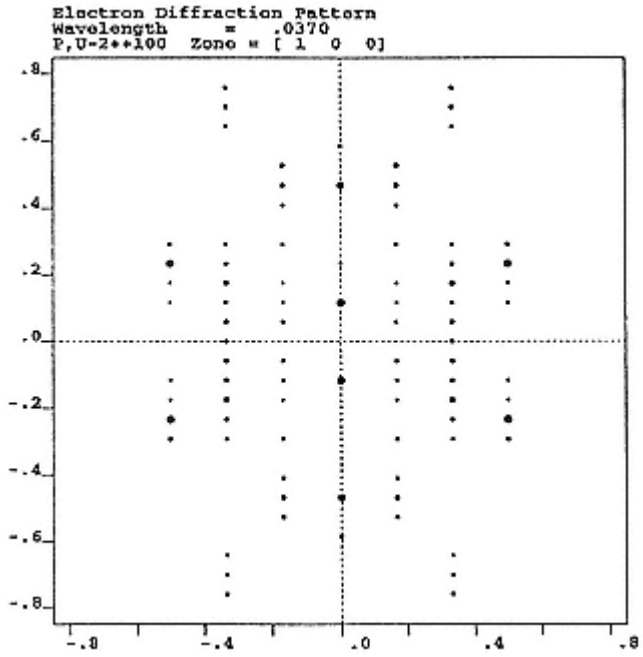
Electron Diffraction Pattern
Wavelength = .0370
P,U-2++100 Zone = [1 0 0]
.8
.6
.4
.2
.0
-.2
-.4
-.6
-.8
-.8
-.4
.0
.4
.8
d* (Reciprocal Angstroms)

(e)

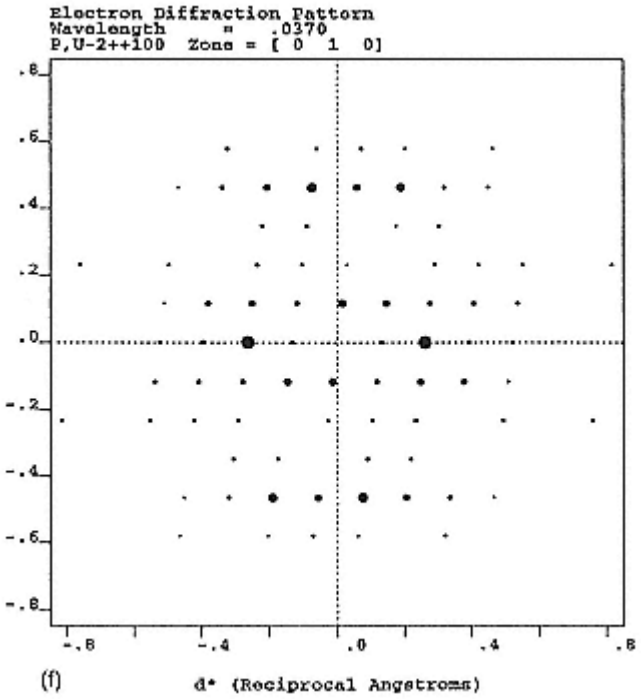

Figure 38
(continued)

In a recent development Wunderlich and co-workers [78] have used a fullpattern (two-dimensional Reitveld) wide-angle x-ray diffraction refinement [79], in conjunction with DSC, SAXS, and thermal mechanical analysis, to characterize the amorphous "structure" in a PET fiber. Based on a model of the crystallite structure, a three-dimensional diffraction pattern was calculated and then "rotated" to produce a two-dimensional fiber pattern for comparison with that observed at each point for which data was collected using a four-circle diffractometer. The latter collects data as for a pole figure. The model used incorporates parameters describing the average size of the crystallites in three dimensions, the distribution of orientation of the crystallites relative to each other and the average orientation relative to the fiber axis, the unit cell parameters, atomic positions (determined using a rigid body model), a temperature factor, a paracrystallinity matrix for defects of the second kind, and instrumental parameters.

Figure 42-A shows a contour plot of one quadrant of the observed fiber diffraction pattern, with Figure 42-B being the crystalline-phase diffraction pattern based on the model, with the background removed. Figure 42-C is the residual fiber scattering after subtraction of the crystalline scattering [i.e., (b) — (a)]. Assuming

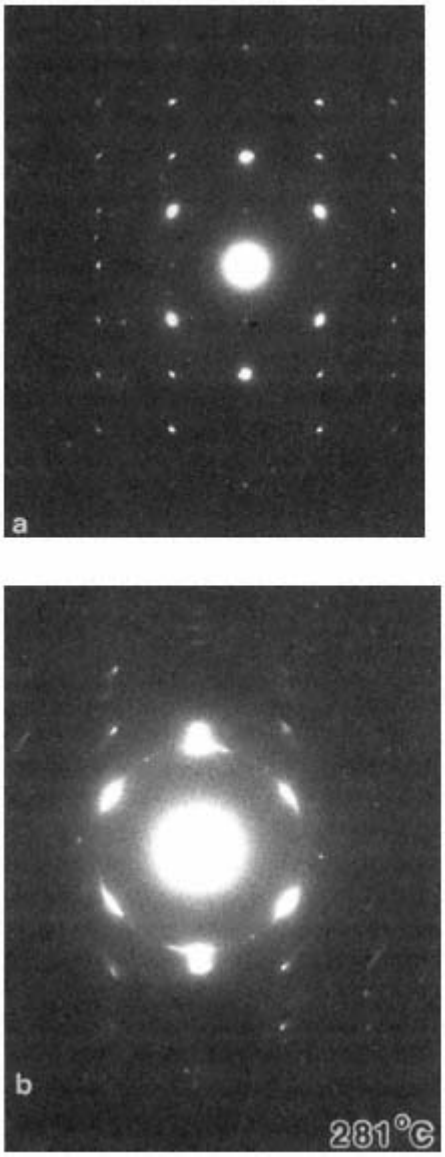

Figure 39
ED patterns of phase I PpOBA CTFMP crystals at (a) room temperature, (b) 281°C, and (c) 346°C with schematic (d) of 346° pattern. ED patterns of phase II ppOBA CTFMP crystals at (e) room temperature; (f) 282°C with (g) schematic, and (h) 346°C with (i) schematic.
(From Ref. 71.)

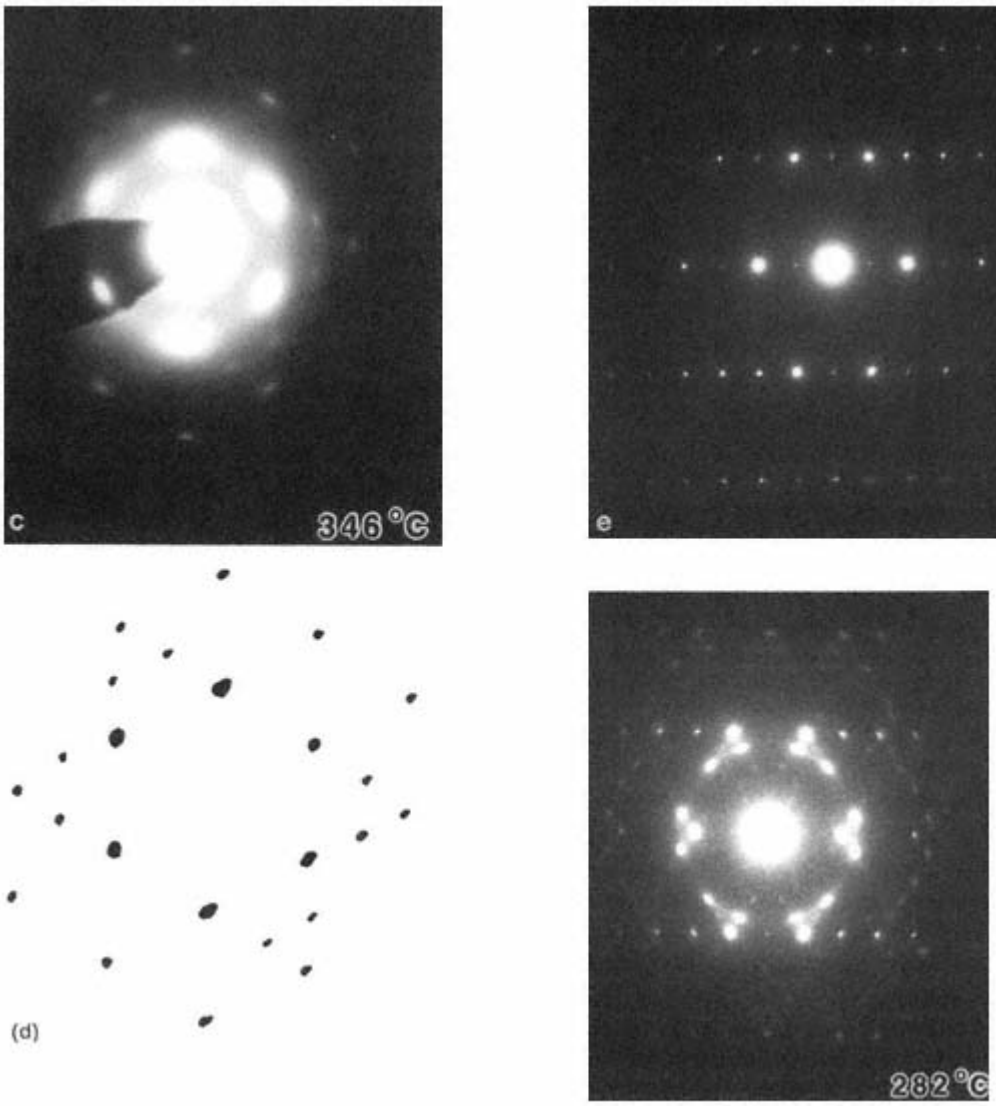

Figure 39
(continued)

the presence of an isotropic amorphous phase with a truly liquid-like structure results, when it is subtracted, in the pattern from the anisotropic, noncrystalline phase shown in Figure 42-D.

This anisotropic phase, defined as the intermediate phase, is clearly oriented, with the broad peaks at 0.2 and 0.28 $Å^{-1}$ on the equator being near the 010 and 100 reflections. Wunderlich and co-workers suggest the initial modulus of the PET fibers is primarily determined by the amount and orientation of the intermediate phase. The tenacity also is strongly dependent on this phase. They suggest it is

mainly present between the fibrils, with the "truly" amorphous regions being between the crystallites within the fibrils.

DSC measurements of the heat of fusion (yielding W_c), and the change in specific heat at T_g (yielding w_a) permit determination of the rigid (rigid above T_g) amorphous fraction, that is, $w_r = 1 - w_c - w_a$. This rigid amorphous fraction is presumed related to the intermediate phase. Figure 42-E shows a comparison of the three phases as determined by x-ray and DSC.

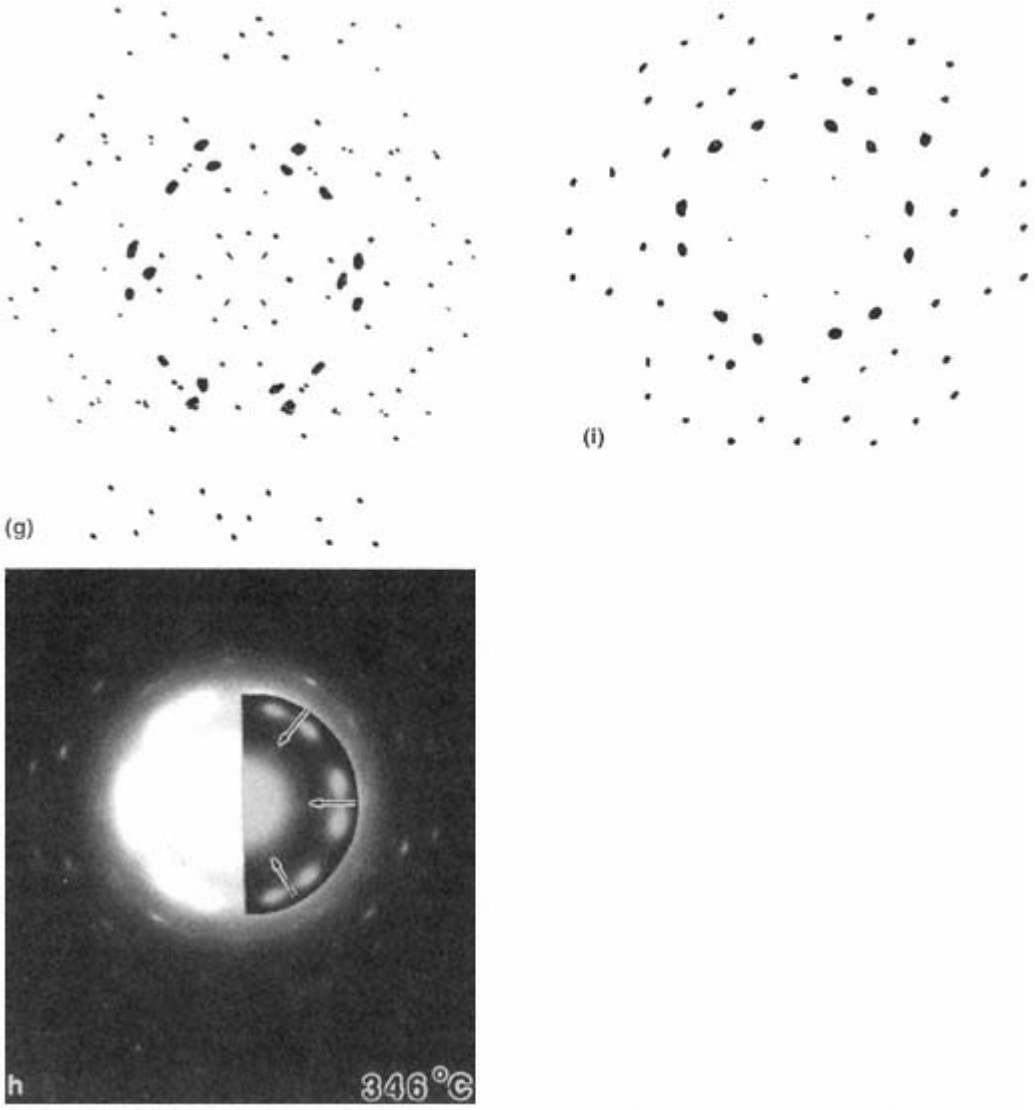

Figure 39
(continued)

B—
Degree of Crystallinity and Orientation

1—
Crystallinity

Determination of the degree of crystallinity, from which a single number representing the fraction of molecular segments in crystalline regions is desired, are, perforce, based on a two-phase model; that is, the segments (of lengths down to a

single C atom) are to be assigned to either a crystalline or amorphous region. Clearly, in reality this cannot be done, since, as will be seen, the assignment depends to some extent on the characterization technique used and the two-phase model ignores the possibility of intermediate degrees of order (and disorder).

Standard (traditional) techniques for characterizing the degree of crystallinity include x-ray diffraction, density, heat of fusion, and IR, with x-ray being, in one sense, the fundamental technique. All of these, however, characterize different aspects of the degree of order in the sample: for example, x-ray characterizes long-range order; density characterizes overall packing; heat of fusion characterizes changes in entropy as well as enthalpy; and IR characterizes short-range order. It is thus to be expected that the various methods will give different answers for a given sample even if the methods have been standardized (i.e., ASTM or ISO) for particular samples to give the same answers. For the density method, x-ray diffraction (or ED) is used to determine the volume and number of physical repeat units in the unit cell, permitting calculation of the density of a 100% crystalline sample. Likewise, heat of fusion measurements are calibrated against either density or x-ray measurements if 100% crystalline samples, as is usually the case, are not available. IR is, in some cases, calibrated similarly, with x-ray characterization of unit cell and conformation also aiding in the determination of appropriate bands to use. For details of the techniques, readers are directed to various general [27] and specific texts (for x-ray, Ref. 39; specific heat, Refs. 7 and 80; and for IR, Refs. 6–8).

In the simplest methods of x-ray crystallinity characterization, diffractometer scans of compression molded plaques (total thickness usually 1/16–1/8 in) are used. Various methods (see Ref. 39) can be used to draw in a line separating the background (air and incoherent scatter) from the polymer scattering over some preselected range of scattering angle 20 plus another line separating the crystalline

Page 74
Page 75

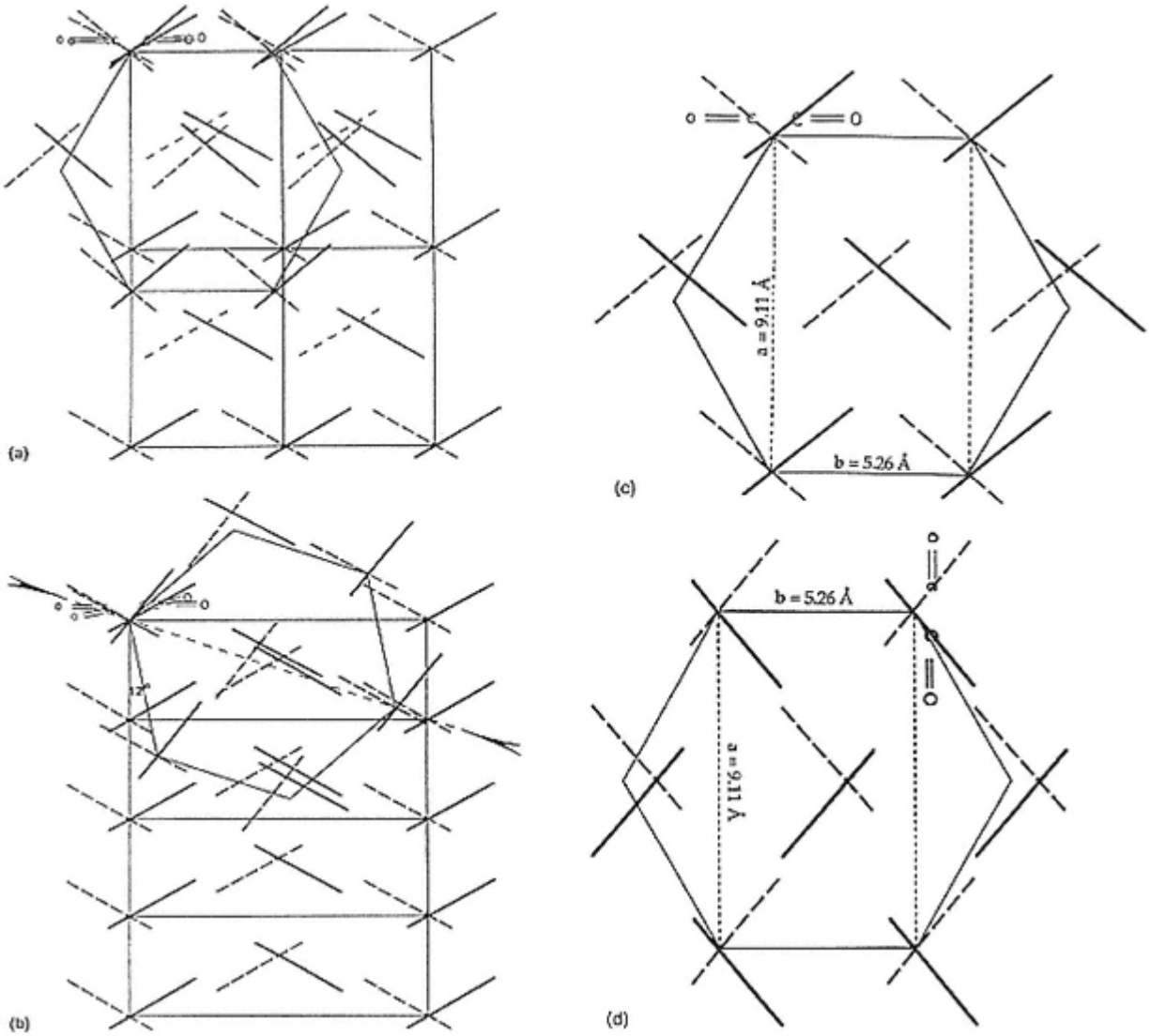

Figure 40
Proposed transformations of (a) phase I and (b) II PpOBA unit cells. Recent simulation (66) suggests the carbonyl groups (C=O)are closer to the planes of the phenyl rings in the room-temperature forms. Diagrams of the proposed orthorhombic high temperature (c) I (HT) and (d) II (HT) crystal structures. They are metrically hexagonal. The solid and dashed lines represent successive phenyl rings along the chain.
(From Ref. 71.)

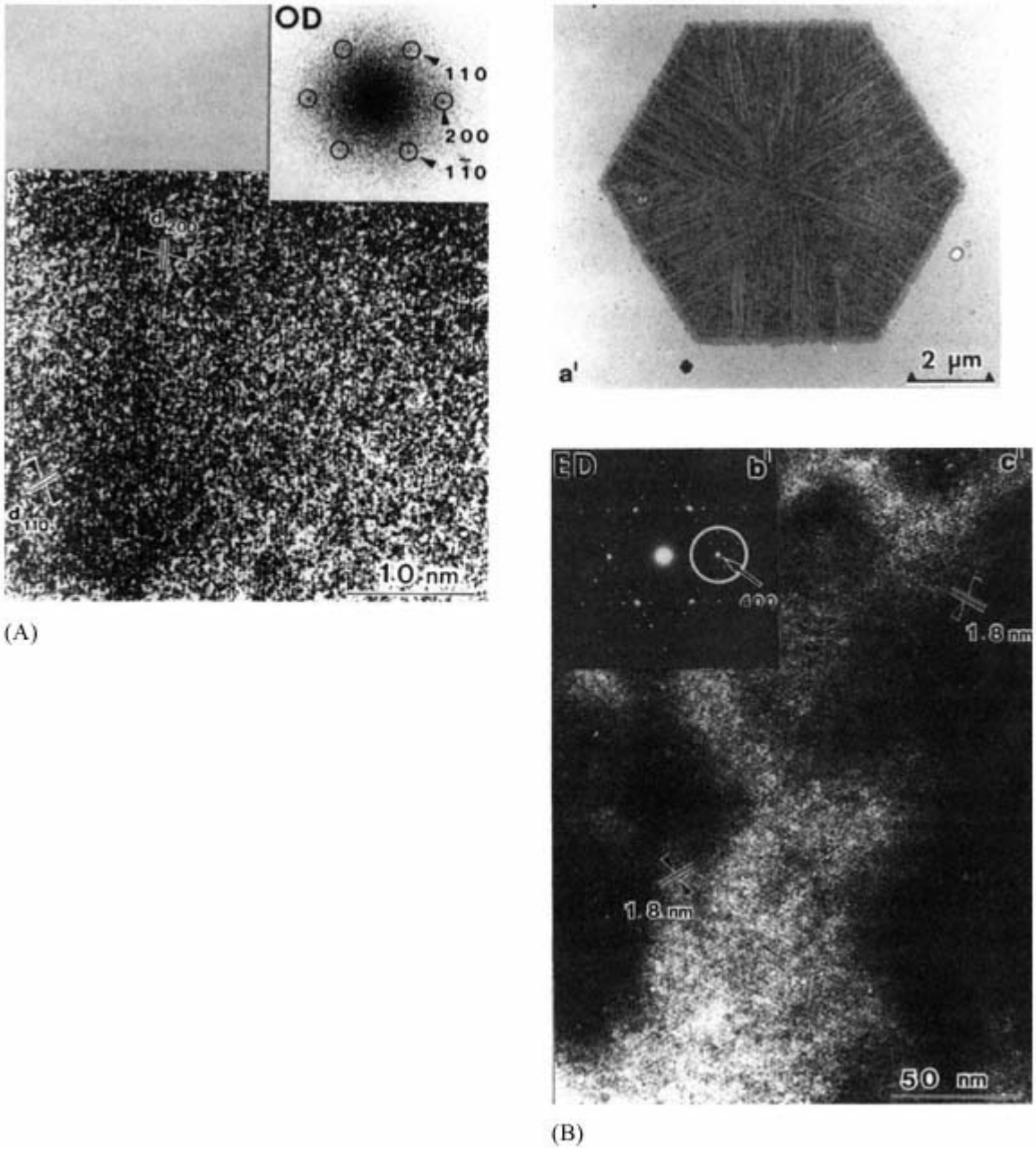

Figure 41

(A) Lattice image of a PE single crystal taken at a magnification of 90,000 at 4.2°K and 160kV (to reduce beam damage). Inset is the optical diffraction pattern from the negative indicating the 110 and 200 planes are resolved in the micrograph (From Ref. 75.) (B) (a´) PPX single crystal. (C) (b´) ED pattern of a β form. (c´) high-resolution dark field image taken using the encircled 400 reflection poly(p-xylylene) (PPX) (D) (d´) Optical diffraction pattern from a negative taken at 500kV, (e´) lattice image obtained by optically filtering the image, (f´) model structure based on ED, (g´) structural model showing orientation of the phenyl rings; the molecules at the comers statistically take one of the three equivalent orientations shown. The bold line on each phenyl ring represents the upper part of the ring. (From Refs. 76a,b.) (C) (a´) ED pattern and (b´,c´) dark-field micrographs of the PPTA sample used for (D). In (b´), using the 110 and 200 reflectionsm, small crystallites are seen, of approximately the same size as the domains showing the lattice fringes in (D). (From Ref. 76c,) (D) High resolution of a PPTA tom fragment from a Kevlar fiber originally annealed at 400°C. The molecular axis is vertical, with the insert pattern being the optical diffraction pattern from the negative. (From Ref. 74.)

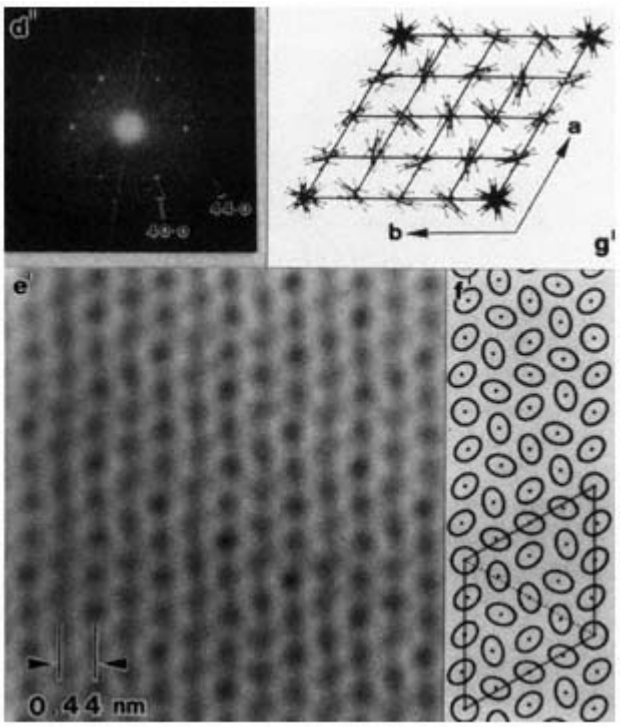

Figure 41(B)
(continued)

from the amorphous scattering (e.g., Fig. 43). The fractional crystallinity is then given by the ratio of the area of the crystalline scattering to the total polymer scattering, with the crystals having to have lateral (hk0) diameters of some 8–10 molecules to be considered crystalline. While the different methods give different absolute values, all (should) extrapolate for polyethylene to a 100% crystallinity at a density of 1.00 g/cm^3, corresponding to the density of the unit cell but to different densities for the (unattainable) 100% amorphous material. In our view, since it is known the two-phase model is incorrect, the relative values obtained by any of the methods can be used to predict variations in properties, with appropriate recognition of potential problems. The method can be used even for samples having more than one crystalline phase, either for individual crystallinities or overall values.

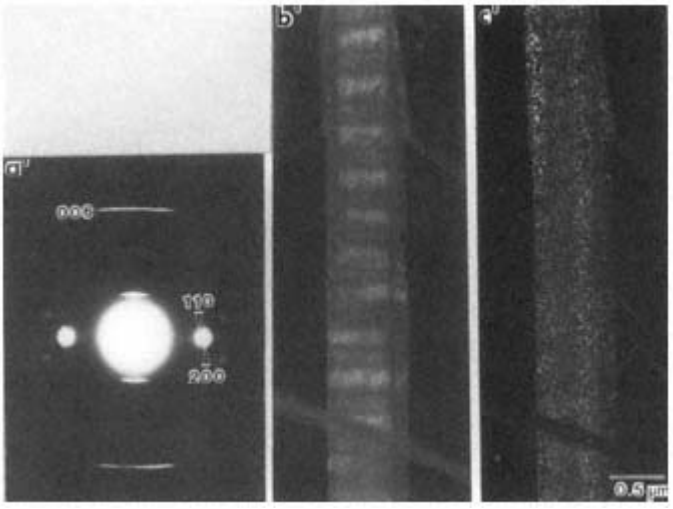

Figure 41 (C)

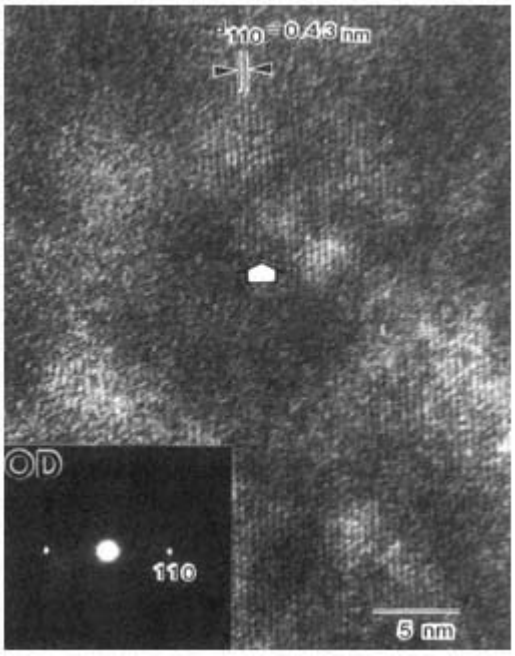

Figure 41 (D)

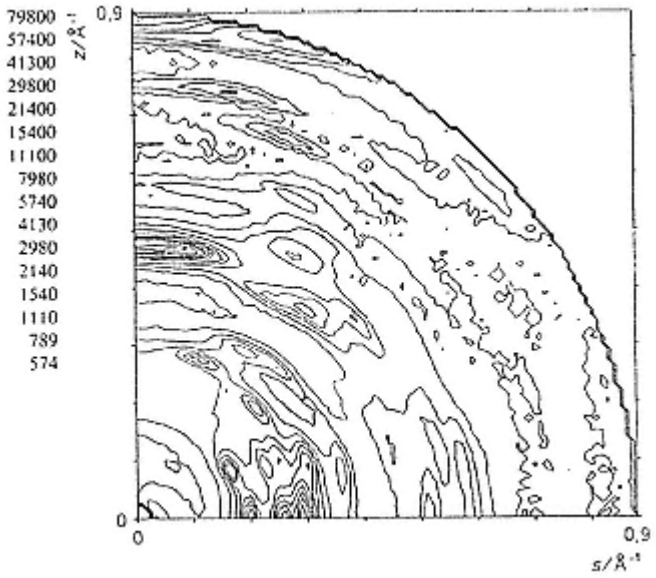

Figure 42-A
Contour plot of the observed pattern for a PET fiber (one quadrant only). The intensity values of the contours, starting from 0, are shown at the upper left. The pattern has been corrected for absorption, polarization, and Compton scattering.

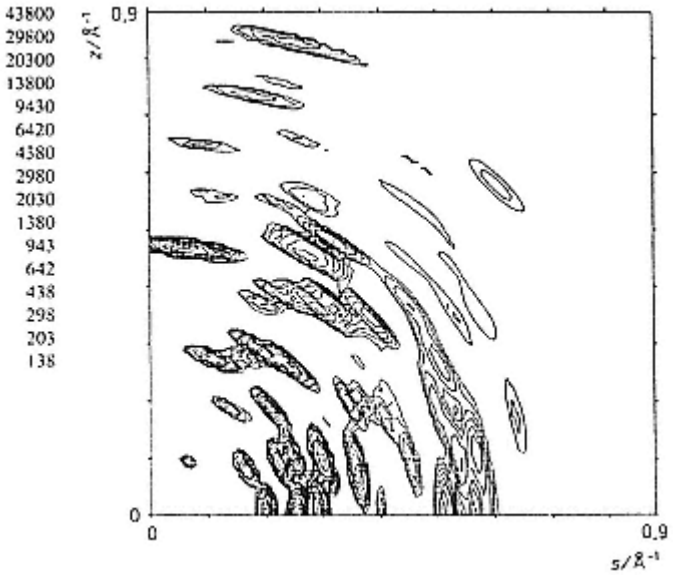

Figure 42-B
Contour plot of the crystalline phase diffraction. This can be compared with the plot in Figure 27-b.

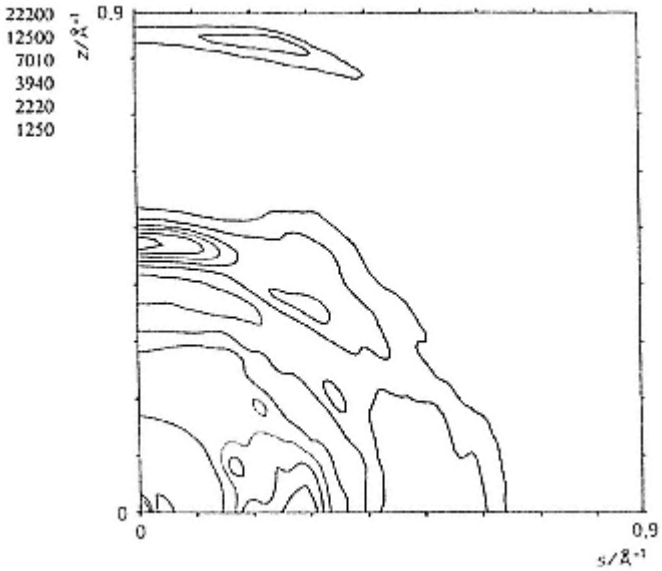

Figure 42-C
Contour plot of the noncrystalline scattering (i.e., A–B).

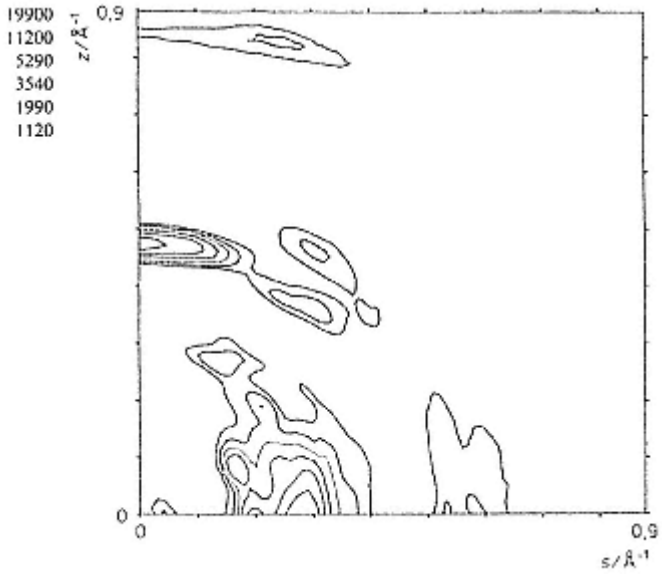

Figure 42-D
Contour plot of the anisotropic, noncrystalline (i.e., intermediate phase) scattering obtained from Figure 42-C by subtraction of an isotropic scattering.

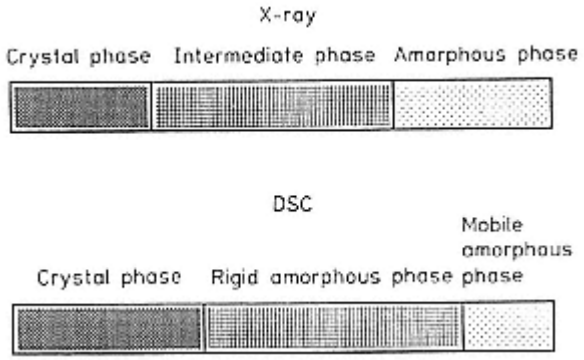

Figure 42-E
Comparison of the relative amounts of the three phasesas defined by x-ray scattering and DSC. (From Ref. 78b.)

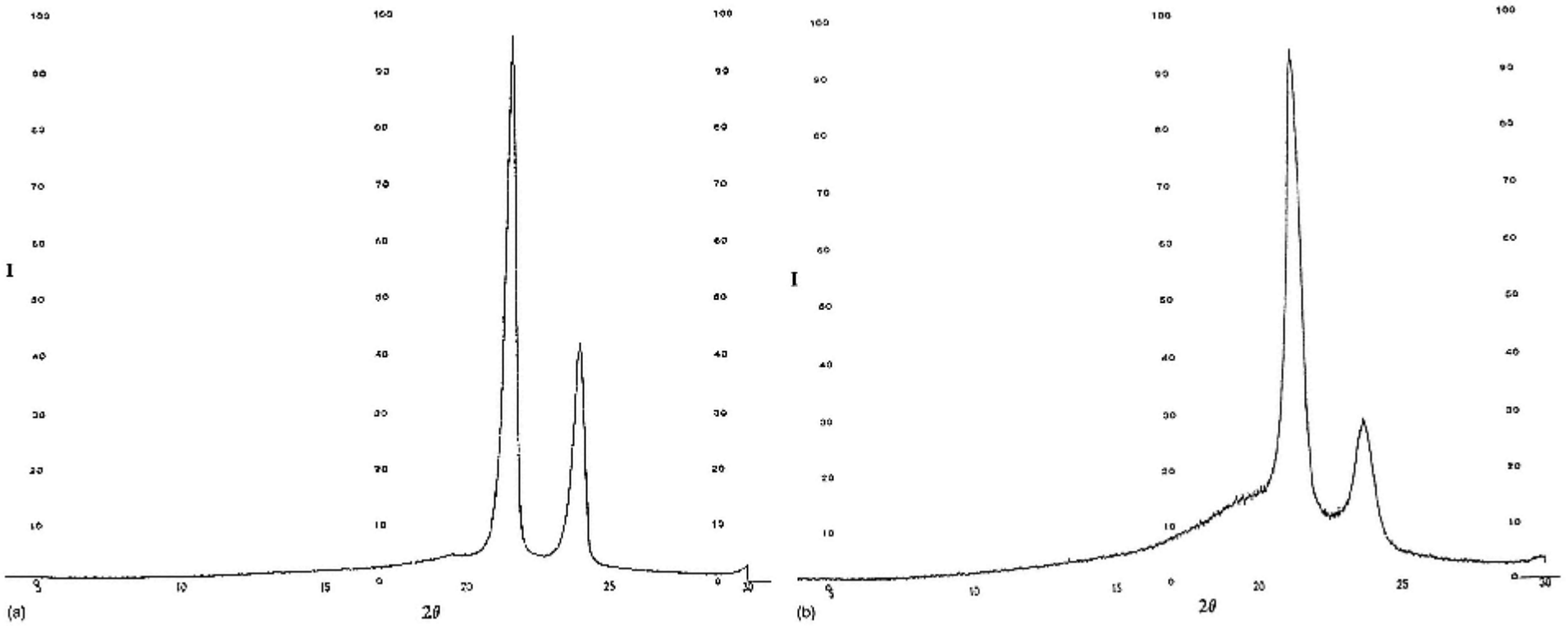

Figure 43
Wide angle x-ray diffraction patterns of PE samples of (a) 80%, (b) 55% and (c) 37% crystallinity.

For fibers a major problem in x-ray determinations of crystallinity is the need for random crystal orientation in the x-ray beam. By some means, such as chopping and mixing, the fibers need to be randomized in space. This is often difficult and thus other methods are more appropriate, with x-ray patterns from molded samples being used for calibration. In addition, if filled samples (e.g., pigment, plasticizers, fibers, etc.) are to be measured, diffraction from the addifives must be subtracted.

Density measurements can be made using density-gradient, columns or, more precisely, if thought useful, by flotation. Fibers, films, or parts of molded objects can be used, with the major problem being the presence of voids or fillers in the samples. In addition, if two crystalline phases are present, with different crystal densities, there is no way by density alone to separate their contributions or determine an overall value.

Thermal analysis, by differential thermal analysis (DTA) or DSC, can be used to measure the heat of fusion of small (~ 10 mg) samples. DSC measurements are more often used, with the peak areas being directly related to the amount of heat

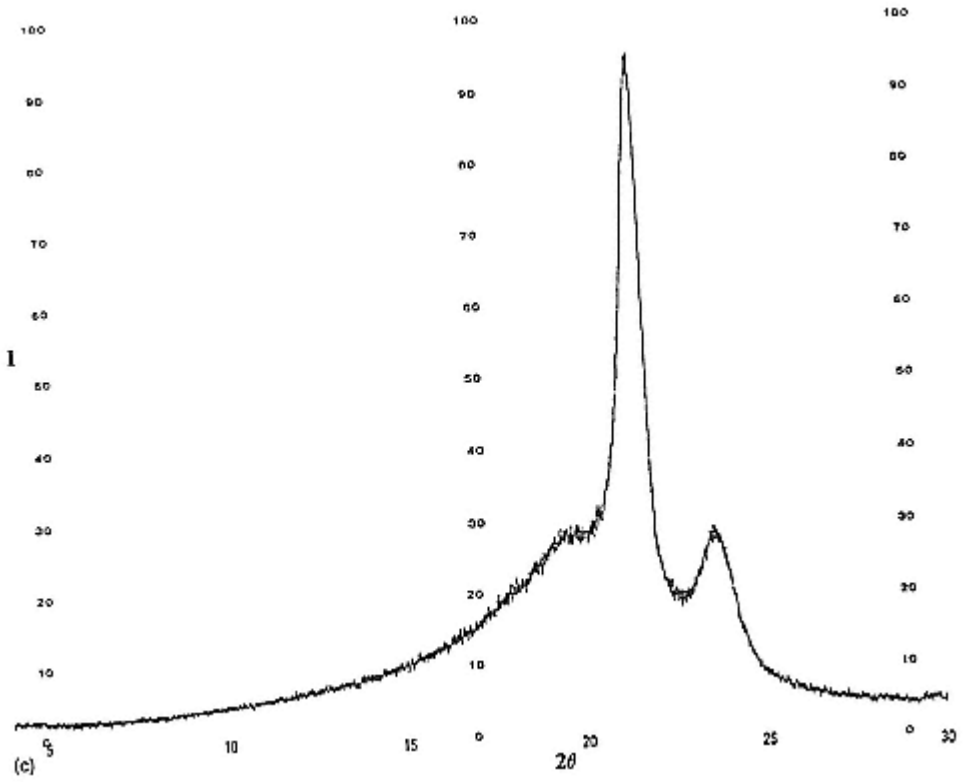

Figure 43
(continued)

absorbed by the sample as it melts, whereas DTA requires calibration. For traditional methods see Refs. 7 and 80. Required is either knowledge of the heat of fusion of a crystalline sample, or extrapolation as a function of crystallinity measured by x-ray or density. As in the case of x-ray measurement, a baseline needs to be drawn in, with ΔH_f being related to the area under the peak (see Fig. 44).

Problems arise if crystallization or annealing effects accompany the melting. Similar problems, for fibers, could result from relaxation of the orientation. A recent development [81], modulated DSC, permits separation of the reversible (heat capacity related) and nonreversible (kinetic) effects occurring during heating of the sample, with the difference giving the initial crystallinity of the sample (Fig. 44). In making these measurements, a small sinusoidal temperature variation (here ±0.53°C/40 sec) is superimposed on the 5°C/min heating rate. The total curve in this figure represents the normal DSC scan of a quenched PET sample. The T_g is seen as the change in baseline at 75°C. Crystallization from the glass (exothermic) is seen as the peak at 134°C (extrapolated onset 126°C), with a total ΔH of 36.40 J/g, while melting occurs with a peak at 253°C (extrapolated onset

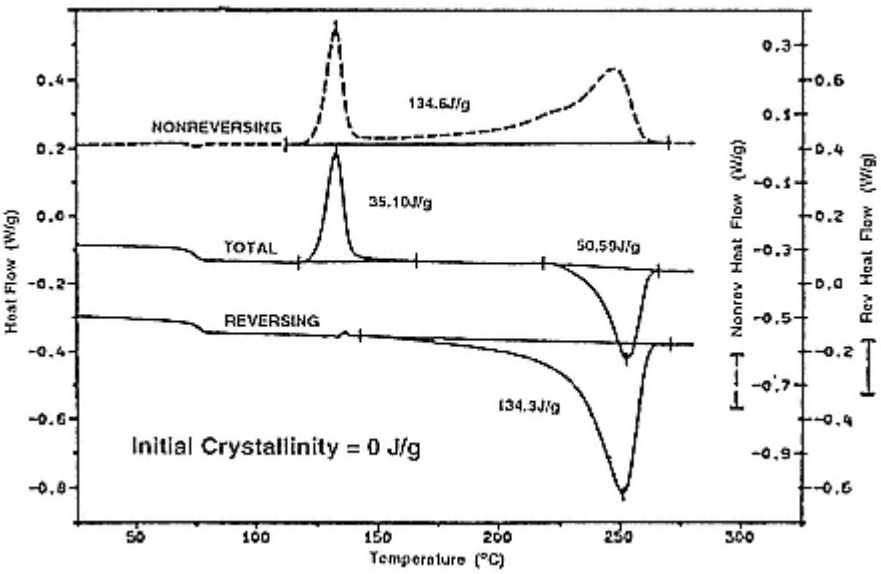

Figure 44
Modulated DSC scan of a quench-cooled PET film measured at a 5°C heating rate with a ±0.53°C amplitude modulation, 40 sec periodicity. The total scan is that normally measured with crystallization occurring at ~135°C, melting at 250°C. The "nonreversing" curve shows both crystallization at 135°C and further crystallization from ~175 to 240°C. The "reversing" curve represents the total heat of fusion of all the crystals formed during heating; because it is equal to the nonreversing ΔH_c it indicates there was no initial crystallinity. (From Ref. 81c.)

239°C) having an area of 50.59 J/g. This suggests some crystallinity was present in the initial sample, an amount that could be quantized if the ΔH_f for the crystal were known. However, the authors [49] claim x-ray indicates no crystallinity in similarly quenched samples. The reversing component of the total curve, with an area of 134.3 J/g and a single, broad peak at 250°C, represents the ΔH_f of both the initial crystallinity and the melting of all the crystals that formed during heating. The nonreversing component represents the exothermic crystallization processes occurring during heating. The cold crystallization peak at 134°C is the same as in the total scan, but additional ordering is seen to occur in two steps, at ~220 and 240°C. The total area is 134.6 J/g, the same as the heat absorbed during melting; that is, the sample had no initial crystallinity.

There are, in general, a number of structure-dependent IR (and Raman) bands; these include both those that are conformation dependent and those split due to the symmetry of the crystal. A list of these structure-dependent bands is given, for example, in Ref. 82. Since the conformation and the splitting are local-order, short-

range effects, crystallinity measurements by IR can differ significantly from measurements by other techniques. For instance, for PET, the ratio of trans CH_2 conformers to total ethylene glycol units (Figure 22), even though all segments in the crystalline regions have a trans conformation, does not represent the degree of crystallinity; as shown, trans conformers also occur in the amorphous region.

Another example is polypropylene (PP). In both the hexagonal and monoclinic crystal forms the molecules have a 3/1 helical conformation. The 1003 cm^{-1} band has been attributed to segments with this conformation, while the 1028 cm^{-1}

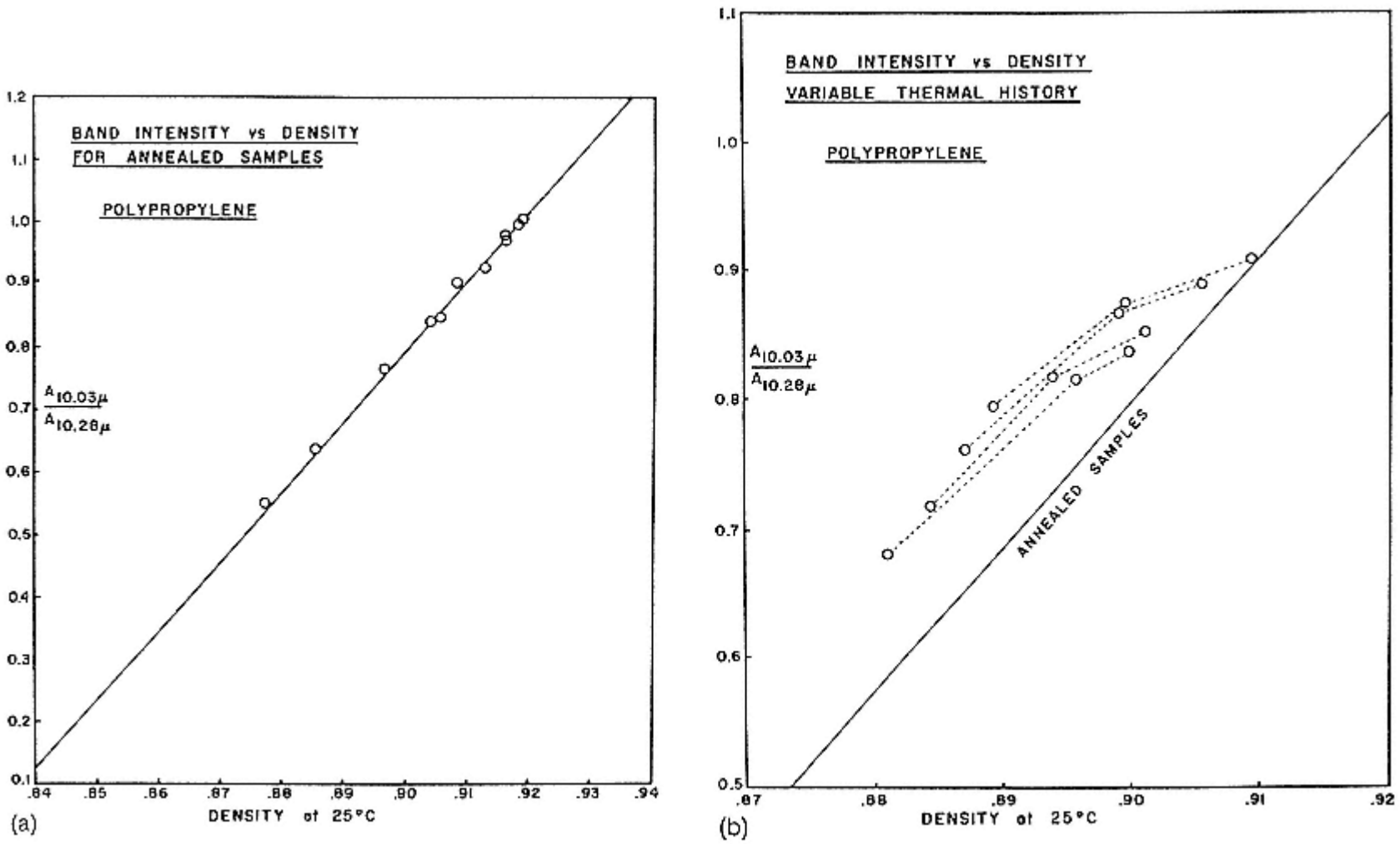

Figure 45
Plot of *A*(1003)/*A*(1028) versus density for (a) annealed samples of PP and (b) quenched samples as they are annealed.
(From Ref. 83.)

band can be used as an internal thickness band. As shown in Fig. 45a, a plot of *A*(1003)/*A*(1028) versus crystallinity as measured by density, for slowly cooled samples, gives a linear plot, suggesting its use; presumably one could characterize the sum of the α and β form crystalline phases. However, as shown in Fig. 46, a quenched and a slowly cooled PP sample have nearly the same IR scans, whereas the x-ray patterns differ drastically. Figure 45b shows the changes in the *A* (1003)/*A*(1028) ratio versus density as the quenched samples are annealed; they

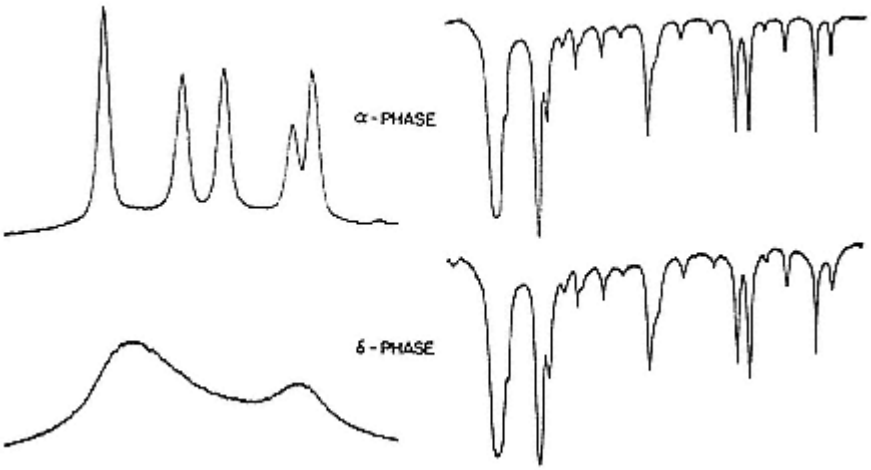

Figure 46
X-ray and IR scans of annealed (upper) and quenched (lower) samples of PP.
(From Ref. 83.)

approach the line obtained for the slowly cooled samples. The "problem" is attributed to the attempt to relate the 3/1 conformation to the degree of crystallinity; when PP is moderately quenched it "crystallizes" in the so-called smectic form [84]. Although details of the molecular packing are still being debated, it consists of domains of aligned 3/1 helical molecular segments. This short-range order is seen as "crystalline" by IR but nearly amorphous by x-ray (and somewhere in between by density and ΔH_f).

As Koenig points out [8], although crystal field splitting can be observed for PE (for the 720 methylene rock and 1460 cm^{-1} methylene bands), permitting their use for crystallinity measurements, IR is generally not suitable for other polymers. In PP it is the intramolecular helical splitting, not the intramolecular crystalline splitting, that is observed: "Unfortunately, the spectral results for PP are typical for most semicrystalline polymers. Generally the chains are simply too far apart and the intermolecular forces are so small that the crystal field splitting is not observed" [8]. As he suggests, and we, density is a simple, rapid, and cheap method of measuring crystallinity, while x-ray serves as the "final test."

All of the foregoing methods are based on the two-phase concept. In actuality, polymer crystals are expected to have a variety of defects and/or disorders. For instance, polyethylene single crystals grown from solution have a crystallinity, as measured by x-ray or density, of only 80%, with only part of the amorphous component being attributable to the folds [85]. Furthermore, in bulk crystallized polyethylene and other polymers a crystalline—amorphous interphase of varying

degrees of mobility is proposed, based, for example, on heat capacity, NMR, and x-ray measurements [78].

Hosemann has described one method of characterizing the possible disorder in crystalline regions (see Refs. 6, 39, and 86) (Fig. 47). Disorders of the first kind retain the long-range order of the lattice. However, either (1) the lattice points are statistically displaced small amounts from their proper positions (as in thermal vibrations), (2) there is a statistical distribution of up and down helices or helix hand, or (3) there is statistical substitutional disorder, as in random copolymers of like size units. In distortions of the second kind each lattice point varies statistically in position relative to its nearest neighbors; that is, there is short-range but not long-

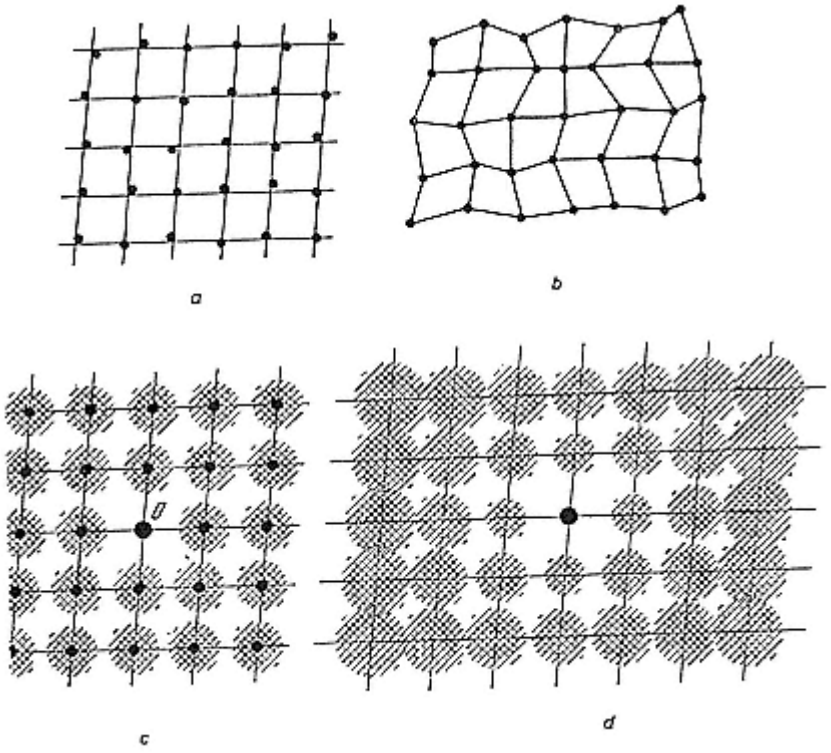

Figure 47
Disorders of the first (a) and second (b) kind; (c) and (d) represent the distribution functions (average positions of the atoms relative to any center) for (a) and (b). The disorder in (a) could also involve a statistical distribution of up and down or right- and left-handed helices, or of a substitutionally disordered lattice of equal size units; (b) would result if the substitutional units have a different size [as in random P(ONA)p(OBA) copolymer]. (From Ref. 40.)

range order. This can occur in random copolymers of unlike size units. The effects of these disorders on the diffraction patterns (in x-ray diffraction and ED) is described in Table 5. From the decrease in intensity of increasing order of a given reflection and the broadening (of all reflections if due to size, or of increasing orders if due to distortions of the second kind) the degree of disorder can be Characterized. The statistical and substitutional disorders result in diffuse scattering (streaks if x-ray fiber or ED single crystal patterns are observed, as in Figure 37). The presence of the disorders clearly complicates the measurement of the crystallinity. The thermal vibrations, for example, subtract intensity from the crystalline peaks and add it to the diffuse background, suggesting an increase in amorphous content. If the crystals are small enough (<10 repeat distances, i.e., ~50 Å), the breadth of the reflections may be so large they are difficult to distinguish from amorphous scattering; this is one interpretation of the scattering from the "smectic" PP.

Table 5 Types of X-ray Scattering by Various Types of Crystals.

System	Diffraction	Diffuse Scattering
Ideal crystals without disorder	Sharp	None
Distortions of the first kind		
Statistical disorder and substitution type	Sharp	$N(\langle f^2\rangle - \langle f\rangle^2)$. continuous, gradually varying
Frozen-in thermal vibration type	Sharp, decrease in I with θ	$N\langle f\rangle^2 (1-D^2)$, yields temperature diffuse scatter, increasing background with θ
Effect of crystallite size	Broadened equally for all orders of given reflection, inverse to N in the lattice direction	same as above if present
Distortions of the second kind	Broadened increasingly with θ, proportional to degree of disorder in lattice direction	same as above if present

Note: f = structure factor for unit cell; $\langle f^2\rangle$ = mean square value, perfect or imperfect; D = Debye factor = exp $(-8\pi^2 \langle \mu^2\rangle \sin^2\theta/\lambda^2)$ with $\langle \mu^2 \rangle$ = mean square amplitude of vibration (of atoms); and N = number of unit cells (in given lattice direction).
Source: Modified from Ref. 6.

Ruland [87], with modifications by Vonk to permit easier calculation using a computer [88], developed a method to characterize both the crystallinity and the degrees of both types of disorder. As described in Ref. 39e, in particular, it involves separation of the incoherent background scattering and the amorphous scattering from the crystalline scattering, for various increasing ranges of 2θ. Comparison of the integrated crystalline scattering, corrected by adjustable terms characterizing the two types of disorder, to the total integrated intensity should be a constant, the degree of crystallinity, regardless of the range of angles chosen. Thus both crystallinity and disorder can be obtained. An example, for PP, is shown in Figure 48 and Table 6.

2—
Orientation

Characterization of the degree and type of orientation, of particular concern in fibers and films but also of interest in, for example, injection-molded (in which variations through the thickness and with distance from the gate affect the properties) and extruded objects, is relatively straightforward for the molecular seg-

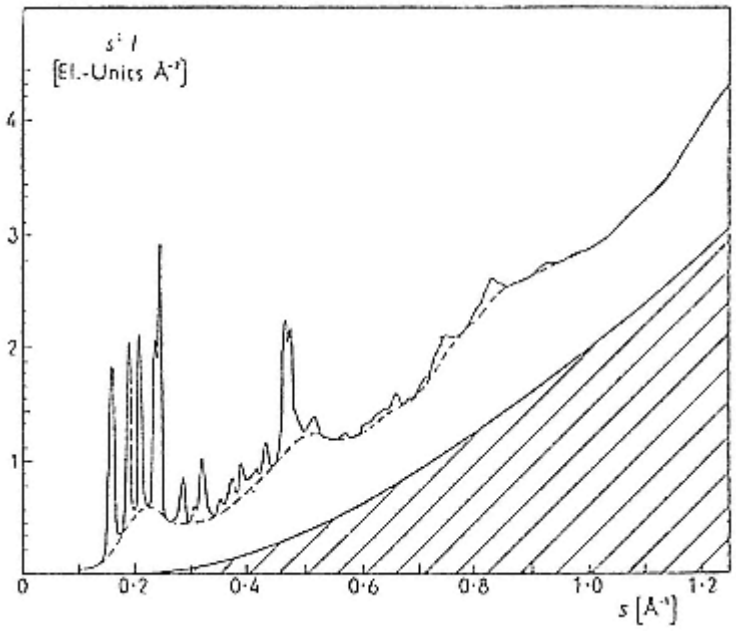

Figure 48
Plot of Is^2 versus s ($s = 2 \sin \theta/\lambda$) for a quenched sample of PP annealed 30 rain at 160°C. The rise at large angles is due to the multiplication by s^2. The shaded area is the incoherent scattering. (From Ref. 87a.)

Table 6 Crystallinity of PP Samples as a Function of k (Disorder Factor) and Range of Angles of Integration

	Polypropylene							
Interval	Sample 1		Sample 2		Sample 3		Sample 4	
$s_o - s_p$	$k = 0$	$k = 4$	$k = 0$	$k = 4$	$k = 0$	$k = 4$	$k = 0$	$k = 4$
0.1–0.3	0.270	0.329	0.353	0.431	0.546	0.666	0.120	0.146
0.1–0.6	0.159	0.294	0.222	0.411	0.333	0.616	0.078	0.144
0.1–0.9	0.105	0.305	0.145	0.421	0.220	0.638	0.044	0.128
0.1–1.25	0.067	0.315	0.095	0.447	0.145	0.682	0.029	0.136
xcr		0.31		0.43		0.65		0.14

Note: For all samples a value of $k = 4$ gives the "same" crystallinity regardless of the range of integration. Since all k are identical regardless of thermal history, it is assumed k is due to thermal vibrations; disorders of the second kind would be expected to vary with thermal history.
Source: Ref. 87a.

ments in the crystalline regions but is more complex if crystalline and amorphous orientation is desired. Yet the latter may significantly affect the properties. For measurements of the orientation of crystalline segments, x-ray diffraction is the primary technique, with IR dichroism also appropriate. The latter is particularly applicable for determining, separately and jointly, the crystalline and amorphous orientation if either absorption bands due to both conformations can be separately identified (as for the trans and gauche PET bands described earlier, with the caveat that some of the trans conformers are in the amorphous regions) or by subtraction if only a crystalline band can be isolated (see later discussion). Birefringence is also used for characterizing overall orientation, with amorphous orientation being obtainable by subtraction of crystalline orientation obtained by another technique.

Fibers are the simplest systems for which to characterize orientation. In general, they have cylindrical symmetry about the fiber axis, for both the crystalline and amorphous regions. On the other hand there may be a skin—core effect, depending on the method of preparation and diameter, in which there is either a skin of different degree of orientation than the core, or a gradation of orientation from surface to center. Ignoring the latter effects, a relatively simple method to obtain an indication of the degree of crystalline orientation is to take a flat-plate or cylindrical film x-ray pattern, the fiber (or bundle of co-aligned fibers) being oriented along the **z** axis (cylinder axis) of the film. Typical flat-plate WAXD photographs are shown in Figure 49 (in this case, however, of films). Desired would be an indication of the distribution of the molecular axes in the crystal, (**c**), at angles to the fiber axis, with this distribution presumably having cylindrical symmetry about the fiber axis. Although the 001 reflections, whose

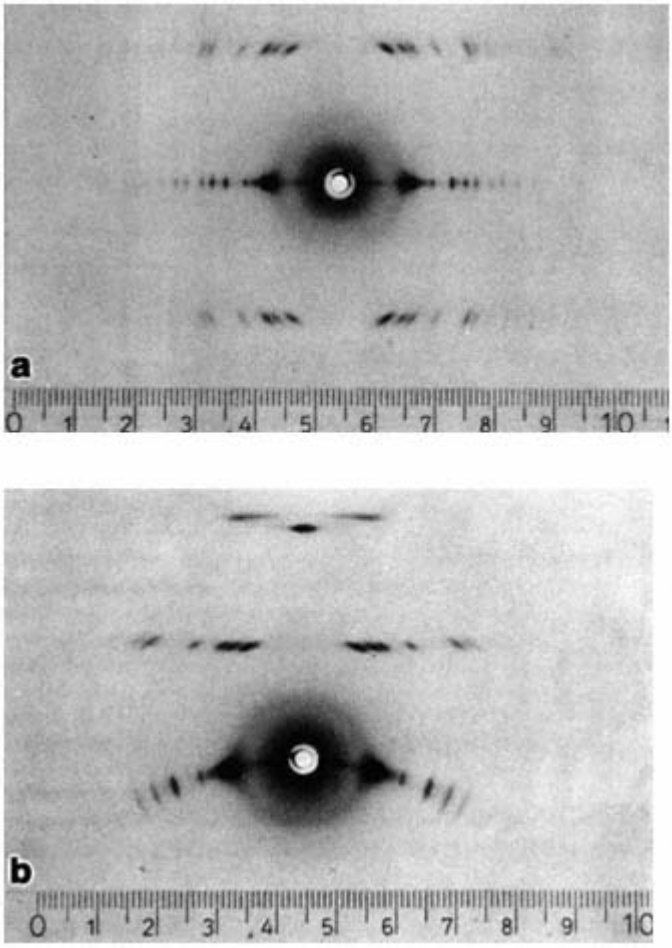

Figure 49
Cylindrical WAXD photographs of drawn samples of (a) PE, (b) PE tilted, (c) POM, (d) PTFE (15°C), (e) PP short exposure, and (f) PP long exposure.
(From Refs. 89 and 92b.)

azimuthal distribution would yield this information, after correction for the increase in circumference of rings about the fiber axis with increasing deviations from the axis,* are not on the pattern (the fiber needs to be tilted for 001 to inter-

*The sphere of reflection intersects a decreasing fraction of the "ring" corresponding to crystals aligned off axis as the angle of misalignment increases (see Reft. 39).

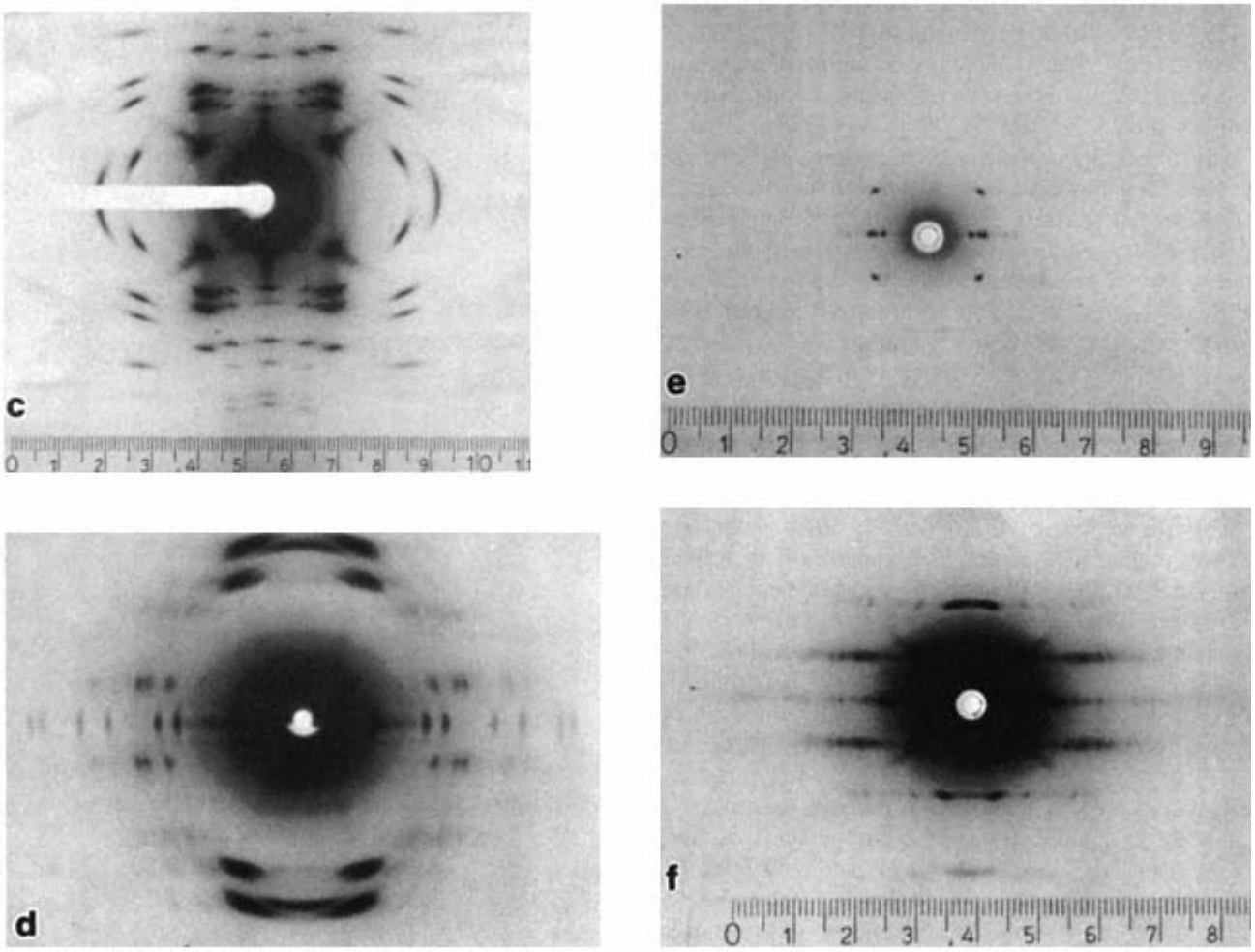

Figure 49
(continued)

sect Ewald's sphere), the same information can be obtained from the equatorial (hk0) reflections.

The degree of orientation can be expressed either in terms of the half (or full) width at half height of a microdensitometer azimuthal scan along one of the equatorial hk0 reflections (even for monoclinic ar triclinic cells since $\mathbf{a}^*$ and $\mathbf{b}^*$ are perpendicular to **c**) or in terms of Hermans' orientation function [90]

$$f = \frac{3(\cos^2 \phi) - 1}{2} \qquad (7)$$

where ϕ is the angle of deviation from perfect alignment (here c is parallel to the fiber axis and/or $\mathbf{a}^*$ and $\mathbf{b}^*$ perpendicular. For reasonable degrees of alignment the correction mentioned earlier is not needed and, with ϕ being the angle between $\mathbf{a}^*$ or $\mathbf{b}^*$ and the equator:

$$\langle \cos^2 \phi \rangle = \frac{\int_0^{2\pi} I(\mathrm{hk0}) \cos^2 \phi \, d\phi}{\int_0^{2\pi} I(\mathrm{hk0}) \, d\phi} \qquad (8)$$

For a "perfectly" oriented fiber, f would be 1 as defined here,* whereas it is 0 for random orientation and -1/2 for an orientation perpendicular to the fiber axis.

For more complex types of orientation, as found in drawn films of some samples (e.g., PET), biaxially oriented films, or the skins of injection molded objects, more complex x-ray methods should be used. The simplest again consists of WAXD photographs, this time three patterns with the beams in three mutually perpendicular (machine, transverse and thickness, as earlier) directions. An example for a drawn film of PET is shown in Figure 50a with the method of sample preparation shown in Figure 51b. [91]. If the film had cylindrical symmetry the transverse and thickness patterns should be identical while the machine direction pattern should consist of rings; the observed pattern is attributed to preferential alignment of the phenyl rings parallel to the surface, with the molecular axes, as expected, being aligned in the machine direction. A similar set of patterns is shown in Figure 50(b) for a "pushtruded" shot gun shell casing LPE sample (see Figure 51). The casing is produced by forcing an LPE tube over a mandrel at ~120°C, that is, below T_m.

As noted above, 001 (planes normal to **c**) reflections are not observed on flat plate photographs with the beam perpendicular to **c** (i.e., the draw direction in fibers), since the Ewald's sphere does not intersect their reciprocal lattice spots. Although they can be observed if the fiber is tilted, such patterns are not that useful for orientation measurements. Representations of the entire distribution of crystal unit cell axes can be obtained by using pole figures (or inverse pole figures) with details of the method given in standard texts [6,39e]. A pole figure is, in essence, a two-dimensional stereographic projection plot of the three-dimensional distribution of a given reciprocal lattice vector (e.g., for PE, $[200]^*$ (**a**), $[020]^*$ (**b**), or $[002]^*$ (**c**)). From two such plots (Figures 51c, d) one can obtain a visualization of the distribution of the unit cell axes. On the pole shown in Figures 51 a, b, the numbers indicate the number of counts detected per unit time when the sample is oriented that the normal (i.e., the pole, hence the name of the plot, and here the axis involved, **b** and **c**) to the plane being examined lies in the given direction. The Figures 51a, b show the raw date while for Figures 51c, d they have been smoothed and plotted as if a hemisphere was drawn about the sample, with the machine direction aligned E-W, the transverse direction aligned N-S, and

*We have defined Φ as the angle of deviation of the hk0 reflection from the equator; normally it is defined as the deviation of c from the meridian, in which case the equation becomes

$$(\cos^2 \phi_m) = \frac{\int_0^{2\pi} I(hkl) \cos^2\phi \sin\phi d\phi}{\int_0^{2\pi} I(hkl) \sin\phi d\phi} \qquad (9)$$

with sin Φ accounting for the corrections mentioned earlier. In this case, perfect alignment for [001] is 1, for an [hk0] it is 1/2 (see Refs. 39 and 90).

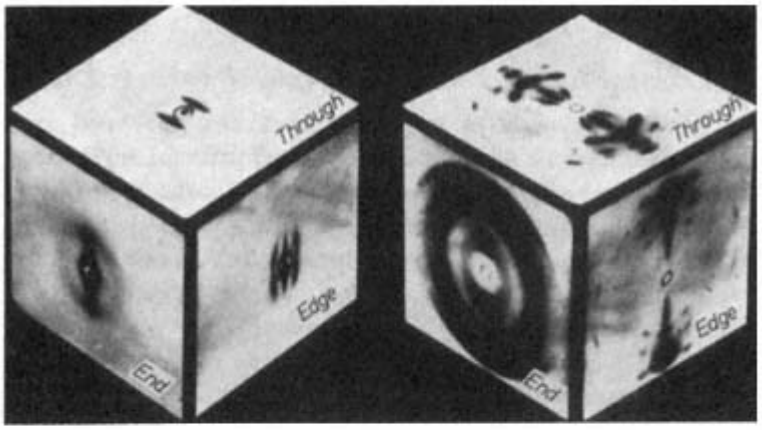

(a)

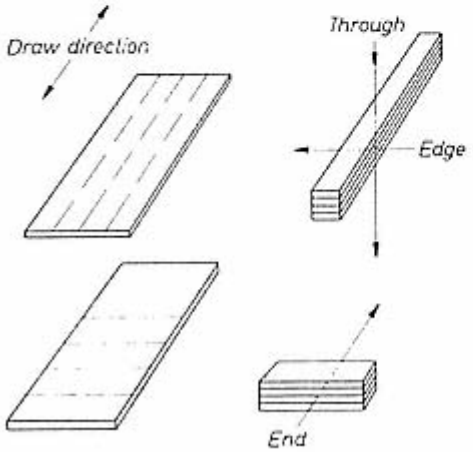

(b)

Figure 50
(a) Flat-plate SAXD and WAXD patterns of drawn films of PET with the beam in the thickness, transverse and draw direction. (b) Diagram of method of obtaining the patterns.
(From Ref. 91a.)
(c) Similar patterns of a pushtruded LPE sample.
(From Ref. 92.)

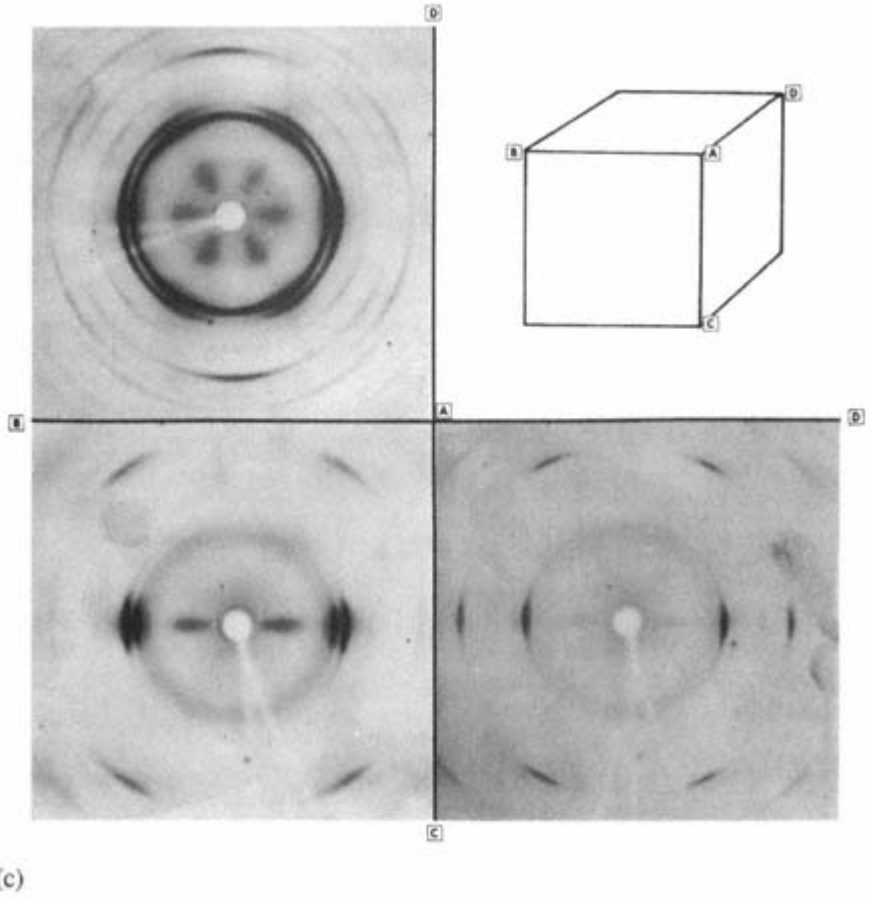

Figure 50
(continued)

the thickness direction in the center. Values of equal intensity are connected with "contour lines," as on a topographic map, to display (here) the unit cell axes' distribution (Fig. 51c, d) Note that the axes (MD, ND, and TD) have been rotated between Figures 51 a, b and c, d. These pole figures (with [110] and [200] also being obtained) were interpreted as indicating an alignment oft in the machine direction, indicated by the high concentration of (002) poles at the E and W poles. In combination with SAXS patterns taken with the beam at various angles to the sample (Figure 51e), they were interpreted in terms of lamellae oriented as in Figure 51f. The difference in the two-point SAXS spacings with beam orientation agrees with the lamellar tilt suggested. With chain folding in LPE occurring on 110 and 200 planes, the fold planes align in the transverse direction (Figure 51g) and prevent

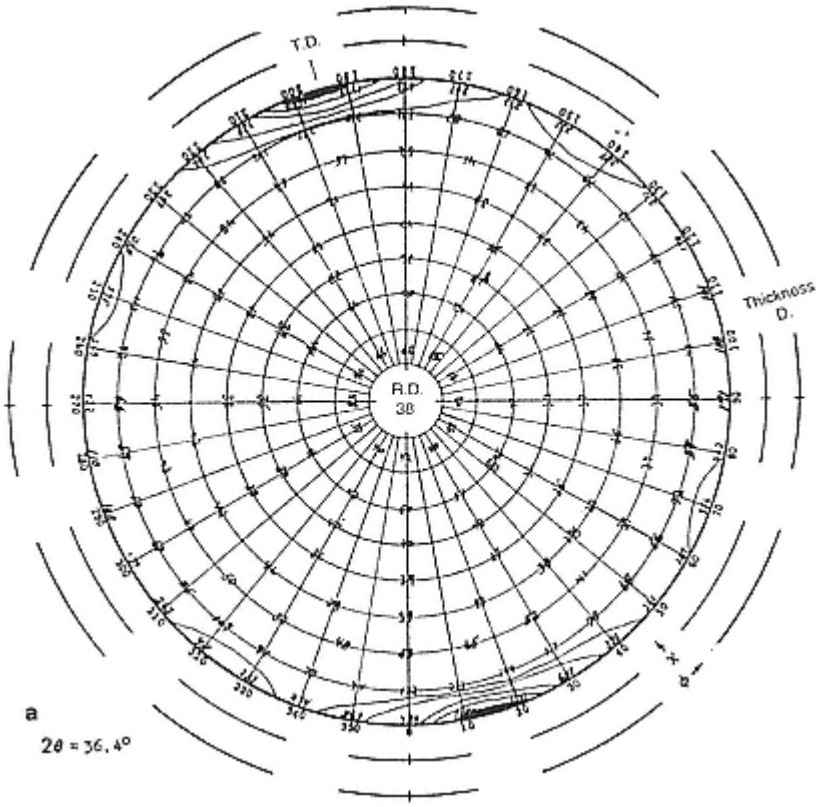

Figure 51
(a,c) 020 and (b,d) 002 pole figures for drawn, rolled LPE. The raw data are shown in (a) and (b), with contour lines shown in (c) and (d). Sample directions: R.D., roll direction; T.D., transverse direction; and Th.D., thickness direction. Usually a Wolff plot projection would be used rather than that shown here. SAXS patterns obtained with the beam oriented at various directions to the sample are diagrammed in (e), with a two-point pattern being seen with the beam normal to the sample and a four-point pattern with the beam in the transverse direction. The proposed model (f) has a roof-like arrangement of the lamellae, with the chain axes in the machine direction and the ridge of the roof in the transverse direction. The fold planes (110 and 200) are aligned in the transverse direction, parallel to the surface (g).
(From Refs. 92a,b.)

the axial splitting often seen in highly drawn films. This orientation also leaves the close-packed 110 and 200 planes parallel to the surface. Pole figures for fibers having cylindrical symmetry (Figure 51a,b) would consist of uniform bands of intensity on the equator (outer ring) for $[hk0]^*$ directions, for example, $[200]^*$ (**a*** or a), $[110]^*$ or $[020]^*$ (**b*** or **b**) for PE, the azimuthal breadth along the lines of longitude (radial lines in Figures 51a,b) being directly related to the half width, half height

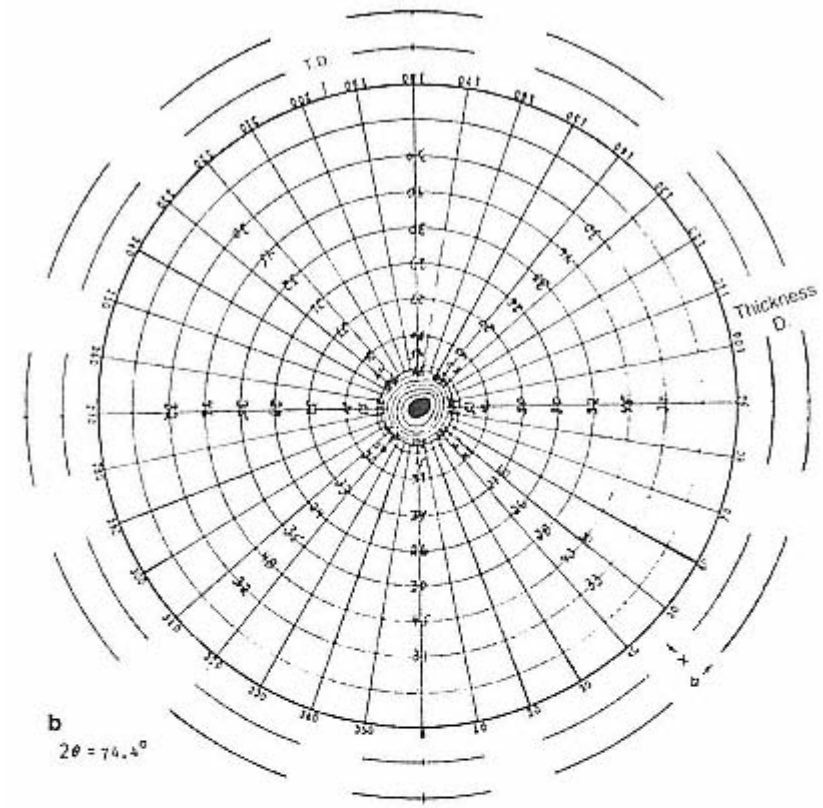
T.D.
Thickness
D
b
2θ = 74.4°

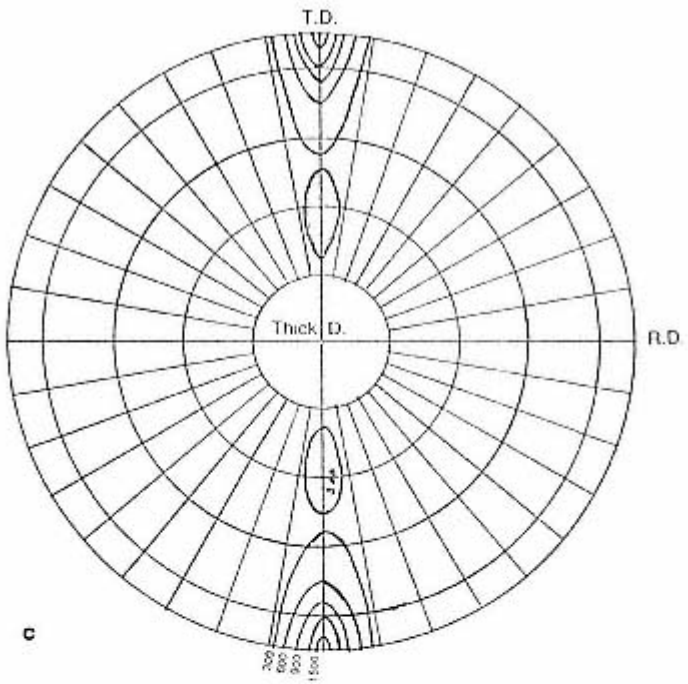
T.D.
Thick. D.
R.D.
c

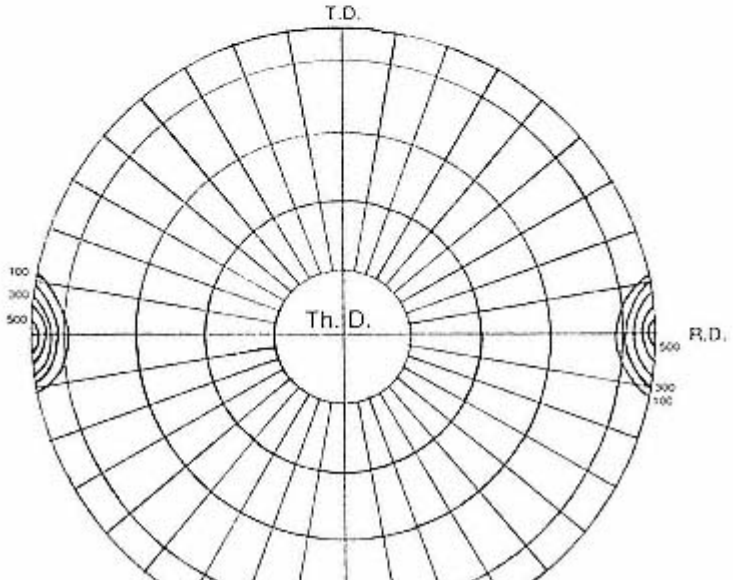
T.D.
Th. D.
R.D.

Figure 51
(continued)

value of Hermans' *f* cited earlier, while $[001]^*$ (**c**)* would either be a "spot" at the center (N pole) (as in Figure 51b) for orthorhombic, tetragonal, and hexagonal cells, or a ring of some breadth about this direction for monoclinic and triclinic cells.

3—
Amorphous (and Overall) Orientation

One of the simplest ways to measure overall orientation (if the crystal orientation is known, "subtraction" permits determination also of the "amorphous orientation") is to determine the change in dimensions as a sample is permitted to freely relax while being heated [93, 94]. We have found that free relaxation can be permitted by using a liquid stable to suitably high temperature and noninteracting with the polymer, with the method being useful for both fibers and more complex types of orientation. Figure 52 is an example for a cross section of two types of PE pipes heated on a dish of glycerin; the preferential orientation of the external skin in one type of pipe (externally cooled)versus skins on both surfaces (cooling inside also) results in the differences in the shrinkage.

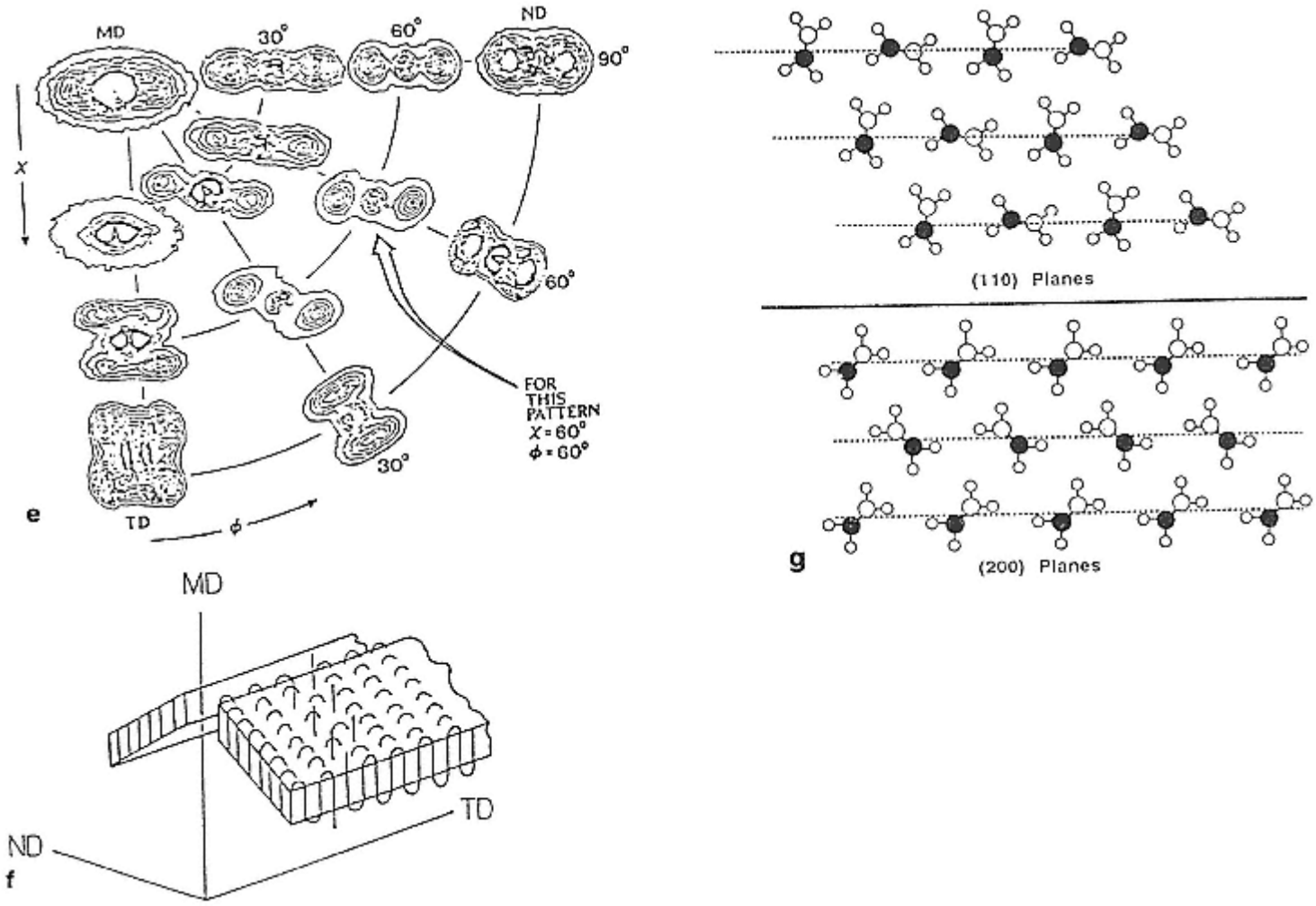

Figure 51
(continued)

Birefringence (Δn), as measured in a polarizing microscope using either a compensator or the Becke line method using immersion oils of varying index of refraction [95], is another relatively simple method of determining the overall orientation of a sample. Letting $n_y = n_z - n_x$, where n_x and n_z are the

indices of refraction in the **x** and **z** (fiber axis) direction, for light propagating in the y direction, Hermans f_{cz} (for the angle between **c** and **z**) is given by

$$f_{cz} = \frac{\Delta n_y}{\Delta n_y^\circ} \tag{10}$$

where Δn_y° is the maximum possible birefringence, that is, all chains perfectly aligned. For semicrystalline polymers of crystallinity fraction Ψ

$$\Delta n_y = \psi\, \Delta n_y(c) + (1 - \psi)\, \Delta ny\,(a) + \Delta n_y(f)$$
$$= \psi f_{cz}(c)\, \Delta n_y^\circ(c) + (1 - \psi)\, f_{cz}(a)\, \Delta n_y^\circ(a) + \Delta n_y(f) \qquad (11)$$

where $\Delta n_y(c)$, $\Delta n_y(a)$ are the Δn for the crystalline and amorphous regions in the fiber, $\Delta n_y^\circ(c)$, $\Delta n_y^\circ(a)$ are the values for completely oriented crystalline and amorphous regions, and $f_{cz}(c)$ and $f_{cz}(a)$ are the respective Hermans f and Δn_y(f) a small contribution from form birefringence. Furthermore, $\Delta n_y^\circ(c)$ and $\Delta n_y^\circ(a)$ differ only due to differences in density, that is $\Delta n_y^\circ(c) = p_c/p_a \cdot \Delta n_y^\circ(a)$. Thus either the overall orientation or, if $f_{cz}(c)$ is known from x-ray diffraction (it would equal the f described above), $f_{cz}(a)$ can be determined. The latter, on which the modulus of fibers is strongly dependent, is usually less than $f_{cz}(c)$, but approaches it in the extended chain fibers of PE [96]. Values of $f_{cz}(c)$ up to 0.999 and $f_{cz}(a)$ have been obtained [96a]. For x-ray methods of determining $f_{cz}(a)$ see Ref. 96b.

Infrared dichroism is another, related method of determining f_{cz} and, if $f_{cz}(c)$ is known, $f_{cz}(a)$. From knowledge of the orientation of the transition moment (direction of dipole oscillation) of the IR vibration (or polarization direction for polarized Raman scattering) relative to the chain axis, measurements of the absorption intensity with parallel (to the fiber axis) and perpendicularly polarized

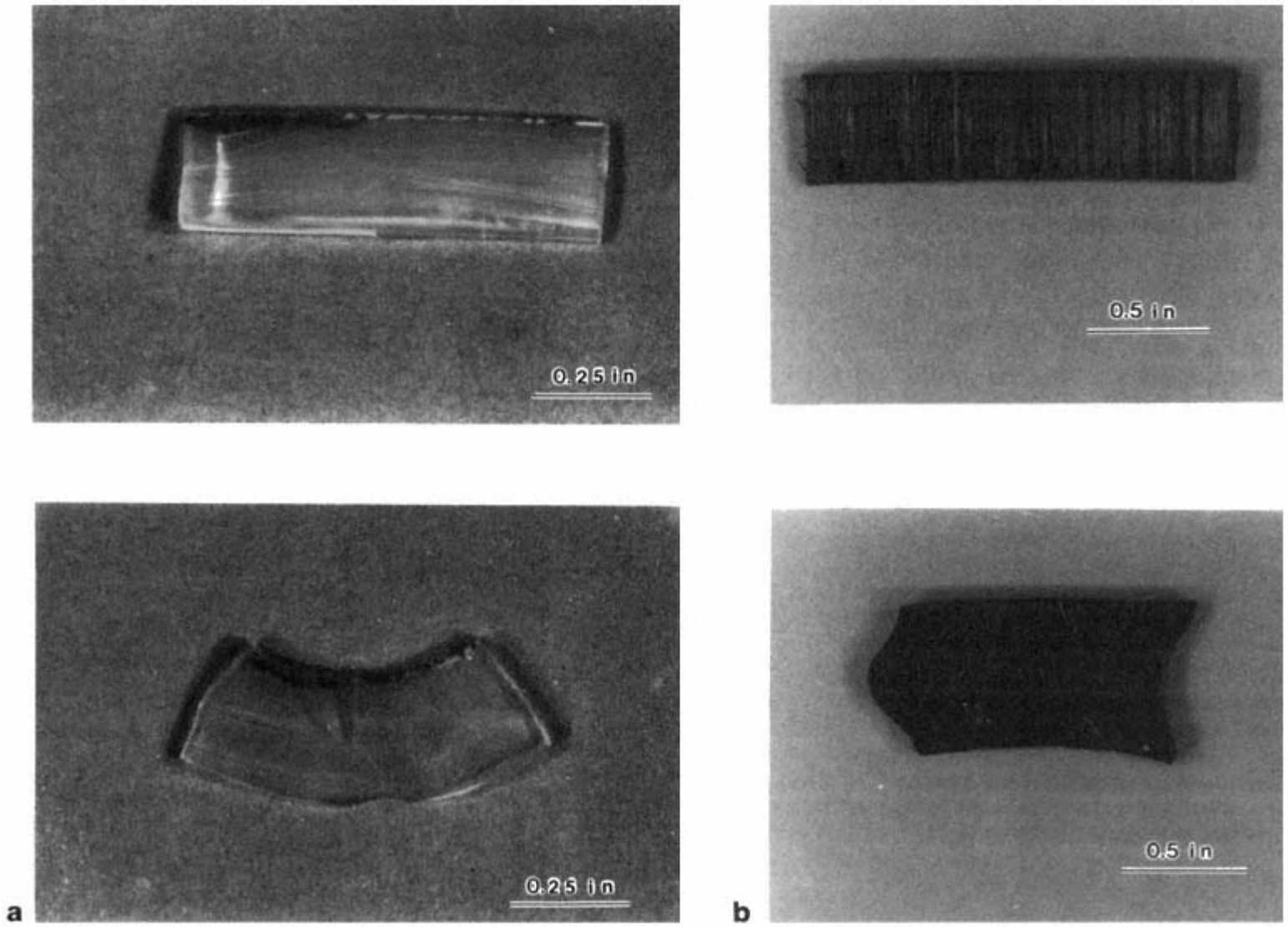

Figure 52
Longitudinal sections of extruded LLDPE pipes originally cooled (a) on the external surface

only and (b) on both surfaces, before (top) and after (bottom) heating to T_m on a glycerine surface. The external surface is upper in each photograph.
(From Ref. 93.)

incident IR give the dichroism R = $R = A_\parallel/A_\perp$ which can be used by itself, or converted to Hermans' *f*:

$$f = \frac{(R - 1)(R_0 + 2)}{(R + 2)(R_0 - 1)} \qquad (12)$$

where R is the experimentally measured dichroism ratio and R_o is the dichronic ratio for a perfectly uniaxially oriented sample. If the transition moment makes an angle ϕ with respect to the molecular axis, $R_o = {}^2 \cot^2 \phi$, with R_o varying from ∞ to 0 as ϕ varies from 0 to 90°. No dichroism ($R_o = 1$) is observed if ϕ = 54° 440´, the so-called magic angle (IR); for NMR the magic angle is 57.4° ($3 \cos^2 \phi' - 1 = 0$), with ϕ' being the angle between axis of rotation of the sample and the applied field H_0. Details of methods of determining ϕ and thus R_0 are given in texts (e.g., Refs. 6 and 8). Examples of transition moment directions relative to the chain axis for various IR bands and the use of the 1220 cm^{-1} band to determine f for PP films drawn to various draw ratios are shown in Table 7 [97],

A major advantage of the IR technique is its ability to detect and separate the orientation of the conformers in the amorphous regions from those in the crystalline regions, or of two components in blends or other multiphase systems, again, however, with the caveat that some fraction, for example, of the "crystalline" conformers (i.e., trans in PET) may actually be in the amorphous regions. Recent x-ray methods (described in Section II.A) have permitted separation of crystalline, intermediate and amorphous (assumed random) orientations [78].

Although not expected in fibers, nonaxially symmetric orientation is frequently found in uniaxially drawn films (e.g., PET, as shown in Fig. 50a), For such samples, as well as biaxial ly oriented films, injection molded objects, etc., the absorbance of the various IR bands in the three directions needs to be characterized. For this purpose *A*z, the absorbance in the third (thickness) direction, as well as A_y ($A_\parallel$) and A_x ($A_\perp$), need determining. From *A*z, obtained by sample tilting (see Ref. 8),

$$A_0 = \frac{A_x + A_y + A_z}{3} \qquad (13)$$

and the orientation parameters A_x/A_0, A_y/A_0 and A_z/A_0 can be determined. Figure 53 shows results for a PET film drawn to varying degrees. The conformer composition was determined by comparison with predicted spectra for pure trans and gauche conformers, with the separation into trans (crystalline)and trans (amorphous) similar to that described for Figure 22.

As indicated x-ray, birefringence, and IR are the most common techniques for characterizing orientation, with the three methods characterizing different aspects of the orientation, and with relaxation being an additional, even simpler technique. Electron and neutron (discussed later) diffraction yield results similar to x-ray, with ED restricted to specially prepared (thin) samples. Other, less used techniques include NMR [99], permitting determination of the orientation of mo-

Table 7 (a) Dichroic ratio (*R*), Orientation Function (*F*), and Average *c* Axis Orientation Angle (θ) for Drawn Films of PP of Various Draw Ratios Based on the Dichroic Ratio for the 1220 cm^{-1} Band at Band Angle 90° and (b) PP Bands and Their Vibration Direction (Transition Moment) Relative to the c Axis

(a)

Draw Ratio[a]	*R*	*F*	θ°
1	1.015	-0.010	55.1
1.5	0.745	0.186	
4	0.536	0.366	40.6
7	0.056	0.918	13.5
8	0.51	0.926	12.9
9	0.036	0.947	10.8

(b)

Frequency (ν)	α_ν°	Frequency (ν)	α_ν°
928 cm^{-1}	90°	1220 cm^{-1}	90°
973 cm^{-1}	18°	1256 cm^{-1}	0°
998 cm^{-1}	18°	1307 cm^{-1}	0°
1045 cm^{-1}	0°	1363 cm^{-1}	90°
1103 cm^{-1}	90°	1378 cm^{-1}	70°
1168 cm^{-1}	0°		

[a]The number shown is the ratio of the length of the drawn film to the initial length of the film.
Source: Ref. 97a and b.

bile segments (see Section III) and the use of fluorescent probes (e.g., Ref. 100). In the later case anisometric fluorescent molecules (e.g., dyes) are absorbed in the amorphous domains of the sample, before or after deformation, and their orientation is determined, for instance by polarized UV spectroscopy.

With increases in intensity of x-ray sources (rotating anodes and synchrotrons) and the development of FTIR (and FT-Raman) techniques, it has become possible to follow deformation and crystallization processes in real time. Modern FTIR instruments (as of 1993) permit obtaining and storing scans (interferograms) at rates up to nearly 100/sec, giving a time resolution approaching 10 msec. Although at low resolution, if the time frame of the phenomenon being examined is sufficiently long, (e.g., polymerization reactions, mechanical deformation, including dynamic mechanical spectroscopy, creep and stress relaxation, fatigue and crystallization; see, e.g., Ref. 8), single interferograms can be transformed into spectra essentially instantaneously to follow incremental Changes. Interpretation is as described elsewhere in this chapter.

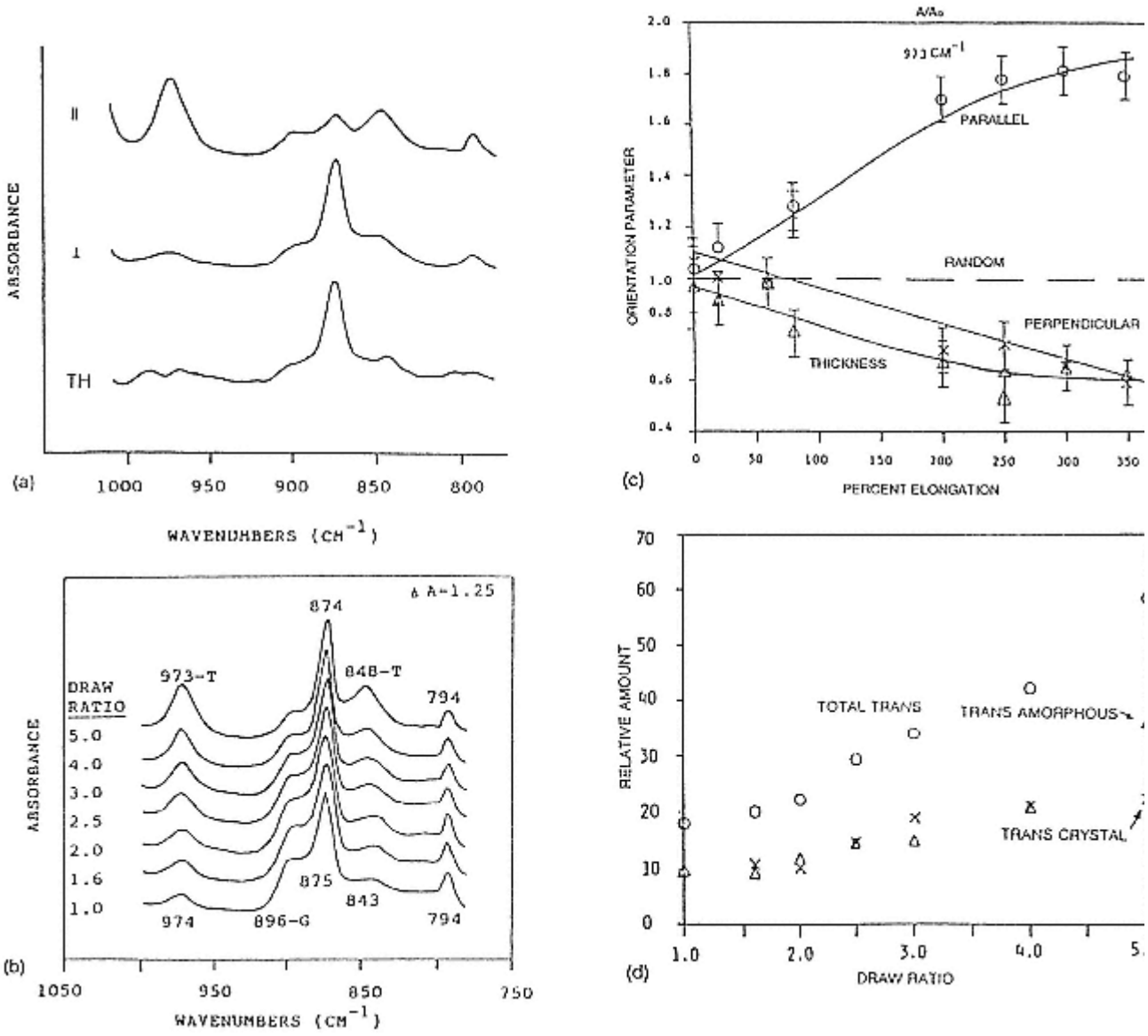

Figure 53

Effect of draw ratio on orientation of PET films. (a) Spectra of uniaxially drawn PET film with the beam polarized parallel and perpendicular to the draw direction and parallel to the thickness direction of the film. (b) Calculated isotropic spectra of uniaxially oriented PET as a function of draw ratio. The 973 and 848 cm^{-1} bands (trans) increase while the 896 (gauche) band decreases. (c) Orientation (trichroic) functions for the 973 cm^{-1} band as a function of percent elongation. Perfect parallel orientation has a value of 2. (d) Conformer composition (trans; total, crystalline, and amorphous) of drawn PET films.
(From Ref. 98.)

Rotating anode x-ray tubes, commercially available from several sources, are designed to permit dissipation of the heat induced by the electron-beam bombardment of the target generating the x-rays. Conventional sealed copper tubes, as often used, have a 1×10 mm focal spot (region from which x-rays are generated) and can be operated, typically, at 40 kV, 20 mA, with higher power being used in broad-focus (e.g., 2×10 mm) and lower in fine-focus (e.g., 0.4×8 mm) tubes. The fine focus, looked at on end from a slight angle, gives a high-brilliance "point" source, while the broad focus looked at normal to the long direction yields an intense line focus. With a normal focus sealed tube, a wide-angle flat-plate point-source pattern of a 3-mm-thick (near optimum for maximum intensity) PE sample takes 5–10 min at a sample-to-film distance of 5 cm; a small-angle pattern (see below) of the same sample at a 17-cm distance takes nearly a day. Typical, reasonable-cost rotating anodes operate at 60 kV, 100, 200, or 300 mA, that is, with up to nearly 30 times the power, with correspondingly increased intensity. These units have tubes with diameter on the order of 6 in, rotating at 6000 rpm. Even higher power tubes are available: Rigaku Denki Corp. produces a unit operating at 1.5 A, 60 kV, with the tube, 12 in. in diameter, rotating at 9000 rpm. For in-lab applications for such tasks as characterization of orientation and crystallization at various positions along a spin line, such systems are ideal. However, even sealed tubes can be used for such purposes, using longer exposures, since it is assumed the physical structure changes are stable as a function of distance from the spinneret, although obviously changing within the fiber as it moves away from the spinneret [101].

Synchrotron radiation is increasingly being used as a high-intensity source [102]. The advantages are [39e]:

1. A continuous spectrum from in-frared ($\lambda \approx 10^{-2}$ mm) to hard x-rays ($\lambda \approx 0.1$ Å).

2. High inherent collimation of the beam (0.1 mradian in the x-ray λ, region).

3. A source intensity and brightness, due in part to the high collimation, several orders of magnitude higher than the largest rotating anode sources.

4. If desired, short (~100 psec) pulses with a frequency of a few nanoseconds.

5. Highly polarized radiation.

Applications have been made to crystallization and annealing (e.g., unorienter PET [103]) and to phase separation in blends and block copolymers, using small-angle x-ray diffraction (discussed later), and to crystallization, melting, and phase transitions, using wide-angle diffraction for a number of polymers (e.g., PP [104] and polyesters [105]). The latter includes simultaneous wide- and smallangle x-ray scattering and light scattering. General reviews are given in Ref. 102, as well as Ref. 39e.

Further enhancement of the rates of detection of x-ray scattering has come through the development of linear and two-dimensional position-sensitive detec-

tors (PSDs) [39e]. These detectors permit scattering angle detection of x-rays scattered over a broad angular range simultaneously (as on film) but with the advantages of counter detection and pulse height (λ) discrimination. Solid-state linear PSDs as well as Vidicon tube two-dimensional detectors are more recent advances, enhancing the range of intensity (solid state, but at the expense of λ discrimination, which, however, is not as important for synchrotron radiation) and the resolution (~300 μm as compared to 1 mm for the two-dimensional PSD).

C— Domain Size, Shape, Organization, and Interaction

The subject of this section is generally called polymer morphology, that is, the external structure of the physical entities making up the sample. In Section II.A we discussed characterization of the internal physical structure of crystalline domains, that is, the unit cell and defect-disorder structure, while Section II.B described characterization of their relative amount and orientation. Pertinent to this section is the discussion there of crystal size effects, that is, x-ray (or electron) diffraction line (or spot) broadening. As shown there, the size of the reciprocal lattice spots is inversely related to the size of the corresponding crystal, with the width of observed reflections being the result of these spots, for one or more crystals, being sampled by Ewald's sphere of reflection. Unfortunately, for crystal size characterization, disorders of the second kind (but not the first) also broaden the reflections, with separation of the two effects normally requiting measurement of the breadth of at least two orders of the reflections from planes normal to the crystal dimension being probed. For instance, 002 and 004 are needed for determination of crystal size in the c axis direction of PE, with even 002 being of low intensity on diffractometer scans and absent on flat-plate photographs from fibers. For fibers, however, x-ray line broadening remains the most appropriate technique, with tilting of the fibers being used when necessary. Note, however, that the x-ray line broadening technique yields the size of the crystal, not the crystal—crystal spacing.

The basic physical structural units for polymers generally have at least one dimension on the order of 100 Å; this includes the thickness of lamellar crystals and all dimensions of fringed micelle-like crystals, fibril diameters, radii of gyration of random coils in amorphous polymers (glass and melt), and domain sizes in block copolymers. For structure on this size scale, small-angle (x-ray and neutron) Scattering and transmission electron microscopy are the traditional techniques.

If the domain structure results in a difference in electron density, small-angle x-ray scattering (SAXS) can be used. Chapter 7 of the recent x-ray text by Balta-Calleja and Vonk [39e] gives an excellent description of its application to polymer morphology characterization. The requirement of measuring close to zero scattering angle (for CuKα) radiation, as normally used, a 100-Å periodicity gives a Bragg peak at 0.88° 2θ) requires that a highly collimated beam be used, necessi-

tating long exposures and/or the use of high-intensity sources and, for fibers, the newer two-dimensional detectors.

Descriptions of the applications (and methods of data interpretation) of SAXS to determination of the specific surface, width of the phase boundary, and radii of gyration of domains of one phase dispersed randomly or regularly in another phase are given in Ref. 39e. If the domains are periodically arranged, as the lamellae in crystalline polymers or the domains in some block copolymers, Bragg's law ($n\lambda = 2d \sin \theta$) can be applied to the peaks observed in the diffraction patterns (after appropriate corrections) to yield domain spacing. For dilute systems of particles, Guinier's law [106] can be applied:

$$i(\theta) = \frac{Nm^2}{V} e^{-16\pi^2\theta^2 R_g^2/3\lambda^2} \qquad (14)$$

where m is the number of excess electrons per particle over that in the matrix (+ or -), N is the number of particles in the illuminated volume V, and R_g is the radius of gyration, defined by

$$R_g^2 = \frac{1}{m}\int \nu' r^2 \, dm \qquad (15)$$

ν' being the volume of the particle. From plots of $i(\theta)$ versus θ^2 both R_g^2 (from the slope) and Nm^2/V (intercept) can be obtained. From knowledge of the composition and chemical structure Nm/V can be determined, permitting determination of m, a quantity directly related to the mass of the domain. R_g^2, on the other hand, can be related to the overall size and shape of the domain. Both of these measurements are often used for biological systems, for instance globular proteins and viruses in suspension, with relative values of R_g^2 for various shape particles being given in standard SAXS texts [106].

Representative schematic SAXS patterns from fibers are shown in Figure 54. Two-point and four-point patterns, elongated into streaks parallel to the meridian, equator, or at angles, are seen, often with diffuse scatter (as in Fig. 54k) superimposed on the center of the pattern. Similar patterns are obtained from uniaxially drawn films, with three-dimensional flat-plate patterns again being needed if the films do not have cylindrical symmetry (Figure 50).

The central streak is often interpreted in terms of voids; if the voids are elongated along the fiber axis (e.g., between fibrils), the streak is elongated (by the reciprocal relationship) along the equator. Such a streak may also be related to the crystalline—amorphous morphology (but a fibrillar morphology, densely packed, would not yield the streaks), with the presence of voids being confirmed by either the presence of light scattering (opaqueness not due to fillers) or loss of the SAXS scattering when the fiber is soaked in a liquid of electron density similar to that of the fiber. Compression of the fibers normal to their axes can also reduce void scatter.

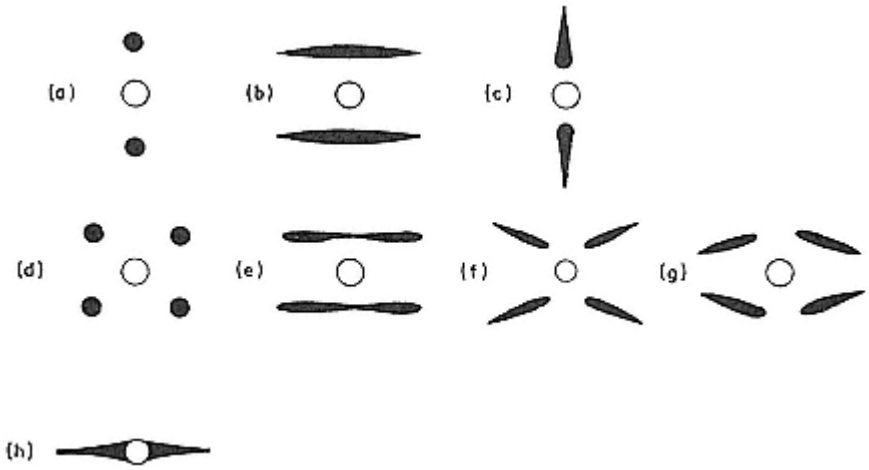

Figure 54
Schematic diagrams of various types of SAXD fiber patterns; the fiber direction is vertical, with (a—c) two-point patterns, (d—g) 4 point patterns, and (h) an equatorial streak.
(From Ref. 39e.)

The two-point and four-point patterns (as well as the central streak) often undergo significant changes during annealing. Annealing taut, as in heat setting, usually leads to a perfecting (increase in crystallinity as shown by WAXD, sharpening of the SAXS pattern and decrease in the scattering angles of the maxima) of the morphology. (Reference 107 discusses applications of SAXS to fibers.) Annealing relaxed, on the other hand, can lead to major changes in the form of the pattern, with the fiber often losing nearly all of its original draw (the basis of the previously described shrinkage measurements of the degree of orientation).

The various patterns in Figure 54 are usually described in terms of morphological models, with, unfortunately, different models sometimes leading to the same type of pattern. This is representative of a feature of all diffraction patterns; while disagreement between the pattern calculated for a model and that observed indicates the model is incorrect, agreement does not indicate the model is correct; a different model may also lead to a similar pattern.

Interpretation of the two- and four-point patterns has been made based on both continuous lamellar structures (more or less normal to the fiber axis; e.g., Figure 55) and a microfibrillar structure based on either a fringed micellar model (Figure 56a) or a paracrystalline fibrillar model (Figure 56b). Bonart and Hosemann's model (Figure 55) can explain the patterns in Figure 54a, b with the width of the streak being related to the curvature of the lamellae and the meridional spacing being related to the center-to-center distance (periodicity) of the lamellae. As shown later, there is reasonable electron microscope evidence for this type of structure.

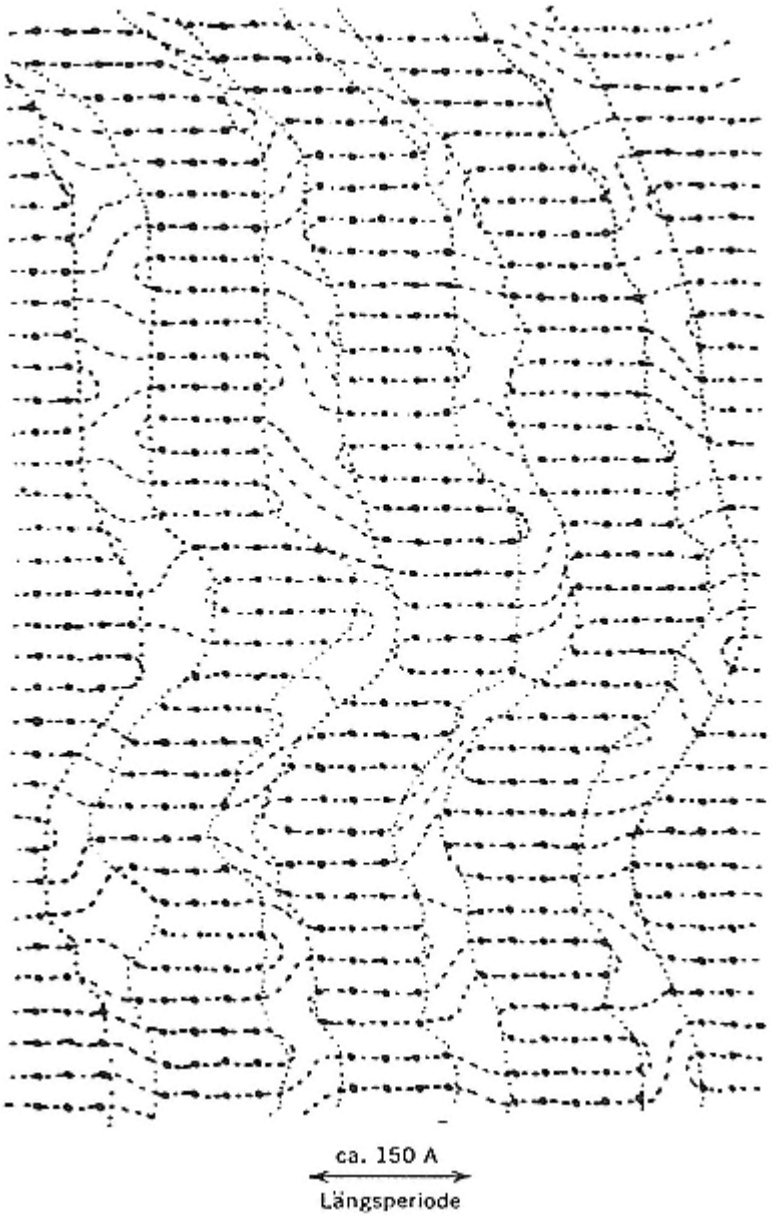

Figure 55
Bonart and Hosemann's model for the arrangement of the molecular segments and the lamellae in an as-drawn fiber or film.
(From Ref. 108.)

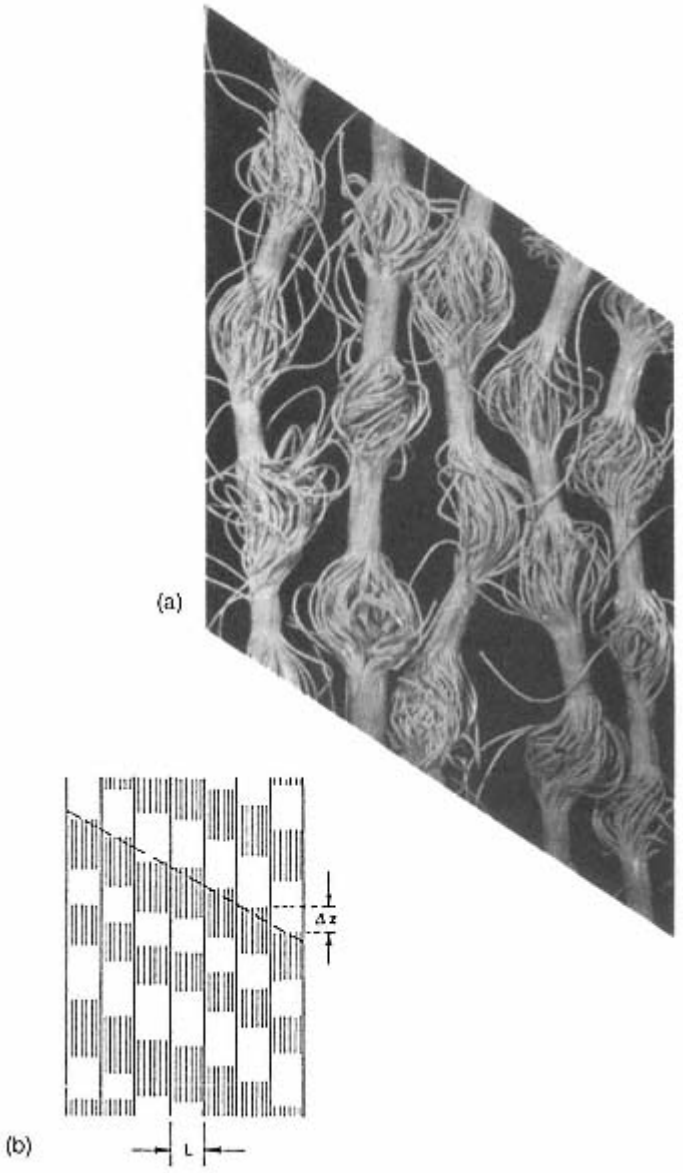

Figure 56
Paracrystalline (for lamellae) fibril models as proposed by (a) Statton [109] and (b) Hosemann [110] that would yield four-point patterns.
(From Refs. 109 and 110.)

Annealing taut leads to a perfecting (decrease in curvature) of the lamellae, increase in spacing (sometimes interpreted in terms of thinner lamellae melting, segments adding to the thicker, resulting in a greater periodicity) and decrease in streak width. Interpretation of the four-point pattern in terms of this type of model requires a preferred tilt angle for the lamellae. In the models in Figure 56 the four-point patterns are explained in terms of axial shift of neighboring crystalline domains in the fibrils. In those models the broadening normal to the fiber axis, as in Figure 54e, is due to the narrow diameter of the fibrils. Further details can be found in Ref. 39e and references therein. The central streak, often found in association with one of the other patterns, is usually attributed to voids elongated parallel to the fiber axis. Other methods of characterization of the void (pore) structure in fibers are discussed in Chapters 7 and 8.

Considering the dimensions of the morphological features of a fiber, transmission electron microscopy (TEM) would be expected to be an ideal technique. Unfortunately, sample preparation problems (with thicknesses of less than 1000 Å required for normal TEM) have greatly restricted its use. Typical fibers are even too thick for application of high-voltage microscopy; furthermore, the micrographs are always projections of the density of the sample through its entire thickness. Standard techniques for preparing thin samples from typical commercial fibers include surface stripping [111], sections cut by ultramicrotome from embedded samples, and replicas of etched samples (for descriptions of TEM polymer sample preparation techniques see Ref. 112); examples of their application to drawn films are given in Figures 57–62. Direct imaging of the fiber surface, by replication, would not be expected to be informative, as the surface is affected by the process of spinning. Etchants (using, for instance, ions or $KMnO_4$—H_3PO_4) chosen to attack amorphous regions in preference to crystalline regions might be expected to reveal the morphology (Figure 58). However, because of their diameter, fibrils are difficult to replicate. Only two-stage (reduced resolution) replicas are possible. Annealing alone can also "generate" a visible morphology (Figure 58a, 59).

The use of cut or stripped sections, or drawn thin films, permits the use of dark-field (imaging of the electrons diffracted into one or more ED reflections) and phase-contrast microscopy (see Ref. 61). As shown in Figure 60, the crystals (here lamellae) are imaged (see also Figure 41). These micrographs can readily be interpreted in terms of Bonart and Hosemann model (Fig. 56). If drawn normal to the original draw direction the films readily break down into fibrils, with, I suggest, the separate fibrils resulting from deformation of initial individual lamellae. The crystals in neighboring fibrils coalesce into the lamellae, with the lateral order perfecting during annealing. The retention (or regeneration by localized melting—recrystallization at the microneck edges) of folds is shown by the result of further draw (Figure 61), with even the annealed samples breaking down into fibrils under the action of lateral stresses. Tie molecules between the original

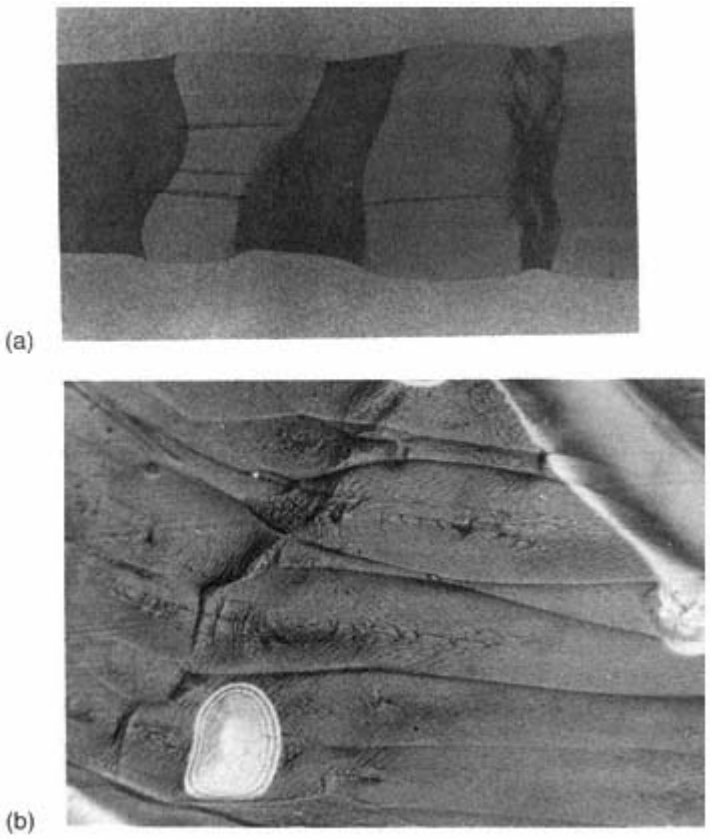

Figure 57
(a) Photograph of a partially drawn LPE film. The drawn regions are opaque due to the development of voids. Shear bands are seen at the right as a neck develops. (b) Optical micrograph (reflected light) of the necking zone of an LPE fiber originally crystallized with a free surface. (From Ref. 89.) (c) TEM micrograph of a microneckat a POM spherulite boundary. (From Ref. 113.)

lamellae, in bulk samples, are proposed to form intrafibrillar links in the drawn samples. This breakdown into fibrils is particularly obvious in simultaneously or uniformly biaxially drawn samples (Figure 62).

As indicated by the preceding micrographs, the use of thin films to study the morphology of uniaxially drawn polymers is much simpler than the corresponding study of fibers. While the observed morphology is believed similar to that in the fibrils, caution in extrapolation is indicated.

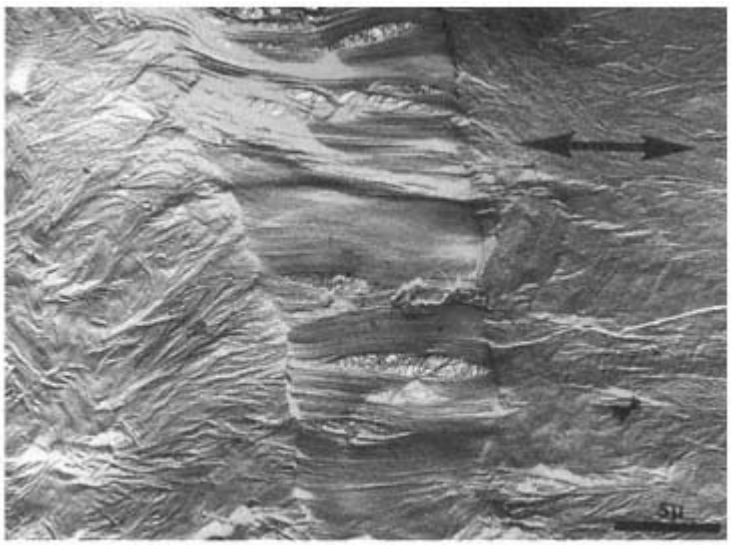

(c)

Figure 57
(continued)

TEM is also the method of choice for observing the organization of the crystalline lamellae in unoriented samples and of the domains in block copolymers. In both cases, however, the need for thin samples and sufficient image contrast requires special preparation techniques. Etching, sectioning, staining, and replication are often used (see Ref. 113).

Characterization of the morphology of amorphous polymers (the size and shape of random coils) utilizes small-angle neutron scattering (see Ref. 118). This is possible because of the difference in scattering power of ^{1}H and ^{2}H, so that a

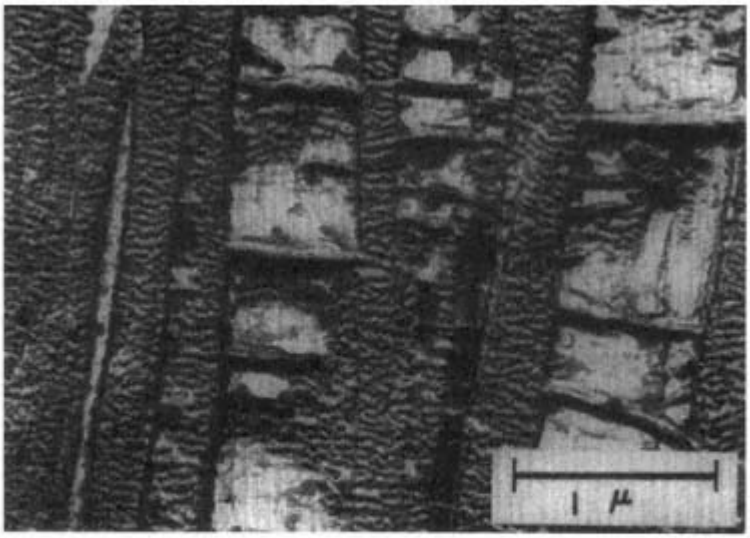

(a)

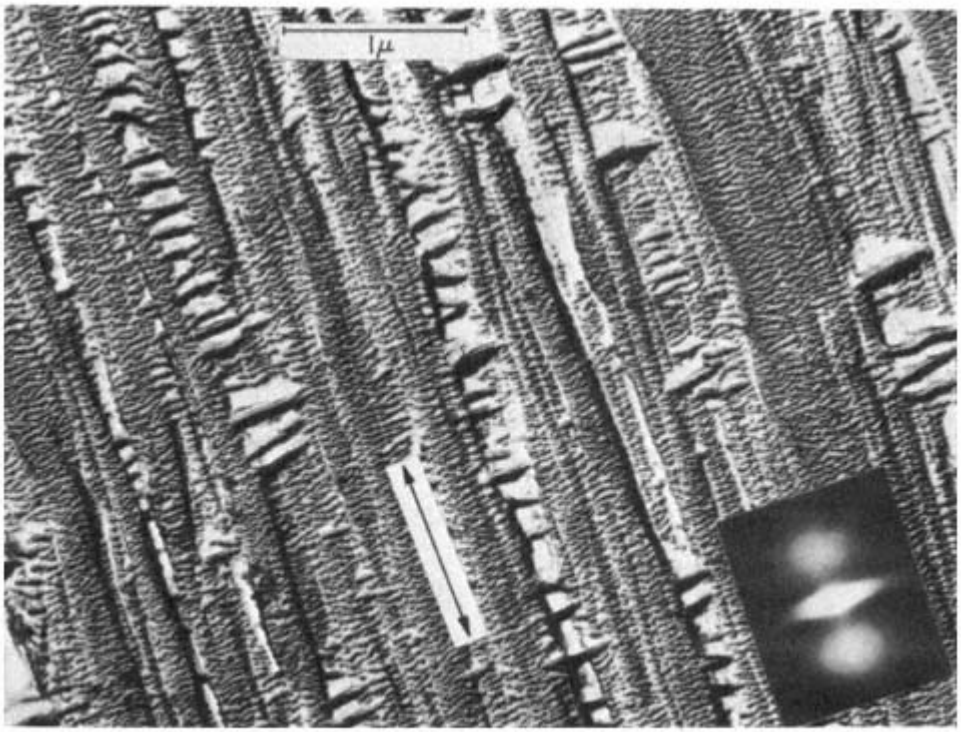

(b)

Figure 58
(a) LPE drawn 8 times at 60° C, annealed 1 hour at 110°C. (b) LPE drawn 13.5 times at 60°C, annealed at 120°C for 7 hr and treated with fuming HNO_3 for 3 hr.
The macro fibrils (linear domains of various uniform lamellar spacing) were suggested to correspond to different degrees of initial draw. A small angle electron diffraction pattern is inset
(From Ref. 114).

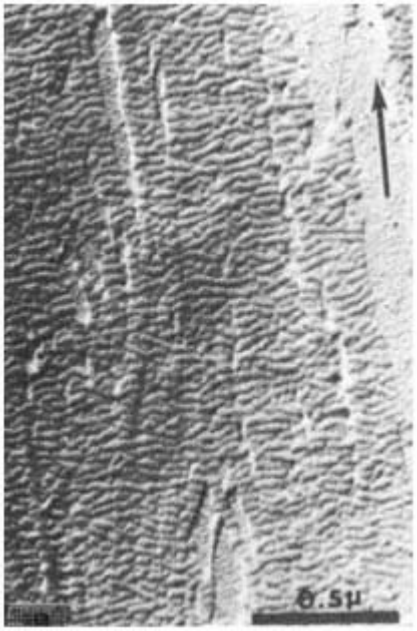

Figure 59
LPE thin film drawn and annealed
on a substrate at 125°C for 1 hr.
(From Ref. 115a.)

deuterated polymer molecule in a matrix of hydrogenated molecules, or vice versa, scatters similarly to an isolated polymer molecule in solution. Random coil dimensions (R_g); including coil anisotropy in drawn samples, and molecular (particle) weights can be obtained. Figure 63 shows an example for polystyrene. Miscibility in blends can also be studied, because the labeled molecules in a truly miscible blend have a random coil R_g, whereas clustering, resulting in larger R_g (and M_w), occurs for poorly miscible or nonmiscible blends. Small-angle neutron scattering can also be used to follow changes in the gross conformation of molecules during deformation of bulk semicrystalline polymers.

The method has also been used to characterize the overall conformation (type of folding) of the molecules in the crystalline state. For instance, the R_g of regular, adjacent-reentry folded molecules (i.e., forming a plane on the growth face) would be considerably different from the near-random coil R_g expected for a switchboard type of conformation. These studies also receive contributions from wide angle neutron diffraction, with the crystalline segments of a labeled polymer in the adjacent reentry model being adjacent to each other (at an ~4.5 Å spacing in many

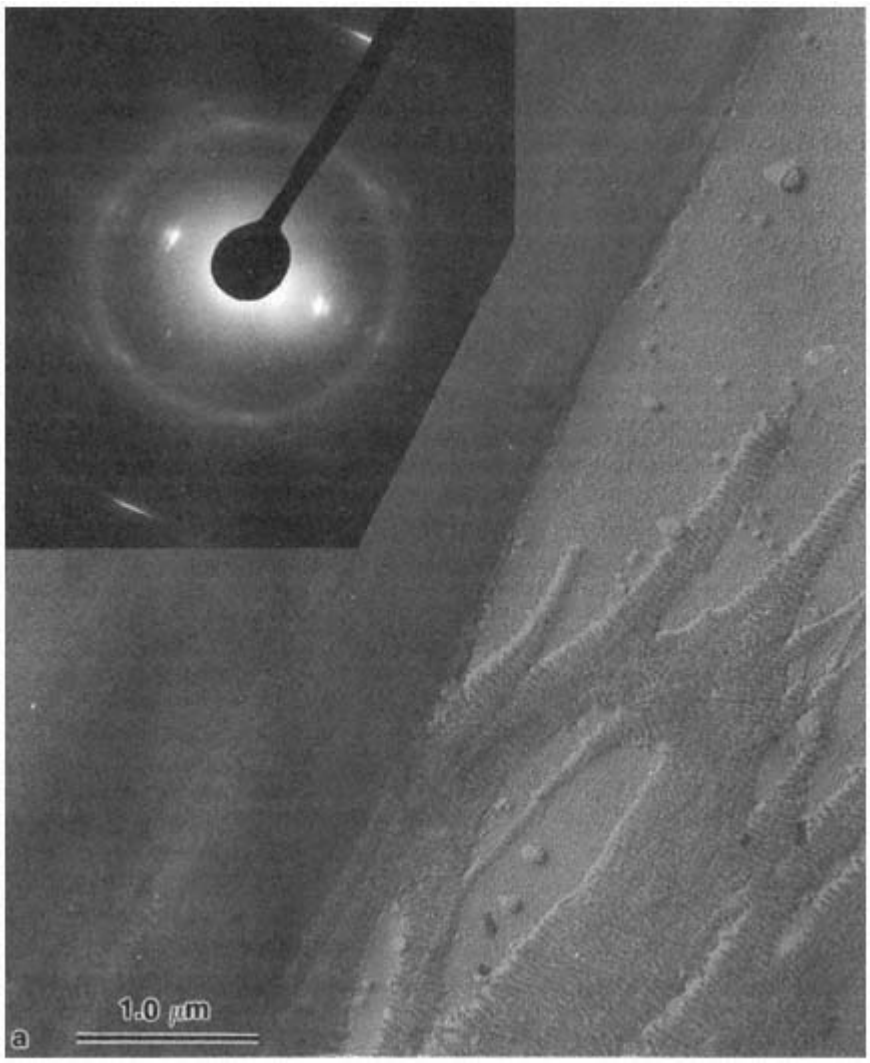

Figure 60
(a) Bright-field and (b) dark-field micrographs of a drawn annealed (130°C, 30 min) LPE thin film. (From Ref. 115b.)
(c) Phase-contrast micrographof a partially drawn, annealed film of LPE.
(From Ref. 116).

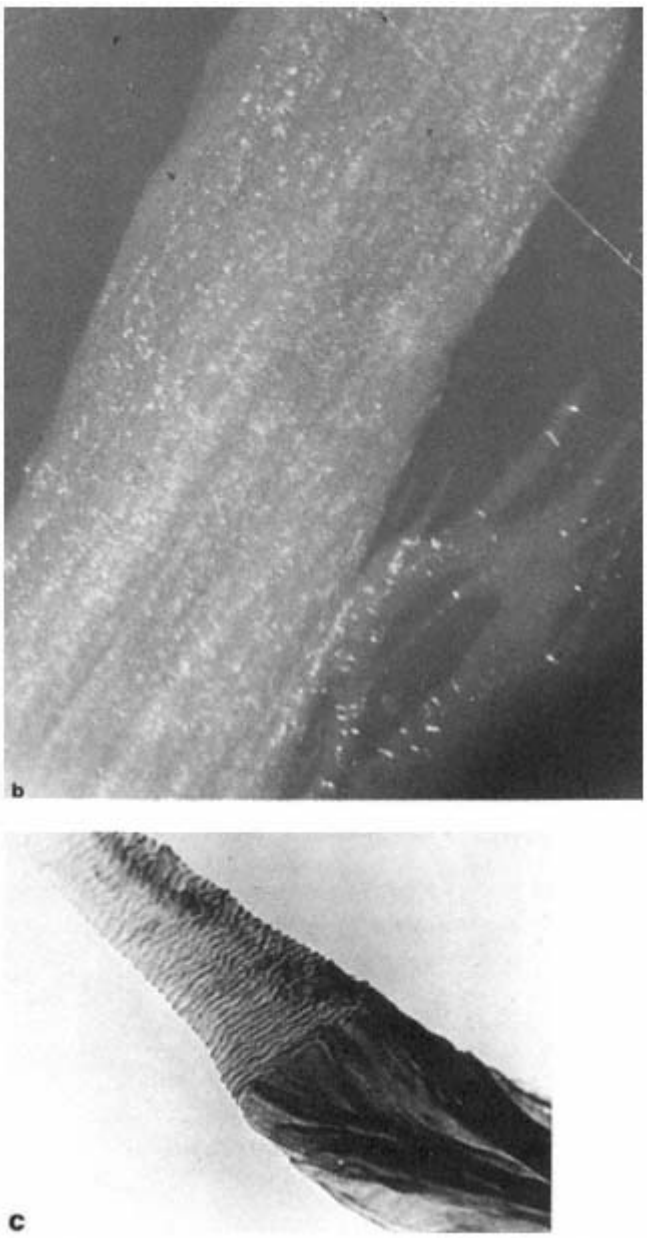

Figure 60
(continued)

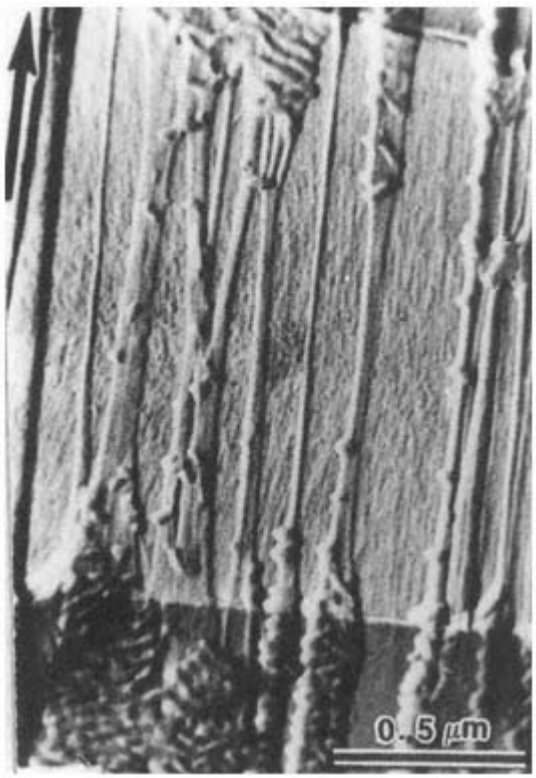

Figure 61
TEM micrograph of a drawn, annealed LPE thin film redrawn across a crack in a carbon film.
(From Ref. 115a.)

polymers) but being more widely and randomly spaced in the switchboard model. Caution in interpretation is needed, however, due to phase segregation of the components. For PE, for instance, slow cooling from the melt results in clustering of the minor component. Using quenched samples and the same data, various interpretations have resulted in values of essentially zero (less than three consecutive adjacent stems, with a 30% probability of escape to an adjacent lamella) [120] to 65% [121] adjacency (see also Ref. 118).

Although the basic structural units in polymers have a dimension on the order of 100 Å (lamellar thickness, fibril diameter, phase domain size, R_g), in crystalline polymers they are often organized into larger structures. These structures, termed spherulites, are often large enough to observe by optical microscopy (Figure 64). Using crossed polars it can be shown that the molecular axes in the lamellar crystals of which they are composed are tangentially oriented; TEM shows the

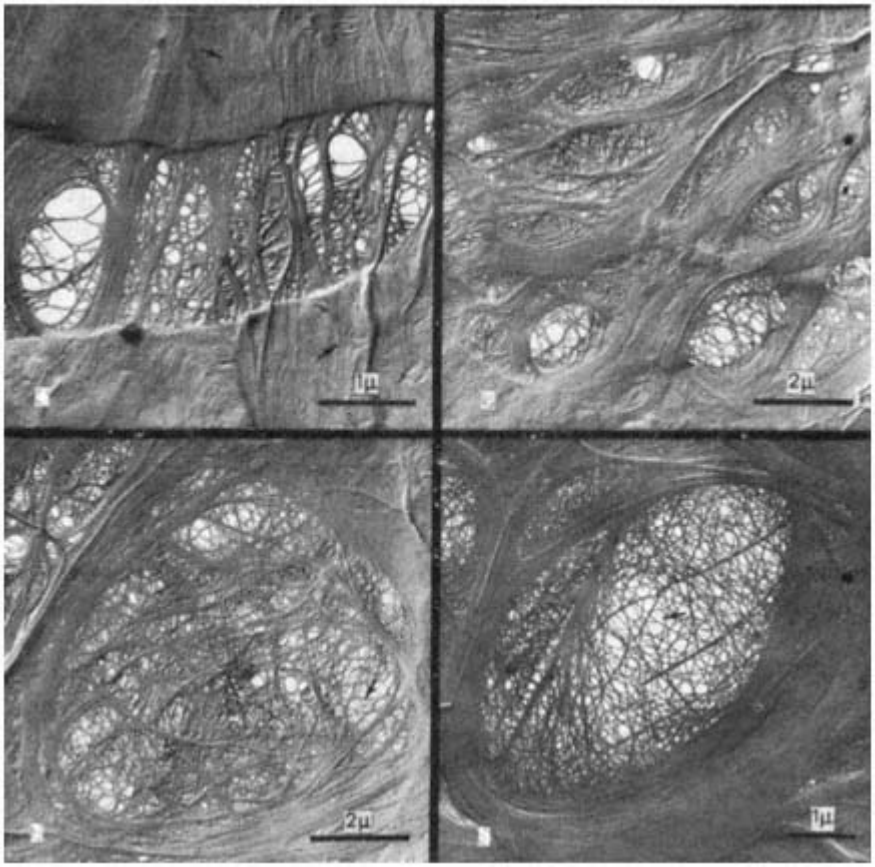

Figure 62
POM film biaxially drawn as a bubble. (From Ref. 117.) All samples drawn 1.25 × 1.25 except lower right (1.5 × 1.5). Arrows in upper left indicate short fibrils of edges of lamellae; on lower two figures branched fibrils.

lamellae grow outward from a central nucleus. For details of the growth and structure of spherulites see Refs. 89 and 122–125.

With spherulites being observed for samples of a wide range of crystallinity, the amorphous regions are incorporated within the spherulites, in between the lamellae, at the spherulite boundaries, and so forth. Tie molecules—molecules whose ends are incorporated in neighboring lamellae and traverse the intervening amorphous regions—were proposed to primarily determine the physical properties of semicrystalline polymers [126]; mats composed of solution-grown single crystals, in which few or no tie molecules are expected, flake apart readily like mica. The numbers of tie molecules are expected to increase with increasing

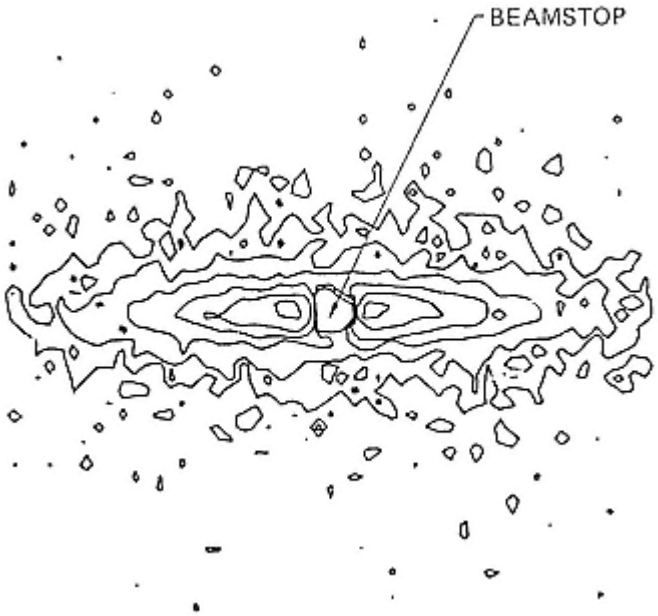

Figure 63
Two dimensional small angle neutron diffraction pattern from a drawn blend of deuterated polystyrene in normal polystyrene taken using an area detector. The asymmetry of the scattering indicates the (reciprocal asymmetry of the deuterated polystyrene coil dimensions.
(From Ref. 119.)

polymer molecular weight and rapidity of crystallization, contributing to both the toughness of the sample and, as suggested earlier, to interfibrillar links if the polymer is drawn. Although we know of no way to "count" the number of tie molecules, evidence for their existence has been obtained, such as by swelling a sample, fracturing it in the swollen state, and then subliming the swelling agent from near the fracture surface [127]. Replication of this surface, as the separation of the lamellae in the swollen state is maintained by the residual swelling agent beneath the surface, reveals "interlamellar links" spanning pores between the lamellae (Figure 65). These links, on the order of 100 Å in diameter, were proposed to be made up of tie molecules and other interlamellar amorphous material (e.g., cilia and segregated molecules) drawn into the fibrils during the swelling. Similar interlamellar links are seen between lamellae in replicas of slightly drawn samples in which the lamellae are normal to the surface [113]. In both cases, if the lamellae are not separated too far, relaxation results in closure of the pores and a "disappearance" of the fibrils. A similar structure is observed between many of the lamellae in slightly drawn samples of, for example, PP and

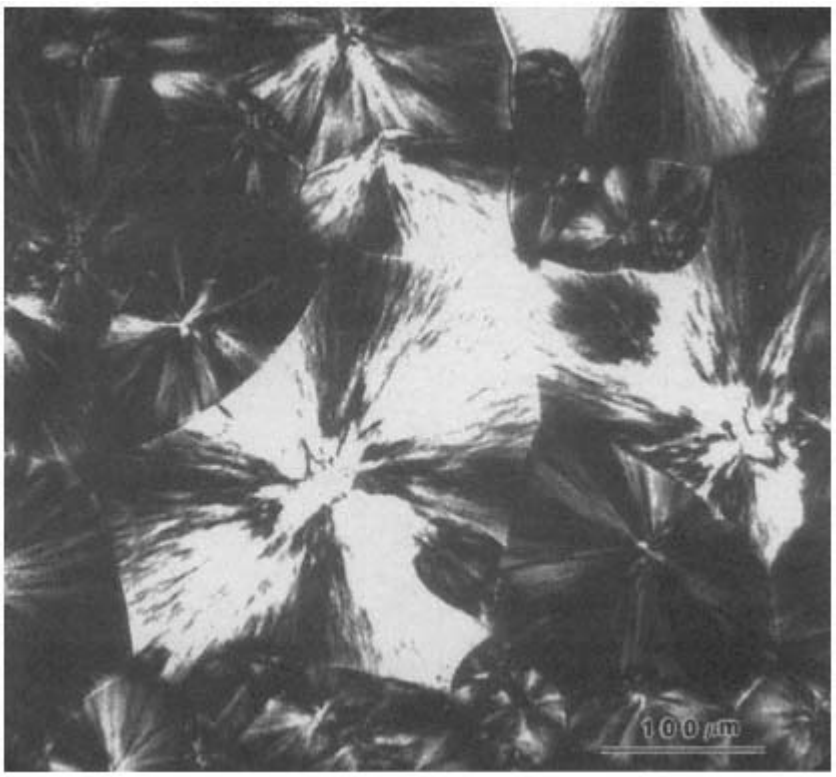

Figure 64
Optical micrograph between crossed polars of monoclinic (dark) and hexagonal (bright) crystal structure PP spherulites.
(From Reft 89.)

POM, crystallized from oriented melts (with all lamellae perpendicular to the orientation direction and the surface). If annealed taut the interlamellar links crystallize, do not relax, and permit retention of the pore structure; the result is porous membranes whose cell size can be controlled by the original processing and amount of draw [128].

With the basic structural units having dimensions on the order of 100 Å, SEM has not been very useful in characterization of their organization. Although sample preparation is easier, polymers only needing to be coated with a conducting (metal) film for most observation, the resolution is sufficiently low that TEM observation of replicas is often more revealing; in both cases only surface structure is observed. The recent development of low voltage SEMs has permitted observations of noncoated, insulating samples; the resolution, however, is even lower.

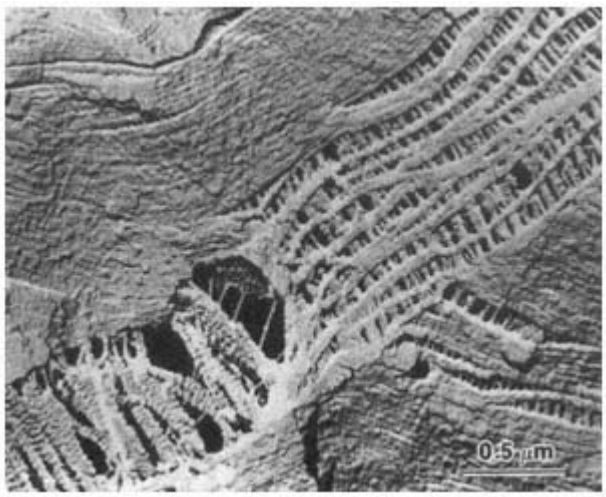

Figure 65
Fracture surface of swollen poly(4-methyl pentene-1). Interlamellar fibrils on the right can be Seen that disappear (relax) when the swelling agent is removed; on the left of the lamellae themselves have been drawn.
(From Ref. 127.)

On the other hand, due to its much greater resolving power and depth of field than an optical microscope, as well as the ability to select regions of the sample for characterization with x-ray dispersive analysis, SEM is ideal for the characterization of the surfaces of textile fibers and fabrics. Its use for these purposes is discussed in the next chapter.

In the past few years an alphabet soup of scanning probe microscopes, (SPMs) have been developed [129]. These include scanning tunneling (STM), atomic force (AFM), lateral force or friction force (LFM, FFM), and electrochemical force (ECFM) microscopy, with various microscopes having resolution sufficient to observe individual atoms (on appropriate samples), ease of sample preparation (often none) and ability to operate in air or liquids. Their use to date for polymer characterization, however, has been relatively limited. Lamellar thicknesses at the edges of solution-grown single crystals, for instance, have been measured, but the potential of observing the fold packing on their surfaces has not yet been fulfilled. Application to fibers is more difficult than to relatively flat specimens. Figure 66 shows a split PPTA fiber. The annealed fiber was embedded in epoxy and split longitudinally prior to observation. The epoxy surface is at upper right, and the skin of the fiber next, with the core having a microfibrillar morphology. Microfibrils cut during sectioning can also be seen.

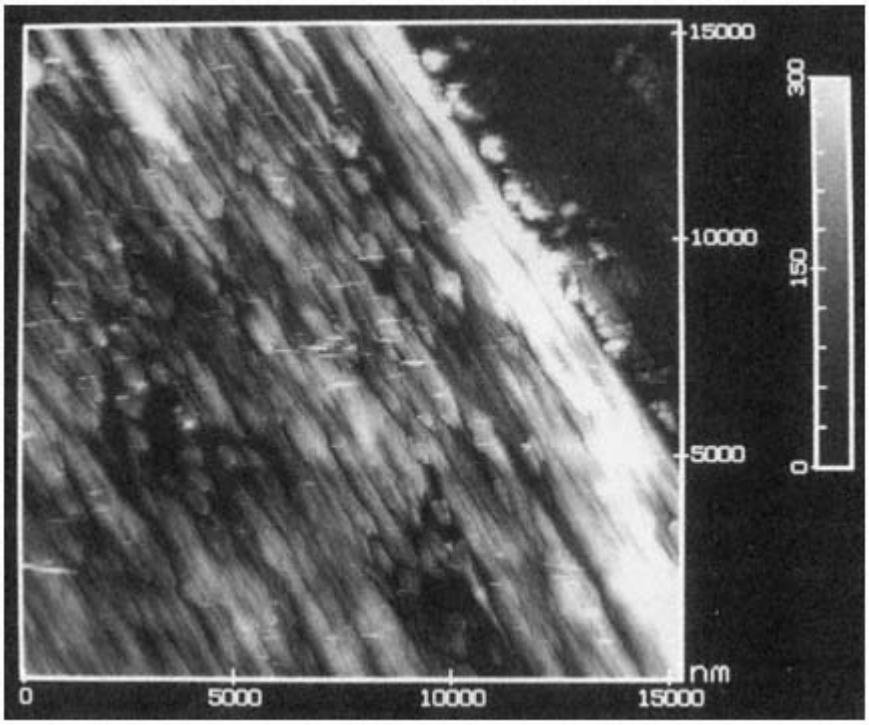

Figure 66
AFM image (scan size 15 μm of a PPTA fiber that was annealed at 450°C, embedded in epoxy and cleaved parallel to the fiber axis.
(From Ref. 130.)

Figure 67 is an AFM image of a drawn film of PE. The lamellae of the shish-kebab structure, produced by the Gohil and Petermann method [61], are clearly seen. At higher magnification (Figure 68) the authors claim individual PE molecules can be seen. The spacing, 5.6Å, is larger than the expected 4.9-Å spacing of the 100 planes. Although most of the images published to date, in my opinion, have not been more informative than possible through TEM and SEM, the methods have considerable potential. For instance, for step heights less than 20–30 Å (as possible, e.g., on the as-polymerized polyester crystals [Figures 33 and 35]) they would be far superior to TEM; the latter is restricted to ~ 15Å visibility and ± 10A accuracy due to the granulation of the shadowing material. Most representative of that potential is a recent publication by Stocker et al. [131b] on the direct observation of the packing of right and left handed helical s-PP molecules on the edges of lamellar crystals (Figure 69) grown by epitaxy. Figure 70 is a high resolution AFM micrograph, with the sample and microscope tip in water,

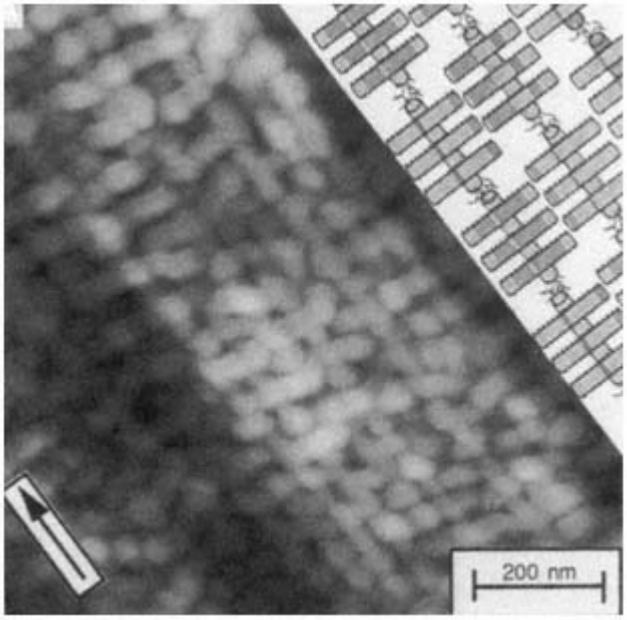

Figure 67
AFM image (in propanol) of film of polyethylene drawn from the melt by the method of Gohil and Petermann [61]. The lamellae of the shish-kebab structure protrude a few nanometers out of surface. A model, based on TEM studies, is at upper right.
(From Ref. 131a.)

of a portion of the edge of one of the lamellae, the reduction of capillary forces making it possible to use imaging forces nearly an order of magnitude less than in air.

While the unfiltered images, as in Figure 70a, are noisy, the 2D FFT in Figure 70b clearly shows substantial periodicity is present and even in the unfiltered image one can clearly see orientation 10° to the vertical, as well as a periodic structure at an ~45° angle to that orientation. In the filtered image, i.e., reconstructed using the maxima in the FFT, not only is the periodicity displayed more clearly, but the suggestion is that individual CH_2 and CH_3 groups are being resolved, as suggested by the model in Figure 70d, with the uppermost groups, visualized in the AFM, being darkened. As the authors note, the helices of one hand are better resolved than those of the opposite hand, here left handed better than right handed. This is due to the resolution in the scan direction being limited by a stick-slip process of the tip while the better resolution in the orthogonal direction is dependent on the density of the scan lines. For applications of the various methods the reader is directed to Ref. 129 and the manufacturer's literature.

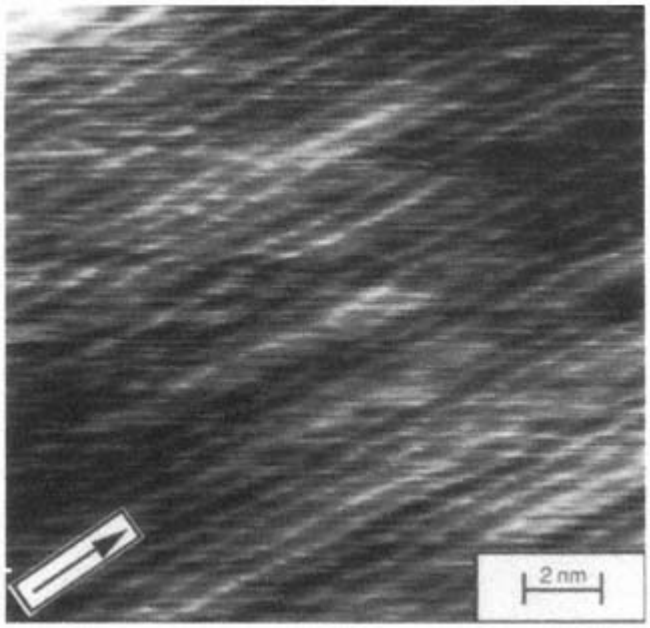

Figure 68
AFM image of a portion of one of the lamellar edges in Figure 67, at higher magnification. (From Ref. 131.)

III— Physical Properties

Because of their importance in practical textile use, characterization of single fiber tension, flexure, and friction properties, as well as the hand of textiles, is described in individual chapters in this volume. The chemical, biological, and thermal barrier properties of textiles are also described. Here we are concerned with physical properties of the polymers themselves that are of concern in their application as textile fibers.

With melt viscosity already described earlier, our primary concern is with their relaxation and transition behavior, that is, the temperatures of onset of particular types of segmental motion at the frequency of the measurement and the effects of stress on individual molecules. These are discussed next.

The primary techniques for relaxation measurements—creep, stress relaxation, and dynamic mechanical analysis (DMA)—are well known, with dielectric spectroscopy also being useful if the polymer contains polar groups, and DSC (as described earlier) being used for T_g (for discussions of method, results and interpretation see, e.g., Ref. 132). An additional, somewhat less used technique of in-

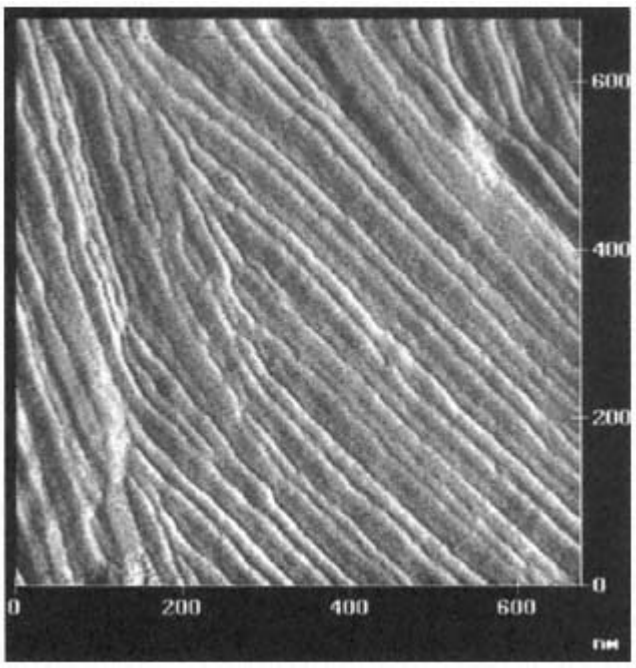

Figure 69
AFM image, in water, of a s-PP film crystallized epitaxially on an oligophenyl substrate. The lamellae are normal to the substrate permitting the high resolution images in Figure 70 of the molecules on the fold plane on their edge. (From Ref. 131b.)

terest is "broad-line" NMR. Changes in the second moment (width) of the NMR line can be related to the types of motion involved, with applications to oriented systems aiding in defining the types of motion. For these purposes measurements of spin—lattice and spin—spin relaxation times (T_1 and T_2) are also of value (see Refs. 7 and 8). An example of the use of the shape of the broad line is shown in Figure 71. The spectrum was divided into three peaks: L_s for the mobile protons in the amorphous regions, L_b for the immobile protons in the rigid amorphous (interphase) regions, and G for the immobile protons in the crystalline regions. The relative areas of the peaks are directly proportional to the fractional amounts in each type of region. The results are thus similar to those obtained by the "whole pattern" x-ray method described earlier. It is noted the measurement was made at 200°C, well above T_g and only slightly below T_m (215°C).

With the lower temperature relaxations generally having lower activation energies, their relaxation temperature increases faster with frequency of measure-

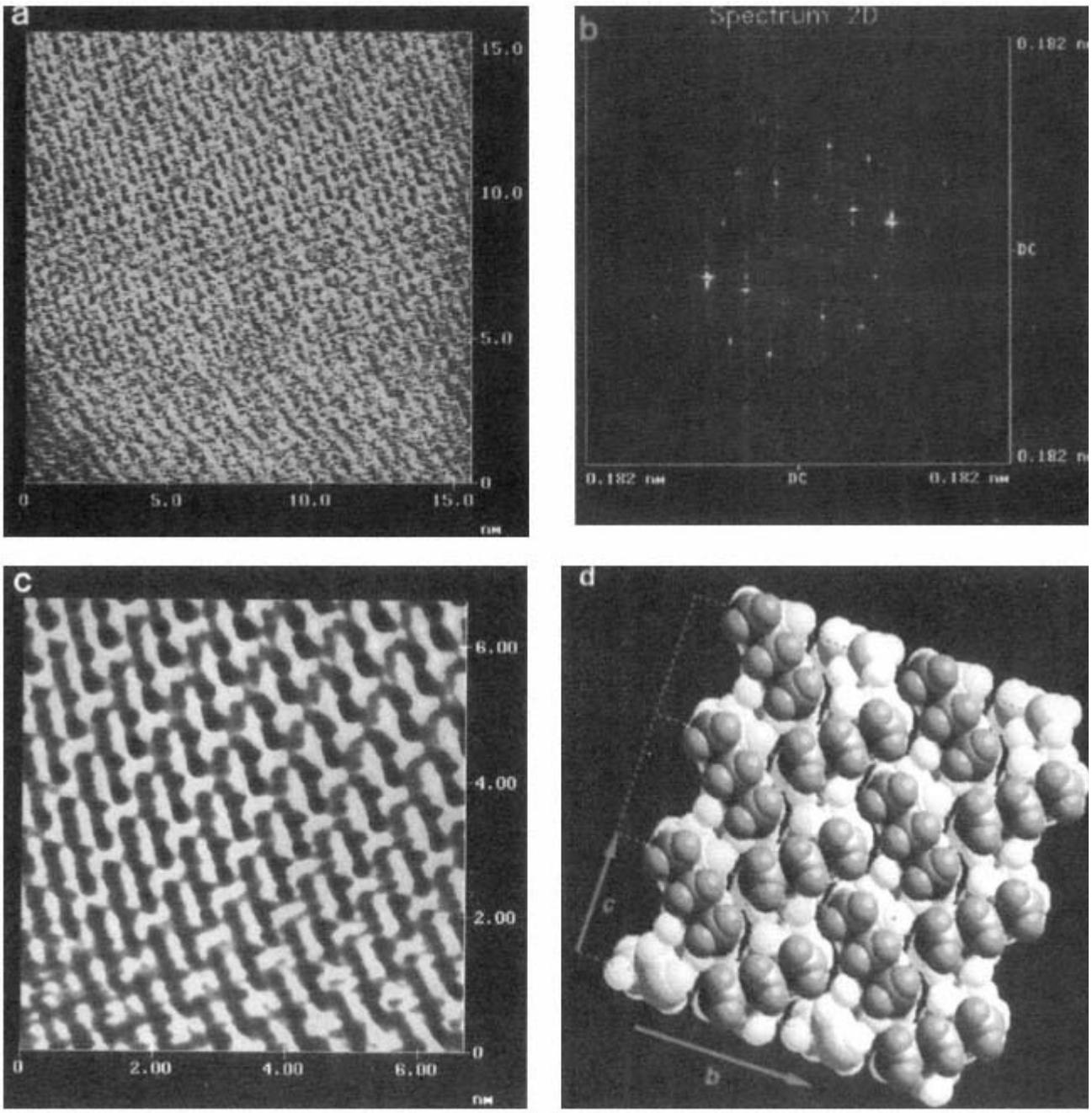

Figure 70
(a) High resolution AFM image of an area near the center of Figure 69. The chain axes are oriented at ~10°C to the vertical. (b) Two dimensional fast Fourier transform of a portion of the image in (a). (c) Reconstruction of the image using the 20 pairs of spots in (b). (d) Schematic representation of the molecular arrangement in (c). The rows of three CH_2 conespond to "exposed" CH_3-CH_2-CH_3 groups; their alternate tilt in (c) and (d) confirms the proposed alternate left and right handed helical molecule packing in the crystal.
(From Ref. 13lb.)

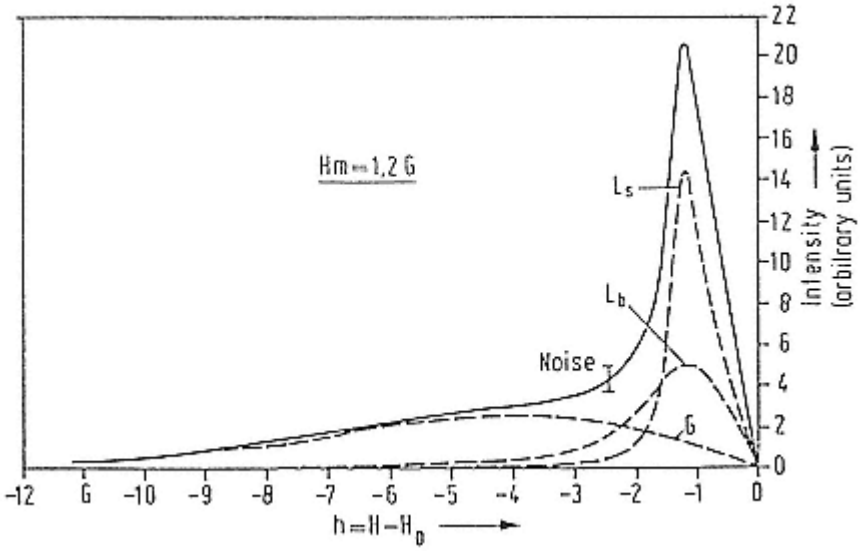

Figure 71
Broad line NMR spectrum of nylon 6 after annealing 20 hr at 200°C.
(From Ref. 133.)

ment than the higher temperature relaxations; that is, the relaxations are closer together with higher frequency. Thus low frequencies (as in creep and stress relaxation) permit better resolution of the relaxations. Two relatively recent techniques taking advantage of this effect are thermally stimulated creep and current. In thermally stimulated creep, which can be applied to oriented samples, a load is applied to a sample at low temperature and the response is measured as the temperature is slowly raised; changes in creep rate occur as various types of molecular motion become activated. In thermally stimulated current (or thermally stimulated discharge current) an electric field is applied to a film with conductive coatings on both surfaces at a temperature above that of any relaxation being probed, the sample is cooled to a suitably low temperature, the field is turned off, and the current through an external circuit is measured as the film is heated. The elevated temperature field orients any mobile dipoles in the film, which remain frozen when the field is removed at low temperature. When segmental motion occurs as the sample is heated, the dipoles relax, and an image charge on the electrode is released; it is this that is measured. Effective frequencies are 10^{-3}–10^{-4} Hz, permitting excellent resolution of the relaxation processes. By polarizing the samples over only a limited temperature range, distributions in relaxation times in individual peaks can be determined, References 134 and 135 are excellent reviews of the techniques and their application.

Although the foregoing discusses primarily the measurement of relaxation temperatures, all can be applied to T_g and T_m measurements as well, with the qualification that for application of mechanical measurement the sample needs to maintain its integrity through the transition; for example, T_g would be measured by DMA for a semicrystalline polymer but not for a wholly amorphous one.

WAXD and IR have been used to characterize the effect of stress on individual molecules: WAXD for the modulus of crystalline regions, and IR for changes in vibration frequencies with stress in both crystalline and amorphous regions. The WAXD measurements (e.g., Ref. 6) rely on measurement of changes in **c** axis spacings with stress in well-oriented samples. The ratio of the stress to the **c** axis strain is the modulus of the crystalline regions. Table 8 is a comparison of observed and calculated values for a number of polymers. The single molecule values are obtained by multiplying the crystal moduli by the cross-sectional area of the molecule.

IR can also be used to study the effects of stress on polymers. For steady stress the goal is to obtain the molecular stress distribution, using initially highly oriented samples. Under stress small shifts in position and shape of some of the peaks are observed, with the shift depending on the initial draw ratio and thermal history of the sample. In other cases, where a phase change occurs under stress, there can be a change in absorbance of appropriate bands. Figures 72 and 73 show examples of these effects for PET and polybutylene terephthalate (PBT), respectively.

Zhurkov et al. [136] have shown that the frequency shift for many bands is approximately linear with applied stress, that is, $\Delta\nu = \alpha_x\sigma$, where α_x depends on the morphology of the sample and the temperature [138]. The results in Figure 72, for the 976 cm^{-1} band (trans, primarily crystalline), show that significant variations in α_x occur for various degrees of initial, controlled shrinkage during annealing (at 155°C for 17 hr in nitrogen) and that there is a threshold stress before shifting occurs. The latter is interpreted in terms of the disordered amorphous chains beating the initial stress. The decrease in α_x with initial shrinkage is attributed to chain disorientation during annealing and to variations in the crystalline texture.

In PBT there is a reversible change in crystal structure under stress, with the aliphatic segments transforming from gauche-trans-gauche to all-trans. As shown in Figure 73, the decrease in CH_2 absorbance at 1460, beginning at 2–3% strain, accompanies the beginning of the phase change, while the 1485 cm^{-1} CH_2 band, attributed to the all-trans conformation, increases, both in a reversible manner. The 1510 cm^{-1} *p*-phenylene band was used as an internal thickness band to correct for changes in thickness.

Table 8 Comparison of Observed and Calculated (from Bond Energies) Single Chain Moduli

	Tenacity		Elongation	Macroscopic modulus		Crystallite modulus[b]		M_p
Polymer[a]	(g/denier)	(kg/mm^2)	(%)	(g/denier)	(dyn/cm^2)	Obsd.[c] (dyn/cm^2)	Calcd. dyn/cm^2)	(decomposition point) (°C)
Kevlar	25	330	5	850	111×10^{10}	153×10^{10}	182×10^{10}	(500)
PRD-49	15	200	3	1050	134	—	163	(500)
Nomex	5.5	68	35	82	10	88	90	(415)
PET	9.0	110	7	160	19.5	108	124[d]	260
it-PP	9.0	74	15	120	9.6	34	28[e]	170
PE	9.0	78	8	100	8.5	235	296*e*	135
Nylon 6 (α)	9.5	97	16	50	5.0	165	244[f]	225
PEOB (x97;)	5.3	64	25	75	8.9	5.9	2.4	225

[a]PEOB: poly(ethylene oxybenzoate).
Source: Ref. 6.

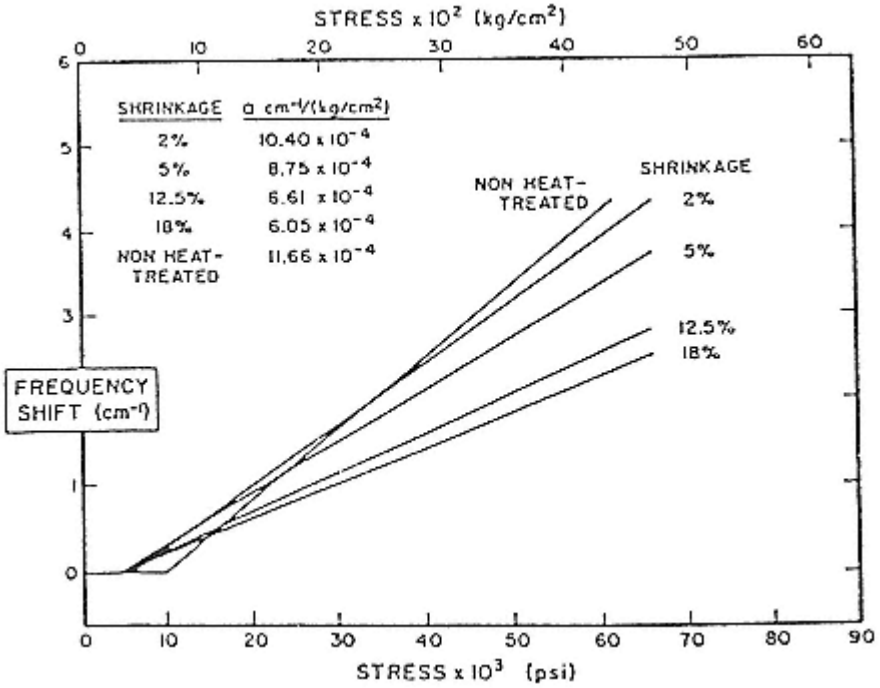

Figure 72
Frequency shift (of the peak) versus applied stress for PET films for the 976 cm^{-1} trans band. Controlled prior shrinkage was accomplished by annealing.
(From Ref. 138 as reported in Ref. 137).

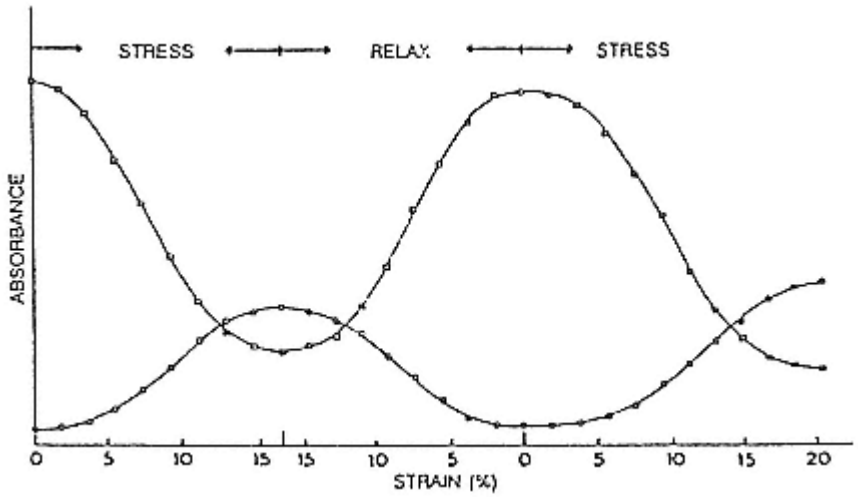

Figure 73
Absorbance of the CH_2 bands at 1460 cm^{-1} (⊡) relaxed form and 1485 cm^{-1} (o) stressed form as a function of reversible stress and strain. The absorbances were corrected for changes in sample thickness using a 1510 cm^{-1} aromatic ring band as an internal thickness band.
(From Ref. 139.)

References

1. C. Booth and C. Price, eds., *Comprehensive Polymer Science*, Vol. 1, *Polymer Characterization*, Pergamon Press, Oxford, 1992.

2. J. Haslem, H. A. Willis, and D. C. M. Squirrel, *Identification and Analysis of Plastics*. 2nd ed. Butterworth, London, 1972.

3. D. Braun, *Simple Methods for Identification of Plastics*, Hanser, Munich, 1982.

4. J. Brandrup and E. H. Immergut, eds., *Polymer Handbook*, 3rd ed., Wiley, New York, 1989.

5. (a) G. S. Beddard, Emission Spectroscopy, *Comprehensive Polymer Science*, Vol. 1, (C. Booth and C. Price, eds.), Pergamon Press, Oxford, 1992, Chap. 22.2 (b)G. Kampf, Characterization of Plastics by *Physical Methods*, Hanser (Macmillan), Munich (New York), 1986, Chap. 7.

6. H. Tadokoro, *Structure of Crystalline Polymers*, Wiley, New York, 1979.

7. G. Kampf, *Characterization of Plastics by Physical Methods*, Hanser (Macmillan), Munich (New York), 1986.

8. J. L. Koenig, *Spectroscopy of Polymers*, American Chemical Society, Washington, D.C., 1992.

9. J. L. Koenig, *Chemical Microstructure of Polymer Chains*, Wiley, New York, 1982.

10. (a) J. G. Grasselli and W. M. Ritchey, eds., *Atlas of Spectral Data and Physical Constants for Organic Compounds*, Vol. 1, 2nd ed., CRC Press, Cleveland, OH, 1975. (b) R. C. Weast, ed., Handbook of Chemistry and Physics, CRC Press, Boca Raton, FL (annual).

11. (a) L. J. Bellamy, *The Infrared Spectra of Complex Molecules*, Wiley, New York, 1975. (b) D. Dolphin and A. Wick, *Tabulation of Infrared Spectra Data*, Wiley, New York, 1977.

12. J. C. Hennicker, *Infrared Spectrometry of Industrial Polymers*, Academic Press, New York, 1967.

13. F. A. Bovey, *Nuclear Magnetic Resonance Spectroscopy*, 2nd ed., Academic Press, San Diego, 1988.

14. (a) F. A. Bovey, *High Resolution NMR of Macromolecules*, Academic Press, New York, 1972. (b) E. M. Mohacsi, *J. Chem Educ. 41*:38(1964).

15. R. A. Komarshi, ed., *High Resolution NMR of Synthetic Polymers in Bulk*, VCH, Deerfield Beach, Fla., 1986.

16. R. Holm and S. Storp, *Surf. Interface Anal*. 2:96 (1980).

17. R. Holm, Proc. 8th Int. Microchem. Symp., 1980, p. 257.

18. G. Bucci and T. Simonazzi, *J. Polym. Sci. C7*:203 (1964). See also: C. Tosi and F. Campbell, *Adv. Polym. Sci. 12*:87 (1973).

19. F. M. Schnepel, *Chem. Uns. Zeit 13*:33 (1979).

20. J. M. O'Reilley and R. A. Mosher, *Macromolecules 14*:602 (1981).

21. J. T. Arnold, S. Dharmatti, and M. E. Packard, *J. Chem. Phys. 19*:507 (1951).

22. F. A. Bovey, F. C. Schilling, F. L. McCrackin, and H. L. Wagner, *Macromolecules 9*:76 (1976).

23. R. C. Ferguson, *Macromolecules 2*:237 (1969).

24. J. C. Randell, *Polymer Characterization by ESR and NMR* (A. E. Woodward and F. A. Bovey, eds.), ACS Symp. Series 142, American Chemical Society, Washington, D.C., 1980.

25. J. Schaefer, M. D. Sefcik, E. D. Stejskal, and R. A. McKay, *Macromolecules 14*:188 (1981).

26. (a) D. T. Clark, W. J. Feast, I. Ritchie, W. K. R. Musgrave, M. Modena, and M. Ragazzini, *J. Polym. Sci., Polym. Chem. Ed., 12*:1049 (1974). (b) D. T. Clark, ESCA applied to polymers, *Advances in Polymer Science, Vol. 24*, (H. J. Cantow et al., eds.), Springer Verlag, Berlin, 1977.

27. F. W. Billmeyer, *Textbook of Polymer Science*, Interscience, Wiley, New York, 1962.

28. (a) E. A. Collins, J. Bares and F. W. Billmeyer, *Experiments in Polymer Science*, Wiley, New York, 1973. (b) J. V. Dawkins, Size exclusion chromatography, *Comprehensive Polymer Science*, Vol. 1 (C. Booth and C. Price, eds), Pergamon Press, Oxford, 1992, Chap. 12.

29. F. M. Mirabella, Jr., and E. A. Ford, *J. Polym. Sci., Polym, Phys. B25*:71 (1987).

30. J. R. Shaefgen and P. J. Flory, *J. Am. Chem. Soc. 70*:2709 (1948).

31. M. L. Huggins, *J. Am. Chem. Soc. 64*:2716 (1942).

32. E. O. Kraemer, *Ind. Eng. Chem. 30*:1200 (1938).

33. This equation is usually attributed to Mark, Houwink, and Sakurada; see Ref. 30.

34. T. G. Fox, S. Gratch, and S. Loshack, *Rheology*, Vol. 1 (F. R. Eirich, ed.), Academic Press, New York, 1956, Chap. 12.

35. S. Oka, *Rheology*, Vol. 3 (F. R. Eirich, ed.), Academic Press, New York, 1960, Chap. 2.

36. J. E. Mcintyre, Polyester fibers, *Handbook of Fiber Science and Technology*, Vol. IV, *Fiber Chemistry* (M. Lewin and E. M. Pearce, eds.), Marcel Dekker, New York, 1985.

37. A. I. Kitaigorodski, *Organic Chemical Crystallography*, Consultants Bureau, New York, 1961.

38. G. Natta and P. Corradini, *Nuovo Cimento, Suppl*. 15:9 (1960).

39. (a) Ref. 6. (b) L. E. Alexander, *X-Ray Diffraction Methods in Polymer Science*, Wiley, New York, 1969. (c) M. Kakudo and N. Kasai, *X-Ray Diffraction by Polymers*, Elsevier, Amsterdam, 1972. (d) J. E. Spruiell and E. S. Clark, *Methods of Experimental Physics*, Vol. 16B (R. A. Fava, ed.), Academic Press, New York, 1980, Chap. 6. (e) F. J. Balta-Calleja and C. G. Vonk, *X-ray Scattering of Synthetic Polymers*, Polymer Science Library, Vol. 8 (A.D. Jenkins, ed.), Elsevier, Amsterdam, 1989.

40. B. K. Vainshtein, *Diffraction of X-rays by Chain Molecules*, Elsevier, Amsterdam, 1966.

41. G. M. Bhatt, J. P. Bell, and J. R. Knox, *J. Polym. Sci., B14*:373 (1976).

42. (a) R. J. Young, *Characterization of Solid Polymers* (S. J. Spells, ed.), Chapman & Hall, London, 1994, Chap. 6. (b) N. Schlotter, Raman spectroscopy, *Comprehensive Polymer Science*, Vol. 1 (C. Booth and C. Price, eds.), Pergamon Press, Oxford, 1992, Chap. 21. (c) P. Hendra, C. Jones, and G. Warnes, *Fourier Transform Raman Spectroscopy*, Ellis Horwood, Chichester, 1991.

43. J. C. Rodriguez-Cabello, L. Quintanilla, and J. M. Paster, *J. Raman Spectrosc. 25*:335 (1994).

44. L. Quintanilla, J. C. Rodriguez-Cabello, T. Jawhari, and J. M. Paster, *Polymer 34*:3787 (1993).

45. R. de P. Daubeny, C. W. Bunn, and C. J. Brown, *Proc. R. Soc*. (*Lond*.) *A226*:531 (1954).

46. R. Boyer, *Macromolecules* 6:288 (1973) and *J. Macromol. Sci., Phys. B8*:503 (1973).

47. J. L. Koenig and M. Hannon, *J. Macromol. Sci., Phys. Bl*:119 (1967).

48. (a) Cerius², Molecular Simulations, Inc. (b) SYBYL, Tripos Associates, Inc. (c) Biosym Technologies, Inc.

49. T. C. Long, J. Liu, B.-L. Yuan and P. H. Geil, paper presented at American Physical Society Meeting, San Jose, Calif., March 1995, in press.

50. W. Claffey, K. Gardner, J. Blackwell, J. Lando, and P. H. Geil, *Phil. Mag. 30*:1223 (1974).

51. (a) D. L. Dorset, *Characterization of Solid Polymers* (S. J. Spells, ed.), Chapman & Hall, London, 1994, Chap. 1. (b) D. L. Dorset, *Macromolecules 25*:4425 (1992).

52. (a) Z. G. Pinsker, *Electron Diffraction*, Butterworths, London, 1953. (b) B. K. Vainshtein, *Structure Analysis by Electron Diffraction*. Macmillan, New York, 1964.

53. J. R. Fryer and D. L. Dorset, eds., *Electron Crystallography of Organic Molecules*, NATO ASI Series, Vol. C328, Kluwer, Dordrecht, 1991.

54. H. Hasegawa, W. Claffey, and P. H. Geil, *J. Macrotool. Sci., Phys. B13*:89 (1977).

55. B. Moss and D. L. Dorset, *J. Macromol. Sci., Phys*. B22:69 (1983).

56. (a) J. C. Wittman, A. M. Hodge, and B. Lotz, *J. Polym. Sci., Polym. Phys. Ed. 21*:2495 (1983) (b) J. C. Wittmann and B. Lotz, *Prog. Polym. Sci. 15*:909 (1990).

57. S. H. Carr, A. Keller, and E. Baer, *J. Polym. Sci. A-2 8*:1467 (1970).

58. (a) P. H. Geil, *J. Appl. Phys. 33*:642 (1962). (b) S. V. Meille, T. Konishi, and P. H. Geil, *Polymer 25*:773 (1984).

59. D. L. Dorset, M. P. McCourt, S. Kopp, J. C. Wittman, and B. Lotz, *Acta Crystallogr. B50*:201 (1994).

60. R. G. Scott, *J. Polym. Sci. 57*:405 (1962).

61. R. M. Gohil and J. Petermann, *J. Macromol. Sci., Phys. B18*:217 (1980).

62. F. Rybnikar, B. L. Yuan, and P. H. Geil, *Polymer 35*:1831 (1994).

63. D. Dean and P. H. Geil, paper presented at American Physical Society Meeting, Pittsburgh, March 1994, in press.

64. F. Rybnikar, J. Liu, and P. H. Geil, *Makromol. Chem. Phys. 195*:81 (1994).

65. P. H. Geil, paper presented at Europhysics Conf. on Macromolecular Physics, Prague, July 1995, in press.

66. J. Liu, T. C. Long, B. -L. Yuan, and P. H. Geil, paper presented at Europhys. Conf. Macromol. Phys., Prague, July 1995, in press.

67. A. J. C. Wilson, *Nature 150*:151 (1942).

68. P. H. Geil, *J. Macromol. Sci., Chem. A1*:325 (1967).

69. (a) J. Liu, F. Rybnikar and P. H. Geil, *J. Polym. Sci., Polym. Phys. Ed. B30*:1469 (1992). (b) J. Liu and P. H. Geil, in press.

70. P. Iannelli, D. Y. Yoon, and W. Parrish, *Macromolecules 27*:3295 (1994).

71. J. Liu, F. Rybnikar, and P. H. Geil, *J. Macromol. Sci., Phys. B32*:395 (1993).

72. D. Y. Yoon, N. Masciocchi, L. E. Depero, C. Viney, and W. Parrish, *Macromolecules 23*:1793 (1990).

73. T. Thomsen, H. G. Zachmann, and H. R. Kricheldorf, *J. Macromol. Sci., Phys. B30*:87 (1992).

74. M. Tsuji, Electron microscopy, *Comprehensive Polymer Science*, Vol. 1 (C. Booth and C. Price, eds.), Pergamon Press, Oxford, 1992, Chap. 34.

75. M. Tsuji, A. Uemura, M. Ohara, S. Isoda, A. Kaweguchi, and K. Katayama, *Koenshu-Kyoto Daigaku Nippon Kagaku Seni Kenhyrucho 44*:1 (1987).

76. (a) M. Tsuji, S. Isoda, M. Ohara, A. Kawaguchi, and K. Katayama, *Polymer 23*:1568 (1982). (b) S. Isoda, M. Tsugi, M. Ohara, A. Kawaguchi, and K. Katayama, *Polymer*

24:1155 (1983). (c) K. Katayama, S. Isoda, M. Tsuji, M. Ohara, and A. Kawaguchi, *Bull. Inst. Chem. Res. Kyoto Univ. 62*:198 (1984). (d) M. G. Dobb, D. J. Johnson, and B. P. Saville, *J. Polym. Sci., Polym. Phys. Ed. 15*:2201 (1977).

77. (a) J. L. Koenig, *Spectroscopy of Polymers*, American Chemical Society, Washington, D.C., 1992, Chap. 10. (b)V. D. Fedotov and H. Schneider, *Structure and Dynamics of Bulk Polymers by NMR Methods*, Springer-Verlag, New York, 1989.

78. (a) Y. Fu, W. R. Busing, Y. Jin, K. A. Affholter, and B. Wunderlich, *Macromolecules 26*:2187 (1993). (b) Y. Fu, W. R. Busing, Y. Jin, K. A. Affholter, and B. Wunderlich, *Macromol. Chem. Phys. 195*:803 (1994). (c) Y. Fu, B. Annis, Y. Jin, A. Boller, Y. Jin, and B. Wunderlich, *J. Polym. Sci., Polym. Phys. B32*:2289 (1994).

79. (a) A. Immirzi and P. Iannelli, *Gazz. Chim. Ital. 117*:201 (1987); *Macromolecules 21*:768 (1988). (b) P. Iannelli and A. Immirzi, *Macromolecules 22*:196 (1989); *23*:2375 (1990). (c) W. R. Busing, *Macromolecules 23*:4608 (1990).

80. (a) M. J. Richardson, *Thermal Analysis in Comprehensive Polymer Science*, Vol. 1 (C. Booth and C. Price, eds.), Pergamon Press, Oxford, 1992. (b) T. Hatakeyama and F. X. Quinn, *Thermal Analysis*, Wiley, Chichester, 1994.

81. (a) S. Sauerbrunn, B. Crowe, and M. Reading, *Am. Lab. 24*(*12*):44 (1992). (b) S. Sauerbrunn and P. Gill, *Am. Lab. 25*(*14*):54 (1993). (c) S. Sauerbrunn and L. *Thomas, Am. Lab. 27*(*1*): 19 (1995).

82. J. DeChant, *Infrared Spectroscopic Investigations on Polymers*, Akademie-Verlag, Berlin, 1992.

83. J. L. Koenig, personal communication.

84. G. Natta and P. Corradini, *Nuovo Cimento* (*Suppl.*), *15*:40 (1960).

85. W. O. Statton and P. H. Geil, *J. Appl. Polym. Sci. 3*:357 (1960).

86. R. Hosemann and A. H. Hindeleh, *J. Macromol. Sci., Phys. B34*(*4*):327 (1995).

87. (a) W. Ruland, *Acta Crystallogr. 14*:1180 (1961). (b) W. Ruland, *Polymer 5*:89 (1964).

88. C. G. Vonk, *J. Appl. Crystallogr. 6*:148 (1973).

89. P. H. Geil, *Polymer Single Crystals*, Wiley, New York, 1963.

90. J. J. Hermans, P. H. Hermans, D. Vermaas, and A. Weidinger, *Rec. Trau. Chim. Pzys Bas 65*:427 (1946).

91. (a) W.O. Statton and G. M. Godard, *J. Appl. Phys. 28*, 1111 (1957). (b) H. Tadokoro, K. Tatsuka, and S. Murahashi, *J. Polym. Sci. 59*:413 (1962).

92. (a) E. S. Clark and M. R. Boone, Conf. Proc. Soc. Plastics Eng., ANTEC 90, 542 (1990). (b) E. S. Clark, personal communication.

93. J. J. Lear, Ph.D. thesis, University of Illinois, Urbana, 1990.

94. International Standard ISO 2557/1 (1976E) and 2557/2 (1979E).

95. A. N. J. Heyn, *Fiber Microscopy, A Textbook and Laboratory Manual*, Interscience, New York, 1954.

96. (a) C. R. Desper, J. L. Mead, M. Sussman and E. Kasch, presented at Matl's Res. Soc. Meeting, Boston, Dec 1992. (b) C. R. Desper, *J. Macromol. Sci., Phys. B7*:105 (1973).

97. (a) R. J. Samuels, *Makromol. Chem.* (*Suppl*), *4*:241 (1981). (b) F. M. Mirabella, Jr., *J. Polym. Sci., Polym. Phys. B25*:591 (1987).

98. L. J. Fina and J. L. Koenig, *J. Polym. Sci., Polym. Phys. B24*:2525 (1986).

99. V. J. McBierty; I. R. MacDonald, and I. M. Ward, *J. Phys. D4*:88 (1971).

100. A. P. Unwin, D. I. Bower, and I. M. Ward, *Polymer 26*:1605 (1985).

101. J. R. Dees and J. E. Spruiell, *J. Appl. Polym. Sci. 18*:1053 (1974).

102. (a) G. Elsner, C. Riekel, and H. G. Zachmann, *Adv. Polym. Sci., 67*:1 (1985). (b) C. Riekel, *Chemical Crystallography with Pulsed Neutrons and Synchrotron Radiation* (H. Carrondo and G. A. Jeffrey, eds.), Raidel., 1988.

103. (a) G. Elsner, M. H. J. Koch, J. Bordas, and H. G. Zachmann, *Makromol. Chem. 182*:126 (1981). (b) W. Wu, C. Riekel, and H. G. Zachmann, *Polym. Comm. 25*:76 (1984).

104. P. Forgaes, B. P. Tolochko, and M. A. Sheromov, *Polym. Bull. 6*:127 (1981).

105. H.G. Zachmann and C. Wutz, *Crystallization of Polymers* (M. Dosiere ed.), Kluwer, Dordrecht, 1993, pp. 403–414.

106. (a) A. Guinier and G. Fournet, *Small Angle Scattering of X-rays*, Wiley, New York, (1995). (b) W. W. Beeman, P. Kaesburg, and J. Anderegg, Size of particles and lattice defects, *Encyclopedia of Physics*, Vol. 32 (S. Flugge, ed.), Springer-Verlag, Berlin, p. 321.

107. W. O. Statton, Small angle X-ray studies of polymers, *Newer Methods of Polymer Characterization*, Interscience, New York, 1963, Chap. 6.

108. R. Bonart and R. Hosemann, *Kolloid Z.-Z. Polym. 186*:16 (1962).

109. W .O. Statton, *J. Polym. Sci. 41*:143 (1959).

110. A. Ferrero, E. Ferracini, and R. Hosemann, *Polymer 25*:1747 (1984).

111. R. G. Scott, *J. Polym. Sci. 57*:405 (1962).

112. (a) L. Sawyer and E. L. Thomas, *Polymer Microscopy*, Chapman and Hall, London, 1987. (b) D. C. Bassett, Etching and microstructural crystalline polymers, *Comprehensive Polymer Science*, Vol. 1 (C. Booth and C. Price, eds.), Pergamon, New York, 1992, Chap. 35.

113. A. Siegmann and P. H. Geil, *J. Macromol. Sci. Phys. B4*:557 (1970).

114. (a) A. Peterlin, The role of chain folding in fibers, *Man Made Fibers*, Vol. 1 (H. F. Mark, S. M. Atlas, and E. Cernia, eds.), Interscience, New York, 1967, p. 283. (b) A. Peterlin and S. Sakaoko, *J. Appl. Phys. 38*:4142 (1967). (c) A. Peterlin and K. Sakaoko, *Clean Surfaces* (G. Goldfinger, ed.), Marcel Dekker, New York, 1970.

115. (a) K. Neki and P. H. Geil, *J. Macromol. Sci., Phys. B9*:71 (1974). (b) A. Peterlin, H. Kiho, and P. H. Geil, *Polym. Let. 3*:151 (1965).

116. F. Rybnikar, unpublished data.

117. A. K. Singhania and P. H. Geil, *Makromol. Chem. 143*:231 (1971).

118. D. M. Sadler, Neutron scattering from solid polymers, *Comprehensive Polymer Science* (C. Booth and C. Price, eds.), Pergamon Press, Oxford, 1992, Chap. 32.

119. G. D. Wignall, unpublished data.

120. (a) D. Y. Yoon and P. J. Flory, *Polymer 18*:509(1977). (b) D. Y. Yoon, *J. Appl. Crystallogr. 11*:531 (1978). (c) D. Y. Yoon and P. J. Flory, *Disc. Faraday Soc. 68*: Paper 17 (1979).

121. J. D. Hoffman, E. A. DiMarzio, and C. H. Guttmann, *Disc. Faraday Soc., 68*: Paper 17(1979).

122. B. Wunderlich, *Macromolecular Physics*, Vol. 1, Academic Press, New York, 1973.

123. D. C. Bassett, *Principles of Polymer Morphology*, Cambridge University Press, Cambridge, 1981.

124. A. S. Vaughn and D. C. Bassett, Crystallization and morphology, *Comprehensive Polymer Science*, Vol. 2 (C. Booth and C. Price, eds.), Pergamon Press, Oxford, 1992, Chap. 12.

125. (a) H. D. Keith, *Mater. Res. Soc. Symp. Proc., 321*:511 (1994). (b) A. S. Vaughn, *Sci. Prog. Oxford 76*:1 (1992).

126. P. H. Geil, *C & E News 43*:72 (1965).

127. F. Rybnikar and P. H. Geil, *J. Macromol. Sci. Phys. B7*1 (1973).

128. B. S. Sprague, *J. Macromol. Sci. Phys. B8*:157 (1973).

129. M. J. Miles, New techniques in microscopy, *Characterization of Solid Polymers* (S. J. Spells, ed.), Chapman & Hall, London, 1994, Chap. 2.

130. G. J. Vansco, R. Nizman, D. Sneting, H. Schonherr, P. Smith, C. Ng, and H. Yang, *Colloids Surf., Physiochem. Eng. Aspects 87*:263 (1994).

131. (a) K. D. Jandt, M. Buhk, M. J. Miles, and J. Petermann, *Polymer 35*:2458 (1994). (b) W. Stocker, H. Schumacher, S. Graff, J. Lang, J. C. Wittman, A. J. Lovinger and B. Lotz, *Macromolecules 27*:6948 (1990).

132. (a) N. G. McCrum, B. E. Read, and G, Williams, *Anelastic and Dielectric Effects on Polymeric Solids*, Dover, New York, 1991 (reprint of Wiley, New York, 1967). (b) P. Gradin, P. G. Howgate, R. Seldin, and R. A. Brown, Dynamic mechanical properties, *Comprehensive Polymer Science*, Vol. 2, Pergamon Press, Oxford, 1992, Chap. 16.

133. K. Wangermann and H. G. Zachmann, *Prog. Colloid Polym. Sci. 57*:236 (1975).

134. J. B. Ibar, P. Denning, T. Thomas, A. Bernes, C. deGoys, J. R. Saffell, P. Jones, and C. Lacabanne, Characterization of polymers by thermally stimulated current analysis and relaxation map analysis spectroscopy, *Polymer Characterization* (C. D. Craver and T. Prouder, eds.), American Chemical Society, Washington, D.C., 1990, Chap. 10.

135. P. DeMont, L. Fourmaud, D. Chatain, and C. Lacabanne, Thermally stimulated creep for the study of copolymers and blends, *Polymer Characterization* (C. D. Craver and T. Prouder, eds.), American Chemical Society, Washington, D.C. 1990, Chap. 11.

136. S. N. Zhurkov, V. I. Vettegren, V. E. Korsukov, and I. I. Novak, *Fracture 1979, Proceedings of the 2nd International Conference on Fracture*, Chapman & Hall, London, 1969, p. 545.

137. R. P. Wool, *Polym. Eng. Sci. 20*:805 (1980).

138. K. K. R. Mocherla, Ph.D. Thesis, University of Utah, Salt Lake City, 1976.

139. H. W. Siesler, *Proceedings of the 5th European Symposium on Polymer Spectroscopy* (D. Hummell, ed.), Verlag Chemie, Weinheim, 1979.